

---

**Exploring the effect of hydrostatic pressure on the optoelectronic and thermoelectric activities of halide double perovskites  $K_2AgXI_6$  ( $X = Sb, Bi$ )**

**Student ID: MS211306**  
**Session: 2021-2022**

Thesis submitted to the Department of Physics at  
Jashore University of Science and Technology  
in partial fulfillment of the requirements  
for the degree of Master of Science  
in Physics

October, 2024

---

---

# Abstract

---

In this work, the structural, mechanical, optoelectronic and thermoelectric properties of  $K_2AgXI_6$  ( $X = Sb, Bi$ ) double perovskite materials are investigated using Density Functional Theory (DFT) as implemented in WIEN2k code both at ambient and under different hydrostatic pressure ranging up to 20 GPa for  $K_2AgSbI_6$  and up to 50 GPa for  $K_2AgBiI_6$ . The structural stability of the compounds are ensured by the Goldschmidt tolerance factor ( $\tau$ ) and the octahedral factor ( $\mu$ ). Our studied compounds exhibit perfectly cubic structures with the space group  $Fm\bar{3}m$  (space group no. 225). The band structure shows p-type semiconducting nature with an indirect band gap of 0.97 eV for  $K_2AgSbI_6$  and 1.599 eV for  $K_2AgBiI_6$  at ambient condition and band gap gradually decreases with induced pressure. Optical analysis shows that the highest transition occurs in the visible spectrum after increasing pressure for both systems compared to ambient conditions. Therefore, the studied compounds under investigation may be suitable for solar cell applications. The transport properties of both materials are investigated using the BoltzTraP code to estimate the electrical and thermal conductivities, Seebeck coefficient, power factor, and figure of merit under different hydrostatic pressures. The high values of the Seebeck coefficient and the figure of merit ensure that the studied compounds are suitable for thermoelectric applications at ambient conditions rather than under pressurized conditions. Finally, our studied compounds demonstrate good mechanical stability under applied pressure, indicating that pressure has a significant impact on their mechanical resilience.

---

# Acknowledgements

---

Firstly, all praises to the Almighty Allah, who is the most merciful and helpful. Then I would like to express my sincere gratitude to my supervisor Sahadat Jaman, and co-supervisor Dr. Mohammad Abdur Rashid, for their constant supervision, guidance, patience, and constant encouragement, which helped me a lot with this work. Without their support, this achievement would have been extremely difficult. I would also like to thank my respected faculty members of Department of Physics for their valuable suggestion and encouragement.

I am deeply indebted to the members of the Quantum Materials Simulation Lab (QMSL) for their constructive suggestions and comments, which greatly aided me in completing my thesis work within the limited timeframe. My experience working in the lab has been both highly valuable and enlightening. Access to the lab's equipment and facilities has been essential in conducting experiments and gathering data, which served as the foundation of this research. I am grateful to the various scientific journals and the authors of numerous publications (cited in the references), whose work provided me with invaluable information and knowledge for my research. I would like to thank especially my research groupmates for their constant inspiration and adequate assistance. Last, but definitely not least, I would like to express my deepest gratitude to my father and especially to my mother for their continuous support and love. Without their love, guidance, and never-ending support, this accomplishment would not be possible.

---

# Contents

---

Exploring the effect of hydrostatic pressure on the optoelectronic and thermoelectric activities of halide double perovskites  $K_2AgXI_6$  ( $X = Sb, Bi$ )

<b>1</b>	<b>Introduction</b>	<b>1</b>
<b>2</b>	<b>Basic Quantum Mechanics</b>	<b>5</b>
2.1	Schrödinger equation . . . . .	5
2.2	The wave function . . . . .	6
2.3	Born-Oppenheimer (BO) approximation . . . . .	8
2.4	The Hartree-Fock (HF) approach . . . . .	9
2.5	Limitation and failings of the Hartree-Fock (HF) approach . . . . .	14
<b>3</b>	<b>Density Functional Theory</b>	<b>16</b>
3.1	Overview . . . . .	16
3.2	The electron density . . . . .	17
3.3	Thomas-Fermi model . . . . .	18
3.4	The Hohenberg-Kohn (HK) theorems . . . . .	21
3.4.1	The HK theorem I . . . . .	21
3.4.2	The HK theorem II . . . . .	22
3.5	Kohn-Sham (KS) equation . . . . .	23
3.5.1	Solving Khon-Shan equation . . . . .	26
3.6	The exchange-correlation (XC) functional . . . . .	27

## Contents

---

3.7	Local Density Approximation (LDA)	28
3.8	Local Spin Density Approximation (LSDA)	29
3.9	Generalized Gradient Approximation (GGA)	34
3.10	LDA+U method	35
<b>4</b>	<b>Results and Discussion</b>	<b>37</b>
4.1	Computational frameworks	37
4.2	Structural properties	38
4.3	Electronic Properties	41
4.3.1	Band Structure	41
4.3.2	Density of states	45
4.4	Optical properties	51
4.4.1	Dielectric function	52
4.4.2	Absorption coefficient	55
4.4.3	Optical conductivity	56
4.4.4	Optical reflectivity	58
4.4.5	Refractive index	59
4.5	Thermoelectric properties	61
4.5.1	Seebeck coefficient	61
4.5.2	Electrical conductivity	63
4.5.3	Thermal conductivity	64
4.5.4	Power factor	65
4.5.5	Figure of merits	67
4.6	Mechanical properties	68
<b>5</b>	<b>Conclusions</b>	<b>73</b>
	<b>Bibliography</b>	<b>75</b>

---

# List of Figures

---

3.1	Flowchart of self-consistency loop for solving Kohn-Sham equation . .	27
4.1	Crystal structure of cubic double perovskites $K_2AgXI_6$ ( $X = Sb, Bi$ ) at 0 GPa pressure. . . . .	39
4.2	Energy versus unit cell volume curve of cubic double perovskite (a) $K_2AgSbI_6$ and (b) $K_2AgBiI_6$ at 0 GPa pressure. . . . .	40
4.3	The band structure of $K_2AgSbI_6$ and $K_2AgBiI_6$ at 0 GPa pressure. . .	42
4.4	The band structure of $K_2AgSbI_6$ at 0 GPa, 5 GPa, 10 GPa, 15 GPa and 20 GPa pressure. . . . .	43
4.5	The band structure of $K_2AgBiI_6$ at 0 GPa, 5 GPa, 10 GPa pressure. .	44
4.6	The band structure of $K_2AgBiI_6$ at 20 GPa, 30 GPa, 40 GPa and 50 GPa pressure. . . . .	45
4.7	(a) Total density of states of $K_2AgSbI_6$ , (b) Partial density of states of K, (c) Partial density of states of Ag, (d) Partial density of states of Sb and (e) Partial density of states of I at ambient pressure. . . . .	47
4.8	(a) Total density of states of $K_2AgSbI_6$ , (b) Partial density of states of K, (c) Partial density of states of Ag, (d) Partial density of states of Sb and (e) Partial density of states of I under different hydrostatic pressure. . . . .	48
4.9	(a) Total density of states of $K_2AgBiI_6$ , (b) Partial density of states of K, (c) Partial density of states of Ag, (d) Partial density of states of Bi and (e) Partial density of states of I at ambient pressure. . . . .	49
4.10	(a) Total density of states of $K_2AgBiI_6$ , (b) Partial density of states of K, (c) Partial density of states of Ag, (d) Partial density of states of Bi and (e) Partial density of states of I under hydrostatic pressure.	50

## LIST OF FIGURES

---

4.11	The computed optical (a) Real dielectric function of $K_2AgSbI_6$ and (b)Real dielectric function of $K_2AgBiI_6$ at ambient and under hydrostatic pressure. . . . .	53
4.12	The computed optical (a) Imaginary dielectric function of $K_2AgSbI_6$ and (b)Real dielectric function of $K_2AgBiI_6$ at ambient and under hydrostatic pressure. . . . .	54
4.13	The computed optical (a) Absorption coefficient of $K_2AgSbI_6$ and (b) Absorption coefficient of $K_2AgBiI_6$ at ambient and under hydrostatic pressure. . . . .	56
4.14	The computed optical (a) Conductivity of $K_2AgSbI_6$ and (b) Conductivity of $K_2AgBiI_6$ at ambient and under hydrostatic pressure. . .	57
4.15	The computed optical (a) Reflectivity of $K_2AgSbI_6$ and (b) Reflectivity of $K_2AgBiI_6$ at ambient pressure and under hydrostatic pressure. .	58
4.16	The computed optical (a) Refraction of $K_2AgSbI_6$ and (b) Refraction of $K_2AgBiI_6$ at ambient and under hydrostatic pressure. . . . .	60
4.17	Calculated thermal properties to observe the (a) Seebeck coefficient of $K_2AgSbI_6$ and (b) Seebeck coefficient of $K_2AgBiI_6$ at ambient and under hydrostatic pressure . . . . .	62
4.18	Calculated thermal properties to observe the (a) Electrical conductivity of $K_2AgSbI_6$ and (b) Electrical conductivity of $K_2AgBiI_6$ at ambient and under induced pressure . . . . .	63
4.19	Calculated thermal properties to observe the (a) Thermal conductivity of $K_2AgSbI_6$ and (b) Thermal conductivity of $K_2AgBiI_6$ at ambient and under induced pressure . . . . .	65
4.20	Calculated thermal properties to observe the (a) Power factor of $K_2AgSbI_6$ and (b) Power factor of $K_2AgBiI_6$ at ambient and under induced pressure . . . . .	66
4.21	Calculated thermal properties to observe the (a) Figure of merits of $K_2AgSbI_6$ and (b) Figure of merits of $K_2AgBiI_6$ at ambient and under induced pressure . . . . .	67

---

# List of Tables

---

4.1	Variation of lattice constants and band gap of $K_2AgSbI_6$ under pressure.	44
4.2	Variation of lattice constants and band gap of $K_2AgBiI_6$ under pressure.	46
4.3	Calculated the estimated elastic constant $C_{11}$ , $C_{12}$ , $C_{44}$ , Cauchy's pressure of $K_2AgSbI_6$ under hydrostatic pressure. . . . .	69
4.4	The calculated the Bulk modulus $B$ ( $GPa$ ), the Shear modulus $G$ ( $GPa$ ), Young's modulus $Y$ ( $GPa$ ), the elastic anisotropy factor ( $A$ ), $B/G$ ratio and Poisson's ratio ( $\nu$ ) of $K_2AgSbI_6$ under hydrostatic pressure. . . . .	70
4.5	Calculated the estimated elastic constant $C_{11}$ , $C_{12}$ , $C_{44}$ , Cauchy's pressure of $K_2AgBiI_6$ under hydrostatic pressure. . . . .	71
4.6	The calculated the Bulk modulus $B$ ( $GPa$ ), the Shear modulus $G$ ( $GPa$ ), Young's modulus $Y$ ( $GPa$ ), the elastic anisotropy factor ( $A$ ), $B/G$ ratio and Poisson's ratio ( $\nu$ ) of $K_2AgBiI_6$ under hydrostatic pressure. . . . .	71

**Exploring the effect of hydrostatic  
pressure on the optoelectronic and  
thermoelectric activities of halide  
double perovskites  $K_2AgXI_6$   
( $X = Sb, Bi$ )**

## Introduction

---

One of the most crucial initiatives for combating the greenhouse effect for a sustainable environment is the search for clean energy conversion [1–3]. Conventional energy sources (fossil fuels), due to their non-renewable nature, cannot keep up with the rapid economic growth, leading to continuously increasing energy demands [4–6]. Additionally, traditional energy sources are non-renewable and release various toxic gases and by-products, compromising environmental safety and contributing to global warming [7]. To address these issues, renewable energy sources that provide a continuous energy supply and are environmentally friendly are needed [8]. For instance, solar cells utilize the photovoltaic effect to transform solar energy into usable electrical energy. This efficient energy conversion is highly dependent on the semiconducting properties of the absorbing layer [9]. Generally, perovskite semiconductors ( $ABX_3$ , where A and B are cations and X is an anion) are affordable and simple to produce. Organic-inorganic lead halide perovskite solar cells are known for their high energy conversion efficiency [10,11]. However, their practical use is limited due to instability and the toxic nature of lead [12]. To address these issues, research is also being conducted on perovskites containing nontoxic elements [13,14]. Despite this, challenges such as ion migration, long-term stability in humid conditions, and limited response time continue to impede their practical applications [15].

## Introduction

---

Double perovskites (DPs) have recently become interesting contenders in the fields of solar cells and catalysis because of their high energy conversion efficiency. Double perovskite have a wide range of applications, including solar cells [16] optoelectronics [17], thermal devices [18] and sensors [19]. Finding stable, environmentally acceptable, non toxic DPs materials has therefore been seen as a strategically significant area of research in recent years. In this regard, lead-free halides and double perovskite oxides, where lead is substituted with silver (Ag), bismuth (Bi), and so on, have attracted significant attention from both theoretical and experimental viewpoints. This class of materials has been shown to be promising materials due to their strong optical conductivity, low reflectivity and high absorption coefficients.

Lead-free halide double perovskites can have a wide range of compositions to optimize their material properties. This versatility arises from their structural formula,  $A_2BB'X_6$ , which allows for numerous combinations of monovalent ions at the B sites and trivalent ions at the B' sites. Additionally, various ions can occupy the A-sites, and different halogen ions can be incorporated at the X-sites [20]. Recently, a wide range of inorganic and organic-inorganic hybrid materials based on double perovskite have been studied in the literature. Many other lead free DPs including  $Cs_2AgInCl_6$  [21],  $Cs_2AgSbCl_6$  [22],  $Cs_4CuSb_2Cl_2$  [23],  $KGeI_{3-x}Br_x$  [24] and  $Cs_2AgFeCl_6$  [25] given optical and adjustable photoluminescence characteristics. Power conversion efficiency (PCE) of solar cells based on perovskites reached 22 percent [26]. Progressive studies are expected to have a PCE of more than 25 percent [27, 28].

First-principles calculations have become a highly appealing method for computing and analyzing various material properties, as well as determining their thermodynamic stability. Numerous double perovskite halides have been theoretically investigated for their potential in optical applications [29–31]. A recent theoretical study on  $K_2AgBiX_6$  ( $X = Cl, Br$ ) has shown that halogen ions can adjust energy gaps, which could be beneficial for optical and thermoelectric applications [32]. Similarly, theoretical investigations of  $Cs_2InAgX_6$  ( $X = Cl, Br, I$ ) [33],  $Cs_2InBiX_6$  ( $X = Cl, Br, I$ ) [34], and  $Cs_2InSbX_6$  ( $X = Cl, Br, I$ ) [35] indicate that substituting halogen

## Introduction

---

ions can potentially tune band gaps, thereby optimizing the materials' optical and thermoelectric properties. Moreover, researchers have been deeply studying double perovskite materials in recent years. For example, Junaid Munir et al. studied the structural, phonon, elastic, electronic, transport, and optical properties of double perovskites  $K_2TlAsX_6$  ( $X = Cl, Br$ ) using first-principles calculations. They found that these systems are mechanically and thermodynamically stable, making them suitable for optoelectronic and renewable applications. [36]. Ghulam M. Mustafa, A., et al. investigated the optoelectronic and thermoelectric characteristics of halide based double perovskites  $K_2YAgX_6$  ( $X = Br, I$ ) and showed them to be the suitable candidate for thermoelectric applications [37]. F. Wang, W. Ning, et al. studied the lead-free halide double perovskite  $Cs_2AgBiBr_6$ , achieving the smallest reported bandgap for this material by controlling the growth temperature of single crystals [38]. The electronic and optical properties of lead-free hybrid double perovskites for photovoltaic and optoelectronic applications were investigated by M. Roknuzzaman et al. Their findings indicated that the organic-inorganic halide double perovskite  $(FA)_2BiCuI_6$  is the most promising candidate, possessing the desirable properties for photovoltaic and optoelectronic applications [39]. N.R. Kumar et al. successfully synthesized  $Cs_2AgBiX_6$  ( $X = Cl, Br, I$ ), a lead-free halide double perovskite [40]. Their research indicated that these materials possess indirect band gaps of 1.91 eV for  $Cs_2AgBiCl_6$ , 1.42 eV for  $Cs_2AgBiBr_6$ , and 0.89 eV for  $Cs_2AgBiI_6$ , which are in good agreement with reported theoretical and experimental results. All of this research results in good optical and mechanical contributions to practical purposes. Due to their surprisingly high stability and electronic structure, these materials are used in a wide variety of sustainable and renewable applications [41, 42].

However, to understand the electronic, optical and other characteristics of a double perovskite it is essential to comprehend its usefulness in various fields. Density functional theory (DFT) based computational studies can guide experimental efforts and often offer deeper insights into the properties, synthesis, and applications of materials. DFT can accurately determine various properties such as electronic, optical, elastic, and thermoelectronic characteristics [43–46], with numerous observations validating its accuracy through comparison with experimental data.

## Introduction

---

Our study determines the structural, mechanical, optoelectronic and thermoelectric properties of  $K_2AgXI_6$  ( $X = Sb, Bi$ ) under induced hydrostatic pressure. The pressure effect can cause notable alterations in the physical characteristics of double perovskite materials, opening up new possibilities for adjusting and regulating their behavior [47, 48]. A material's different properties can be readily adjusted by applying a hydrostatic pressure [49–51]. The electron orbits in pressure-dependent samples migrate in the direction of the electric field and the band-gap energy shrinks. Consequently, the bonding energy within the octahedral state is altered, leading to a decrease in the band gap energy and primarily affecting the boundary conditions of the electronic wave functions. In materials, pressure can cause structural phase transitions [52]. The arrangement of atoms within the crystal lattice can change significantly at high pressures [53]. The overall symmetry of the crystal structure as well as bond lengths and bond angles may alter as a result. The electronic and magnetic properties can be altered by pressure-induced changes in the crystal structure [54, 55]. For instance, pressure can modify the density of states close to the Fermi level, which can change electronic bandgaps or electrical conductivity [56].

In this study, we employ the first-principles calculation method based on Density Functional Theory (DFT), utilizing the WIEN2k code [57]. WIEN2k is a widely recognized and efficient software package for performing DFT calculations, offering robust capabilities for studying the electronic, optical, and mechanical properties of materials. The significance of choosing double perovskite materials for our research with both ambient and under applied hydrostatic pressure because of their interesting applications. In Chapter 2, we discuss the fundamentals of quantum mechanics. Chapter 3 delves into density functional theory, including various approximations. Chapter 4 explores the structural, mechanical, optoelectronic, and thermoelectric properties of lead-free halide double perovskites  $K_2AgXI_6$  ( $X = Sb, Bi$ ) under applied hydrostatic pressure. Finally, in the concluding chapter, we summarize our findings on the characteristics and potential applications of these materials, both at ambient and pressurized conditions.

# Basic Quantum Mechanics

---

## 2.1 Schrödinger equation

Schrödinger equation refers to a fundamental equation of quantum physics. The Schrödinger equation is a linear partial differential equation that governs the wave function of a quantum-mechanical system. It is a key result in quantum mechanics, and its discovery was a significant landmark in the development of the subject. The equation is named after Erwin Schrödinger, who postulated the equation in 1925, and published it in 1926 [58]. The time-independent Schrödinger equation,

$$\hat{H}\psi(\vec{r}) = E\psi(\vec{r}) \quad (2.1)$$

Where,  $\hat{H}$  is the hamiltonian operator and  $\psi$  is the wave function. It is often impracticable to use a complete relativistic formulation of the formula; therefore Schrödinger himself postulated a non-relativistic approximation which is nowadays often used, especially in quantum chemistry.

Using the Hamiltonian for a single particle,

$$\hat{H} = \hat{T} + \hat{V} = -\frac{\hbar^2}{2m}\vec{\nabla}^2 + V(\vec{r}) \quad (2.2)$$

leads to the (non-relativistic) time-independent single-particle Schrödinger equation,

$$\hat{E}\psi(\vec{r}) = \left[ -\frac{\hbar^2}{2m}\vec{\nabla}^2 + V(\vec{r}) \right] \psi(\vec{r}). \quad (2.3)$$

For  $N$  particles in three dimensions, the Hamiltonian is,

$$\hat{H} = \sum_{i=1}^N \frac{\hat{p}_i^2}{2m_i} + V(\vec{r}_1, \vec{r}_2, \dots, \vec{r}_N) = -\frac{\hbar^2}{2} \sum_{i=1}^N \frac{1}{m_i} \nabla_i^2 + V(\vec{r}_1, \vec{r}_2, \dots, \vec{r}_N) \quad (2.4)$$

The corresponding Schrödinger equation reads,

$$\hat{E}\psi(\vec{r}_1, \vec{r}_2, \dots, \vec{r}_N) = \left[ -\frac{\hbar^2}{2} \sum_{i=1}^N \frac{1}{m_i} \nabla_i^2 + V(\vec{r}_1, \vec{r}_2, \dots, \vec{r}_N) \right] \psi(\vec{r}_1, \vec{r}_2, \dots, \vec{r}_N) \quad (2.5)$$

Special cases are the solutions of the time-independent Schrödinger equation, where the Hamiltonian itself has no time-dependency (which implies a time-independent potential  $V(\vec{r}_1, \vec{r}_2, \dots, \vec{r}_N)$  and the solutions therefore describe standing waves which are called stationary states or orbitals). The time-independent Schrödinger equation is not only easier to treat, but the knowledge of its solutions also provides crucial insight to handle the corresponding time-dependent equation. Furthermore, the left hand side of the equation reduces to the energy eigenvalue of the Hamiltonian multiplied by the wave function, leading to the general eigenvalue equation,

$$E\psi(\vec{r}_1, \vec{r}_2, \dots, \vec{r}_N) = \hat{H}\psi(\vec{r}_1, \vec{r}_2, \dots, \vec{r}_N) \quad (2.6)$$

Again, using the many-body Hamiltonian, the Schrödinger equation becomes,

$$E\psi(\vec{r}_1, \vec{r}_2, \dots, \vec{r}_N) = \left[ -\frac{\hbar^2}{2} \sum_{i=1}^N \frac{1}{m_i} \nabla_i^2 + V(\vec{r}_1, \vec{r}_2, \dots, \vec{r}_N) \right] \psi(\vec{r}_1, \vec{r}_2, \dots, \vec{r}_N) \quad (2.7)$$

## 2.2 The wave function

A wave function is a mathematical representation of a particle's quantum state as a function of momentum, position, time and spin in quantum physics. It contains

## Basic Quantum Mechanics

---

all the information about the particle's state. A wave function is represented by the Greek letter  $\psi$  (psi). The probability of finding an electron within the matter-wave may be explained using a wave function. This may be produced by incorporating an imaginary number that is squared to give a real number solution resulting in an electrons position.

Max Born developed a probabilistic interpretation of the wave function as a probability density, which is a major principle of the Copenhagen interpretation of quantum mechanics [59,60].

$$|\psi(\vec{r}_1, \vec{r}_2, \dots, \vec{r}_N)|^2 d\vec{r}_1, d\vec{r}_2, \dots, \vec{r}_N. \quad (2.8)$$

The particles 1, 2, ...,  $N$  are all present at the same time in the corresponding volume element  $d\vec{r}_1, d\vec{r}_2, \dots, d\vec{r}_N$  which is the probability that is specified by equation (2.8) [61]. If the positions of two particles are exchanged, the total probability density cannot be affected. That is to written as,

$$|\psi(\vec{r}_1, \vec{r}_2, \dots, \vec{r}_i, \vec{r}_j, \dots, \vec{r}_N)|^2 = |\psi(\vec{r}_1, \vec{r}_2, \dots, \vec{r}_j, \vec{r}_i, \dots, \vec{r}_N)|^2. \quad (2.9)$$

The symmetrical and anti-symmetrical wave functions are two possible wavefunction behaviours during a particle exchange. The symmetrical wave function remains unchanged as a result of such exchange, which corresponds to bosons (integer or zero spin). However, the anti-symmetrical wave function shifts it's sign to correspond to fermions (half-integer spin) [62,63]. Because electrons are fermions, in this text may explore the anti-symmetric fermion wave function. The Pauli exclusion principle, which states that no two electrons may occupy the same orbital, is followed by the anti-symmetric fermion wave function. Another result of probability interpretation is the normalization of the wave function [62]. A particle's wave function must be normalized. The probability of finding the particle somewhere in space is unity as,

$$\int d\vec{r}_1 \int d\vec{r}_2 \dots \int d\vec{r}_N |\psi(\vec{r}_1, \vec{r}_2, \dots, \vec{r}_N)|^2 = 1. \quad (2.10)$$

Equation (2.10) is physically valid. Continuous and square-integrable wave functions are required. In quantum physics, any wave function that is not continuous and square-integrable has no physical meaning [64]. When we calculate the expec-

tation values of operators with a wave function, we get the expectation value of the corresponding observable for that wavefunction, which is another important aspect of the wave function. This may be expressed for an observable,  $O(\vec{r}_1, \vec{r}_2, \dots, \vec{r}_N)$  as,

$$O = \langle O \rangle = \int d\vec{r}_1 \int d\vec{r}_2 \int d\vec{r}_N \psi^*(\vec{r}_1, \vec{r}_2, \dots, \vec{r}_N) \hat{O} \psi(\vec{r}_1, \vec{r}_2, \dots, \vec{r}_N). \quad (2.11)$$

## 2.3 Born-Oppenheimer (BO) approximation

The Schrödinger equation of a many-body system is,

$$H_{tot} \psi(\{\vec{R}_I\}, \{\vec{r}_i\}) = E \psi(\{\vec{R}_I\}, \{\vec{r}_i\}). \quad (2.12)$$

Where,  $H_{tot}$  is the total Hamiltonian,  $E$  is the total energy and  $\psi(\{\vec{R}_I\}, \{\vec{r}_i\})$  is the total wave function of the system. The total Hamiltonian of a many-body system consisting of nuclei and electrons can be written as,

$$\begin{aligned} \hat{H}_{tot} = & - \sum_I \frac{\hbar^2}{2M_I} \nabla_{\vec{R}_I}^2 - \sum_i \frac{\hbar^2}{2m_e} \nabla_{\vec{r}_i}^2 + \frac{1}{2} \sum_{I,J} \frac{Z_I Z_J e^2}{|\vec{R}_I - \vec{R}_J|} \\ & + \frac{1}{2} \sum_{i,j} \frac{e^2}{|\vec{r}_i - \vec{r}_j|} - \sum_{I,i} \frac{Z_I e^2}{|\vec{R}_I - \vec{r}_i|}, \end{aligned} \quad (2.13)$$

where, the indexes  $I, J$  run on nuclei,  $i$  and  $j$  on electrons,  $\vec{R}_I$  and  $M_I$  are position and mass of the nuclei,  $\vec{r}_i$  and  $m_e$  are position and mass of the electrons. The first term of the above equation represents the kinetic energy of the Nuclei. Second term represents the kinetic energy of the electrons. Third term  $\frac{1}{2} \sum_{I,J} \frac{Z_I Z_J e^2}{|\vec{R}_I - \vec{R}_J|}$  is for potential energy of nucleus-nucleus Coulomb interaction, the fourth term is the potential energy electron-electron Coulomb interaction and the last term is the potential energy of nucleus-electron Coulomb interaction. As nuclei are significantly heavier than electrons (the mass of a proton is about 1836 times the mass of an electron), the electrons travel considerably more quickly than the nuclei [64]. In that case, Born-Oppenheimer (BO) approximation was proposed by Born and Oppenheimer in 1927. The Born-Oppenheimer approximation is an assumption that it

is possible to distinguish equation (2.13) between the nuclear and electronic motions of molecules. Consider the nuclei to be static, classical potential with respect to the electron, then address the electronic issue without further consideration of the nuclei [65]. On the timeline of the electronic transition, it is possible to claim that the core movement can be disregarded, i.e., it has no bearing on them [66–68]. Adopting Born-Oppenheimer approximation the electronic hamiltonian the becomes,

$$\hat{H} = - \sum_i \frac{\hbar^2}{2m_e} \nabla_{\vec{r}_i}^2 + \frac{1}{2} \sum_{i,j} \frac{e^2}{|\vec{r}_i - \vec{r}_j|} - \sum_{I,i} \frac{Z_I e^2}{|\vec{R}_I - \vec{r}_i|}. \quad (2.14)$$

The BO approximation’s importance lies in it’s ability to distinguish between the motion of electrons and nuclei. The starting point of DFT is the electron motion in a static external potential  $V_{ext}(\vec{r})$  created by the nucleus. Born and Huang expanded the BO approximation, giving it the name Born-Huang (BH) approximation [69], to account for more non-adiabatic effects in the electronic Hamiltonian than the BO approximation did.

## 2.4 The Hartree-Fock (HF) approach

In order to find a suitable strategy to approximate the analytically not accessible solutions of many-body problems, a very useful tool is variational calculus, similar to the least-action principle of classical mechanics. By the use of variational calculus, the ground state wave function  $\psi_0$ , which corresponds to the lowest energy of the system  $E_0$ , can be approached [61]. Hence, for now only the electronic Schrödinger equation is of interest, therefore in the following sections we set  $\hat{H} \equiv \hat{H}_{el}$ ,  $E \equiv E_{el}$ , and so on. Observables in quantum mechanics are calculated as the expectation values of operators [70, 71]. The energy as observable corresponds to the Hamiltonian operator, therefore the energy corresponding to a general Hamiltonian can be calculated as,

$$E = \langle \hat{H} \rangle = \int d\vec{r}_1 \int d\vec{r}_2 \dots \int d\vec{r}_N \psi^* (\vec{r}_1, \vec{r}_2, \dots, \vec{r}_N) \hat{H} \psi (\vec{r}_1, \vec{r}_2, \dots, \vec{r}_N) \quad (2.15)$$

## Basic Quantum Mechanics

---

The Hartree-Fock technique is based on the principle that the energy obtained by any (normalized) trial wave function other than the actual ground state wave function is always an upper bound, i.e. higher than the actual ground state energy. If the trial function happens to be the desired ground state wave function, the energies are equal,

$$E_{trial} \geq E_0 \quad (2.16)$$

with

$$E_{trial} = \int d\vec{r}_1 \int d\vec{r}_2 \dots \int d\vec{r}_N \psi_{trial}^*(\vec{r}_1, \vec{r}_2, \dots, \vec{r}_N) \hat{H} \psi_{trial}(\vec{r}_1, \vec{r}_2, \dots, \vec{r}_N) \quad (2.17)$$

and

$$E_0 = \int d\vec{r}_1 \int d\vec{r}_2 \dots \int d\vec{r}_N \psi_0^*(\vec{r}_1, \vec{r}_2, \dots, \vec{r}_N) \hat{H} \psi_0(\vec{r}_1, \vec{r}_2, \dots, \vec{r}_N) \quad (2.18)$$

For a detailed description of this notation, the reader is referred to the original publication [72]. In that notation, equations (2.17) to (2.19) are expressed as,

$$\langle \psi_{trial} | \hat{H} | \psi_{trial} \rangle = E_{trial} \geq E_0 = \langle \psi_0 | \hat{H} | \psi_0 \rangle \quad (2.19)$$

*Proof:* [71] The eigenfunctions  $\psi_i$  of the Hamiltonian  $\hat{H}$  (each corresponding to an energy eigenvalue  $E_i$ ) form a complete basis set, therefore any normalized trial wave function  $\psi_{trial}$  can be expressed as linear combination of those eigenfunctions.

$$\psi_{trial} = \sum_i \lambda_i \psi_i \quad (2.20)$$

The assumption is made that the eigenfunctions are orthogonal and normalized. Hence it is requested that the trial wave function is normalized, it follows that,

$$\langle \psi_{trial} | \psi_{trial} \rangle = 1 = \left\langle \sum_i \lambda_i \psi_i \left| \sum_j \lambda_j \psi_j \right. \right\rangle = \sum_i \sum_j \lambda_i^* \lambda_j \langle \psi_i | \psi_j \rangle = \sum_j |\lambda_j|^2 \quad (2.21)$$

On the other hand, following equations (2.22) to (2.24),

$$E_{trial} = \langle \psi_{trial} | \hat{H} | \psi_{trial} \rangle = \langle \sum_i \lambda_i \psi_i | \hat{H} | \sum_j \lambda_j \psi_j \rangle = \sum_j E_j |\lambda_j|^2 \quad (2.22)$$

Together with the fact that the ground state energy  $E_0$  is per definition the lowest possible energy, and therefore has the smallest eigenvalue ( $E_0 \leq E_i$ ), it is found that,

$$E_{trial} = \sum_j E_j |\lambda_j|^2 \geq E_0 \sum_j |\lambda_j|^2 \quad (2.23)$$

what resembles equation (2.22). Equations (2.23) to (2.26) also include that a search for the minimal energy value while applied on all allowed N-electron wave-functions will always provide the ground-state wave function (or wave functions, in case of a degenerate ground state where more than one wave function provides the minimum energy). Expressed in terms of functional calculus, where  $\psi \rightarrow N$  addresses all allowed N-electron wave functions,

$$E_0 = \min_{\psi \rightarrow N} E[\psi] = \min_{\psi \rightarrow N} \langle \psi | \hat{H} | \psi \rangle = \min_{\psi \rightarrow N} \langle \psi | \hat{T} + \hat{V} + \hat{U} | \psi \rangle \quad (2.24)$$

Due to the vast number of alternative wave functions on the one hand and processing power and time constraints on the other, this search is essentially unfeasible for N-electron systems. Restriction of the search to a smaller subset of potential wave functions, as in the Hartree-Fock approximation, is conceivable. A Slater determinant is a formula in quantum mechanics that describes the wave function of a multi-fermionic system. It satisfies anti-symmetric criteria, and thus the Pauli's principle, by changing sign when two electrons are exchanged (or other fermions). Only a small fraction of all potential fermionic wave functions can be expressed as a single Slater determinant, but because of their simplicity, they are an important and useful subset. In the Hartree-Fock approach, the search is restricted to approximations of the N-electron wave function by an antisymmetric product of N (normalized) one electron wave functions, the so called spin-orbitals  $\chi_i(\vec{x}_i)$  [73]. A

wave function of this type is called Slater-determinant and reads,

$$\psi_0 \approx \phi_{SD} = (N!)^{-\frac{1}{2}} \begin{vmatrix} \chi_1(\vec{x}_1) & \chi_2(\vec{x}_1) & \cdots & \chi_N(\vec{x}_1) \\ \chi_1(\vec{x}_2) & \chi_2(\vec{x}_2) & \cdots & \chi_N(\vec{x}_2) \\ \vdots & \vdots & \ddots & \vdots \\ \chi_1(\vec{x}_N) & \chi_2(\vec{x}_N) & \cdots & \chi_N(\vec{x}_N) \end{vmatrix} \quad (2.25)$$

It is important to notice that the spin-orbitals  $\chi_i(\vec{x}_i)$  are not only depending on spatial coordinates but also on a spin coordinate which is introduced by a spin function,  $\vec{x}_i = \vec{r}_i, s$ . Returning to the variational principle and equation (2.27), the ground state energy approximated by a single slater determinant becomes,

$$\begin{aligned} E_0 &= \min_{\phi_{SD} \rightarrow N} E[\phi_{SD}] \\ &= \min_{\phi_{SD} \rightarrow N} \langle \phi_{SD} | \hat{H} | \phi_{SD} \rangle \\ &= \min_{\phi_{SD} \rightarrow N} \langle \phi_{SD} | \hat{T} + \hat{V} + \hat{U} | \phi_{SD} \rangle \end{aligned} \quad (2.26)$$

A general expression for the Hartree-Fock Energy is obtained by usage of the Slater determinant as a trial function.

$$E_{HF} = \langle \phi_{SD} | \hat{H} | \phi_{SD} \rangle = \langle \phi_{SD} | \hat{T} + \hat{V} + \hat{U} | \phi_{SD} \rangle \quad (2.27)$$

For the sake of brevity, a detailed derivation of the final expression for the Hartree-Fock energy is omitted. It is a straightforward calculation found for example in the Book by Schwabl [70]. The final expression for the Hartree-Fock energy contains three major parts: [73].

$$E_{HF} = \langle \phi_{SD} | \hat{H} | \phi_{SD} \rangle = \sum_i^N (i | \hat{h} | i) + \frac{1}{2} \sum_i^N \sum_j^N [(ii|jj) - (ij|ji)] \quad (2.28)$$

with

$$(i | \hat{h} | i) = \int \chi_i^*(\vec{x}_i) \left[ -\frac{1}{2} \nabla_i^2 - \sum_{k=1}^M \frac{Z_k}{r_{ik}} \right] \chi_i(\vec{x}_i) d\vec{x}_i, \quad (2.29)$$

$$(ii|jj) = \iint |\chi_i(\vec{x}_i)|^2 \frac{1}{r_{ij}} |\chi_j(\vec{x}_j)|^2 d\vec{x}_i d\vec{x}_j, \quad (2.30)$$

$$(ij|ji) = \iint \chi_i(\vec{x}_i) \chi_j^*(\vec{x}_j) \frac{1}{r_{ij}} \chi_j(\vec{x}_j) \chi_i^*(\vec{x}_i) d\vec{x}_i d\vec{x}_j \quad (2.31)$$

The first term corresponds to the kinetic energy and the nucleus-electron interactions,  $\hat{h}$  denoting the single particle contribution of the Hamiltonian, whereas the latter two terms correspond to electron-electron interactions. They are called Coulomb and exchange integral, respectively. Examination of equations (2.30) to (2.34) furthermore reveals, that the Hartree-Fock energy can be expressed as a functional of the spin orbitals  $E_{HF} = E[\{\chi_i\}]$ . Thus, variation of the spin orbitals leads to the minimum energy. An important point is that the spin orbitals remain orthonormal during minimization. This restriction is accomplished by the introduction of Lagrangian multipliers  $\lambda_i$  in the resulting equations, which represent the Hartree-Fock equations.

$$\hat{f}\chi_i = \lambda_i \chi_i \quad i = 1, 2, \dots, N \quad (2.32)$$

with

$$\hat{f}_i = -\frac{1}{2}\vec{\nabla}_i^2 - \sum_{k=1}^M \frac{Z_k}{r_{ik}} + \sum_i^N [\hat{J}_j(\vec{x}_i) - \hat{K}_j(\vec{x}_i)] = \hat{h}_i + \hat{V}^{HF}(i) \quad (2.33)$$

Finally one arrives at the Fock operator for the  $i$ -th electron. In similarity to equations (2.30) to (2.34), the first two terms represent the kinetic and potential energy due to nucleus-electron interaction, collected in the core Hamiltonian  $\hat{h}_i$ , whereas the latter terms are sums over the Coulomb operators  $\hat{J}_j$  and the exchange operators  $\hat{K}_j$  with the other  $j$  electrons, which form the Hartree-Fock potential  $\hat{V}^{HF}$ . There are major approximation of Hartree-Fock can be seen. The two electron repulsion operator from the original Hamiltonian is exchanged by a one-electron operator  $\hat{V}^{HF}$  which describes the repulsion in average.

## 2.5 Limitation and failings of the Hartree-Fock (HF) approach

Atoms as well as molecules can have an even or odd number of electrons. If the number of electrons is even and all of them are located in double occupied spatial orbitals  $\phi_i$ , the compound is in a singlet state. Such systems are called closed-shell systems. Compounds with an odd number of electrons as well as compounds with single occupied orbitals, i.e. species with triplet or higher ground state, are called open-shell systems respectively. These two types of systems correspond to two different approaches of the Hartree-Fock method. In the restricted HF-method (RHF), all electrons are considered to be paired in orbitals whereas in the unrestricted HF (UHF)-method this limitation is lifted totally. It is also possible to describe open-shell systems with a RHF approach where only the single occupied orbitals are excluded which is then called a restricted open-shell HF (ROHF) which is an approach closer to reality but also more complex and therefore less popular than UHF [73].

There are also closed-shell systems which require the unrestricted approach in order to get proper results. For instance, the description of the dissociation of  $H_2$  (i.e. the behavior at large internuclear distance), where one electron must be located at one hydrogen atom, can logically not be obtained by the use of a system which places both electrons in the same spatial orbital. Therefore the choice of method is always a very important point in HF calculations [74]. Kohn states several  $M = p^5$  with  $3 \leq p \leq 10$  parameters for an output with adequate accuracy in the investigations of the  $H_2$  system [75]. For a system with  $N = 100$  electrons, the number of parameters rises to,

$$M = p^{3N} = 3^{300} \text{ to } 10^{300} \approx 10^{150} \text{ to } 10^{300}$$

According to the equation (2.37), energy reduction would have to be done in a space with at least  $10^{150}$  dimension, which is well above current computer capabilities. As a result, HF methods are limited to situations involving a modest number of electron

( $N \approx 10$ ), This barrier commonly referred to as the exponential wall because of the exponential component in (2.41) [75]. Since a many electron wave function cannot be described entirely by a single Slater determinant, the energy obtained by HF calculations is always larger than the exact ground state energy. The most accurate energy obtainable by HF-methods is called the Hartree-Fock-limit. The Hartree-Fock-limit is the most precise energy that can be calculated using HF-methods [76]. Since a many electron wave function cannot be described entirely by a single Slater determinant, the energy obtained by HF calculations is always larger than the exact ground state energy. The most accurate energy obtainable by HF-methods is called the Hartree-Fock-limit. The difference between  $E_{HF}$  and  $E_{exact}$  is called correlation energy and can be denoted as [77],

$$E_{corr}^{HF} = E_{min} - E_{HF}. \quad (2.35)$$

Despite the fact that  $E_{corr}$  is usually small against  $E_{min}$ , as in the example of a  $N_2$  molecule where,

$$E_{corr}^{HF} = 14.9eV < 0.001 \cdot E_{min}, \quad (2.36)$$

it can have a huge influence [78]. For instance, the experimental dissociation energy of the  $N_2$  molecule is,

$$E_{diss} = 9.9eV < E_{corr}, \quad (2.37)$$

which corresponds to a large contribution of the correlation energy to relative energies such as reaction energies which are of particular interest in quantum chemistry. The main contribution to the correlation energy arises from the mean field approximation used in the HF-method. That means one electron moves in the average field of the other ones, an approach which completely neglects the intrinsic correlation of the electron movements. To get a better understanding what that means, one may picture the repulsion of electrons at small distances which clearly cannot be covered by a mean-field approach like the Hartree-Fock method.

# Density Functional Theory

---

### 3.1 Overview

Computational methods have now become an essential aspect of the scientific world, particularly in the calculation of issues. Computers and numerical approaches are important for issues involving enormous quantities of particles, data and so on that cannot be solved analytically. Additionally, it requires a large amount of funding or resources for the experiment.

DFT is a type of ab initio method that is often referred to as a computational quantum mechanical modeling method. The method is well-known at the matter of quantum chemistry, condensed matter physics, materials science et cetera. The application of this method starts with remedying the many-body Schrödinger equation equation problem. However, DFT is more than just another method to solve the Schrödinger equation equation. DFT provides an entirely distinct approach to any interacting problem, translating it perfectly to more simple non-interacting problem. This methodology is broadly utilized for resolving a variety of issues, with the electronic structure problem being the most common [59]. In DFT, the electron density is used as the fundamental factor, instead of the wave-function. Another method for solving the many-body Schrödinger equation equation is the Hartree-

Fock approach, that use wave-functions to describe the electronic figure of atoms and substance. However, this methods has several drawbacks, including a high cost of calculation time for investigating big systems. But DFT has demonstrated superior accuracy at a reduced computing cost, making it superior to all other approaches. This facts makes DFT the most useful method to analyze electronic structure. Walter Kohn with his co-workers developed this “Density functional theory” and find out the way of using the electron density to resolve the Schrödinger equation equation. For his timeworn work, he got novel prize in 1998 [60]. The chapter describes their work in broad strokes, beginning with fundamental quantum physics, its issues, and how DFT resolves them.

### 3.2 The electron density

The electron density (for  $N$  electrons) as the basic variable of density fuctional theory is defined as [79] In electronic system, the number of electron per unit volume in a given state is the electron density for a state designated by  $n(\vec{r})$ . Its formula in terms of  $\psi$  is,

$$n(\vec{r}) = N \sum_{s_1} \int d\vec{x}_2 \dots \int d\vec{x}_N \psi^*(\vec{x}_1, \vec{x}_2, \dots, \vec{x}_N) \psi(\vec{x}_1, \vec{x}_2, \dots, \vec{x}_N). \quad (3.1)$$

The electron density can also be described as a measurably obserable quantity based simply on spatial coordinates if the spin coordinates are further neglected [75].

$$n(\vec{r}) = N \int d\vec{r}_2 \dots \int d\vec{r}_N \psi^*(\vec{r}_1, \vec{r}_2, \dots, \vec{r}_N) \psi(\vec{r}_1, \vec{r}_2, \dots, \vec{r}_N) \quad (3.2)$$

with, for instance, an X-ray diffraction measurement. It must be confirmed that a method employing the electron density as a variable actually contains all necessary information about the system before it is presented. That entails, specifically, that it must include details on the electron number  $n$  as well as the external potential denoted by  $\hat{V}$ . By integrating the electron density over the spatial variables, one

may get the total number of electrons.

$$N = \int d\vec{r} n(\vec{r}). \quad (3.3)$$

For an atom in its ground state the density decreases monotonically away from the nucleus [80]. The electron density at any atomic nucleus in an atom, molecule, or solid has a finite value. Hohenberg and Kohn pointed out that if one knows the density of the ground state of a many electron system, one can deduce from it the external potential in which the electrons reside, up to an overall constant [65]. It must be kept in mind that the only ways in which two many electron problem can differ are in the external potentials  $\hat{V}$  and in the number of electrons that reside in the potentials. According to this results, both of these external parameters are determined by the electron density, so one can say that the density completely determines the many body problem. This statement is surprising, because the density is a real function of a single spatial variable while complete quantum mechanical wave function needs  $N$  variables for its description. The starting point of the theory is the observation of Hohenberg and Kohn that electron density contains in principle all the information contained in a many electron wave function.

### 3.3 Thomas-Fermi model

The assumptions stated by Thomas are that, electrons are distributed uniformly in a six dimensional phase space for the motion of an electron at the rate of two for each  $h^3$  of volume and that there is an effective potential field that is itself determined by the nuclear charge and this distribution of electrons. The Thomas Fermi formula for electron density can be derived from these assumptions [65]. Let us consider the space divided into many small cubes, each of side  $l$  and volume  $\delta V = l^3$ , each containing some fixed number of electrons  $\delta N$  and we assume that the electrons in each shell behave like independent fermions at the temperature 0 K, with the cells independent of one another. The energy level of a particle in a three dimensional

## Density Functional Theory

---

infinite well are given by the formula,

$$\epsilon(n_x, n_y, n_z) = \frac{h^3}{8ml^2}(n_x^2 + n_y^2 + n_z^2) \quad (3.4)$$

$$= \frac{h^3}{8ml^2}R^2 \quad (3.5)$$

Where  $n_x, n_y, n_z = 1, 2, 3, \dots$  and the second equality defines by the quantity  $R$ . For high quantum numbers, that is, for large  $R$ , the number of distinct energy levels with energy smaller than  $\epsilon$  can be approximated by the volume of one octant of a spherical with radius  $R$  in the space  $n_x, n_y, n_z$ . This number is,

$$\phi(\epsilon) = \frac{1}{8} \left( \frac{4^3}{3} \right) \quad (3.6)$$

$$= \frac{\pi}{6} \left( \frac{8ml^2\epsilon}{h^2} \right)^{\frac{3}{2}} \quad (3.7)$$

The number of energy levels between  $\epsilon$  and  $\epsilon + \delta\epsilon$  is accordingly,

$$g(\epsilon)\Delta\epsilon = \phi(\epsilon + \delta\epsilon) - \phi(\epsilon) \quad (3.8)$$

$$= \frac{\pi}{4} \left( \frac{8ml^2\epsilon}{h^2} \right)^{\frac{3}{2}} \epsilon^{\frac{1}{2}} + \phi(\delta\epsilon)^2 \quad (3.9)$$

where the function  $g(\epsilon)$  is the density of states at energy  $\epsilon$ . To compute the total energy for the cell with electrons, we need the probability for the state with energy to be occupied which we call  $f(\epsilon)$ . This is the Fermi Dirac distribution.

$$f(\epsilon) = \frac{1}{1 + \exp^{\beta(\epsilon - \mu)}} \quad (3.10)$$

where  $\epsilon_f$  is the Fermi energy. All the states energy smaller than  $\epsilon_f$  are occupied and those with energy greater than  $\epsilon_f$  are unoccupied. The Fermi energy  $\epsilon_f$  is the zero temperature limit of the chemical potential  $\mu$ . Now we find the total energy of the electrons in this cell by summing the contributions from the different energy states:

$$\Delta E = 2 \int \epsilon f(\epsilon) g(\epsilon) d\epsilon \quad (3.11)$$

$$= 2 \int \epsilon f(\epsilon) \frac{\pi}{4} \left( \frac{8ml^2}{h^2} \right)^{\frac{3}{2}} \epsilon^{\frac{1}{2}} d\epsilon \quad (3.12)$$

$$= \frac{8\pi}{5} \left( \frac{2m}{h^2} \right)^{\frac{3}{2}} l^3 \epsilon_f^{\frac{5}{2}} \quad (3.13)$$

where the factor 2 enters because each energy level is doubly occupied by one electron with spin  $\alpha$  and another with spin  $\beta$ . The fermi energy  $E_f$  is related to the number of electrons  $\Delta N$  in the cell through the formula,

$$\Delta N = 2 \int f(\epsilon) g(\epsilon) d\epsilon \quad (3.14)$$

$$= \frac{8\pi}{3} \left( \frac{2m}{h^2} \right)^{\frac{3}{2}} l^3 \epsilon_f^{\frac{3}{2}}$$

Eliminating  $\epsilon_f$  from 4.13 and 4.14 we have,

$$\Delta E = \frac{3}{5} \Delta N E_f \quad (3.15)$$

$$= \frac{3h^2}{10m} \left( \frac{3}{8\pi} \right)^{\frac{2}{3}} l^3 \left( \frac{\Delta N}{l^3} \right)^{\frac{5}{3}} \quad (3.16)$$

Equation (3.16) is a relation between total kinetic energy and the electron density  $n = \frac{\Delta N}{l^3} = \frac{\Delta N}{\Delta V}$  for each cell in the space. Adding the contribution from all cells we find the total kinetic energy to be, now reverting to atomic units,

$$T_{TF}[n] = C_f \int n^{\frac{5}{3}}(\vec{r}) d\vec{r} \quad (3.17)$$

where,

$$C_f = \frac{3}{10} (3\pi^2)^{\frac{2}{3}} = 2.871 \quad (3.18)$$

Here, we first come across the LDA [65] one of the most significant concepts in contemporary density functional theory. By using locally applicable relations suited for a homogeneous electronic system, electronic characteristics are approximated as

functions of the electron density. In terms of electron density, the energy formula for an atom is,

$$T_{TF}[n(\vec{r})] = C_F \int n^{\frac{5}{3}}(\vec{r})d\vec{r} - Z \int \frac{n(\vec{r})}{\vec{r}}d\vec{r} + \frac{1}{2} \int \int \frac{n(\vec{r}_1)n(\vec{r}_2)}{|\vec{r}_1 - \vec{r}_2|}d\vec{r}_1d\vec{r}_2 \quad (3.19)$$

This is the energy functional of Thomas-Fermi theory of atoms. The method became considered as an overly simplified model of little real significance for quantitative predictions in atomic, molecular, or solid state physics because the accuracy for atoms is not as high with this model as it is with other methods.

### 3.4 The Hohenberg-Kohn (HK) theorems

Density functional theory (DFT) is the most widely used many-body approach for electronic structure calculations and has significantly impacted on modern science and engineering. DFT is made possible by the existence of two ingeniously simple theorems put forward and proven by Hohenberg and Kohn in 1964 [81]. The Hohenberg-Kohn theorems which have become a basic tool for the study of electronic structure of matter. Basically, any system that involves electron.

#### 3.4.1 The HK theorem I

For any system of interacting particles in an external potential  $V_{ext}(\vec{r})$ , the density is uniquely determined (in other words, the external potential is a unique functional of the density).

##### Proof of the HK theorem I

Assume that there exist two potentials  $V_{ext}(\vec{r})$  and  $V'_{ext}(\vec{r})$  differing by more than a constant and giving rise to the same ground state density,  $n_0(\vec{r})$ . Obviously,  $V_{ext}(\vec{r})$  and  $V'_{ext}(\vec{r})$  belong to distinct Hamiltonians  $\hat{H}$  and  $\hat{H}'$ , which give rise to distinct wave functions  $\psi$  and  $\psi'$ . Because of the variational principle, no wave function can

give an energy that is less than the energy of  $\psi$  for  $\hat{H}$ . That is,

$$\begin{aligned}
 E_0 &< \langle \psi' | \hat{H} | \psi' \rangle \\
 &< \langle \psi' | \hat{H}' | \psi' \rangle + \langle \psi' | \hat{H} - \hat{H}' | \psi' \rangle \\
 &< E'_0 + \int n_0(\vec{r}) [V_{ext}(\vec{r}) - V'_{ext}(\vec{r})] d\vec{r}
 \end{aligned} \tag{3.20}$$

Similarly,

$$\begin{aligned}
 E'_0 &< \langle \psi | \hat{H} | \psi \rangle \\
 &< \langle \psi | \hat{H} | \psi \rangle + \langle \psi | \hat{H}' - \hat{H} | \psi \rangle \\
 &< E_0 + \int n_0(\vec{r}) [V'_{ext}(\vec{r}) - V_{ext}(\vec{r})] d\vec{r}.
 \end{aligned} \tag{3.21}$$

Adding equations (2.20) and (2.21) lead to the contradiction,

$$E_0 + E'_0 < E_0 + E'_0 \tag{3.22}$$

which is clearly a contradiction. Thus, the theorem has been proven by reduction absurdum.

### 3.4.2 The HK theorem II

A universal functional  $F[n(\vec{r})]$  for the energy  $E[\psi']$  can be defined in terms of the density, The exact ground state is the global minimum value of this functional.

#### Proof of the HK theorem II

Since the external potential is uniquely determined by the density and since the potential in turn uniquely (except in degenerate situations) determines the ground state wavefunction, all the other observables of the system such as kinetic energy are uniquely determined. Then one may write the energy as a functional of the density. The universal functional  $F[n(\vec{r})]$  can be written as,

$$F[n(\vec{r})] \equiv T[n(\vec{r})] + E_{int}[n(\vec{r})] \tag{3.23}$$

where  $T[n(\vec{r})]$  is the kinetic energy and  $E_{int}[n(\vec{r})]$  is the interaction energy of the

## Density Functional Theory

---

particles. According to variational principle, for any wavefunction  $\psi'$ , the energy functional  $E[\psi']$ :

$$E[\psi'] \equiv \langle \psi' | \hat{T} + \hat{V}_{int} + \hat{V}_{ext} | \psi' \rangle \quad (3.24)$$

has its global minimum value only when  $\psi'$  is the ground state wavefunction  $\psi_0$  with the constraint that the total number of the particle is conserved. According to HK theorem I,  $\psi'$  must correspond to a ground state with particle density  $n'(\vec{r})$  and external potential  $V'_{ext}(\vec{r})$ , then  $E[\psi']$  is a functional of  $n'(\vec{r})$ . According to variational principle:

$$\begin{aligned} E[\psi'] &\equiv \langle \psi' | \hat{T} + \hat{V}_{int} + \hat{V}_{ext} | \psi' \rangle \\ &= E[n'(\vec{r})] \\ &= \int n'(\vec{r}) V'_{ext}(\vec{r}) d\vec{r} + F[n'(\vec{r})] \\ &> E[\psi_0] \\ &= \int n_0(\vec{r}) V_{ext}(\vec{r}) d\vec{r} + F[n_0(\vec{r})] \\ &= E[n_0(\vec{r})] \end{aligned} \quad (3.25)$$

Thus the energy functional  $E[\psi'] \equiv \int n(\vec{r}) V_{ext}(\vec{r}) d\vec{r} + F[n(\vec{r})]$  evaluated for the correct ground state density  $n_0(\vec{r})$  is indeed lower than the value of this functional for any other density  $n(\vec{r})$ . Therefore by minimizing the total energy functional of the system with respect to variations in the density  $n(\vec{r})$ , one would find the exact ground state density and energy [82]. This functional only determines ground state properties, it doesn't provide any guidance concerning excited states.

### 3.5 Kohn-Sham (KS) equation

An inventive indirect method of mono-electronic equation for the kinetic-energy functional  $T[n(\vec{r})]$  was developed by Kohn and Sham in 1965 as Kohn-Sham (KS) method [83]. Kohn and Sham proposed introducing orbitals into the problem in such a way that the kinetic energy can be computed simply to good accuracy, leaving a small residual correction that is handled separately. It is convenient to begin with

## Density Functional Theory

---

the exact formula for the ground-state kinetic energy,

$$T = \sum_i^N a_i \langle \psi_i | -\frac{1}{2} \nabla^2 | \psi_i \rangle \quad (3.26)$$

where,  $\psi_i$  and  $a_i$  respectively, natural spin orbitals and their occupation numbers. We are assured from the Hohenberg-Kohn theory that this  $T$  is a functional of the total electron density.

$$n(\vec{r}) = \sum_i^N a_i |\psi_i(\vec{r})|^2 \quad (3.27)$$

Kohn and Sham showed that one can build a theory using simpler formulas, namely,

$$T_s[n] = \sum_i^N \langle \psi_i | -\frac{1}{2} \nabla^2 | \psi_i \rangle \quad (3.28)$$

and

$$n(\vec{r}) = \sum_i^N |\psi_i(\vec{r})|^2 \quad (3.29)$$

This representation of kinetic energy and density holds true for the determinantal wave function that exactly describes  $N$  non-interacting electrons. In analogy with the Hohenberg-Kohn definition of the universal functional  $F_{HK}[n]$ , Kohn and Sham invoked a corresponding non-interacting reference system, with the Hamiltonian,

$$\hat{H}_s = \sum_i^N \left( \frac{1}{2} \nabla_i^2 \right) + \sum_i^N \nu_s(\vec{r}) \quad (3.30)$$

in which there are no electron-electron repulsion terms and for which the ground state electron energy is exactly  $n$ . For this system, there will be an exact determinantal ground-state wave function,

$$\psi_s = \frac{1}{\sqrt{N!}} \det[\psi_1 \psi_2 \dots \psi_N] \quad (3.31)$$

where  $\psi_i$  are the  $N$  lowest eigenstates of the one-electron Hamiltonian  $\hat{h}_s$ :

$$\hat{h}_s \psi_i = \left[ -\frac{1}{2} \nabla^2 + \nu_s(\vec{r}) \right] \psi_i = \epsilon_{me} \psi_i \quad (3.32)$$

## Density Functional Theory

---

The kinetic energy is  $T_s(n)$  given by equation (3.28).

$$T_s[n] = \langle \psi_s | \sum_i^N (-\frac{1}{2} \nabla_i^2) | \psi_i \rangle = \sum_{i=1}^N \langle \psi_i | -\frac{1}{2} \nabla^2 | \psi_i \rangle \quad (3.33)$$

The quantity  $T_s[n]$ , although uniquely defined for any density, is still not the exact kinetic energy functional. Kohn-Sham set up a problem of interest in such a way that  $T_s[n]$  is it's kinetic energy component. To produce the desired separation out of  $T_s[n]$  as the kinetic energy component, we write the equation as

$$F[n] = T_s[n] + J[n] + E_{xc}[n]. \quad (3.34)$$

where,

$$E_{xc}[n] = T[n] - T_s[n] + V_{ee}[n] - J[n] \quad (3.35)$$

Here the quantity  $E_{xc}[n]$  is called exchange-correlation energy. It contains the difference between  $T$  and  $T_s$  and non-classical part of  $V_{ee}[n]$ . The Euler equation becomes,

$$\mu = \nu_{eff}(\vec{r}) + \frac{\delta T_s[n]}{\delta n(\vec{r})} \quad (3.36)$$

where KS effective potential is defined by,

$$\begin{aligned} \nu_{eff}(\vec{r}) &= \nu(\vec{r}) + \frac{\delta J[n]}{\delta n(\vec{r})} + \frac{\delta E_{xc}[n]}{\delta n(\vec{r})} \\ &= \nu(\vec{r}) + \int \frac{n(\vec{r}')}{|\vec{r} - \vec{r}'|} dr' + \nu_{xc}(\vec{r}) \end{aligned} \quad (3.37)$$

with the exchange-correlation potential

$$\nu_{xc}(\vec{r}) = \frac{\delta E_{xc}[n]}{\delta n(\vec{r})} \quad (3.38)$$

For a system of non-interacting electrons moving in the external potential  $\nu_s(\vec{r}) = \nu_{eff}(\vec{r})$ . Therefore, for a given  $\nu_{eff}(\vec{r})$ , one obtains the  $n(\vec{r})$  that satisfies equation (3.38) simply by solving the  $N$ -one electron equations,

$$[-\frac{1}{2} \nabla^2 + \nu_{eff}(\vec{r})] \psi_i = \epsilon_{me} \psi_i \quad (3.39)$$

where  $\epsilon_{me}$  is the eigenvalue of monoelectron equation and setting

$$n(\vec{r}) = \sum_i^N |\psi_i(\vec{r})|^2 \quad (3.40)$$

Equations (3.37) and (3.40) are celebrated Kohn-Sham equations.

The Kohn-Sham equations derived above that are summarized in the flow chart in Figure: 3.1. They are a set of Schrödinger like independent particle equations which must be solved subject to the condition that the effective potential  $\nu_{eff}$  and the density  $n(\vec{r})$  are consistent. After solving Kohn-Sham equations, we will have a set of single electron wave functions. These wave functions can be used to calculate the new electron density. As an input, the new electron density is fed into the next cycle. Finally, after each iteration, compare the differences in calculated electron densities. If the difference in electron density between consecutive iterations is less than a suitably determined convergence threshold, the solution of the Kohn-Sham equations is deemed self-consistent. The predicted electron density has now been converted to the ground state electron density, which can be used to compute the total energy of the system.

### 3.5.1 Solving Kohn-Shan equation

In a condensed matter system the KS equation gives a way to obtain the exact density and energy of the ground state. The process starts with an initial electron density  $n(\mathbf{r})$ , usually a superposition of atomic electron density, then the effective KS potential  $\nu_{eff}$  is calculated and the KS equation is solved with single-particle eigenvalues and wave functions, a new electron density is then calculated from the wave functions. This is usually done numerically through some self consistent iteration as shown in above flowchart. Self-consistent condition can be the change of total energy or electron density from the previous iteration or total force acting on atoms is less than some chosen small quantity, or a combination of these individual conditions. If the self-consistency is not achieved, the calculated electron density will be mixed with electron density from previous iterations to get a new electron

density. A new iteration will start with the new electron density. This process continues until selfconsistency is reached. After the self-consistency is reached, various quantities can be calculated including total energy, forces, stress, eigenvalues, electron density of states, band structure, etc..

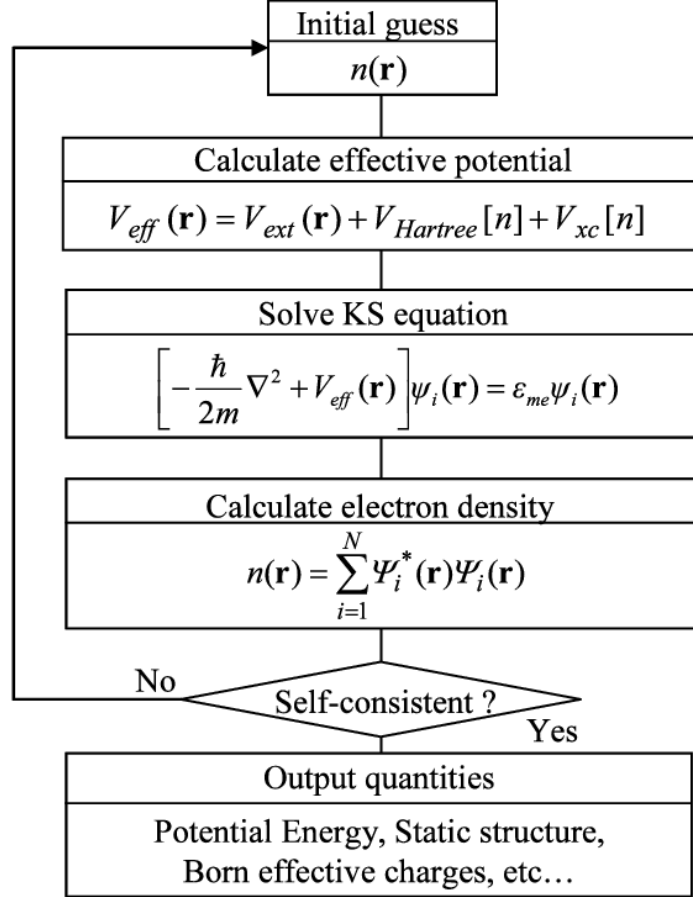


**Figure 3.1:** Flowchart of self-consistency loop for solving Kohn-Sham equation

### 3.6 The exchange-correlation (XC) functional

The exchange-correlation functional is at the core of density functional theory (DFT) that determines the accuracy of DFT in describing the interactions among electrons/ions in solids and molecules [84]. The crucial quantity in the Kohn-Sham approach is the exchange-correlation energy which is expressed as a functional of the density  $E_{xc}[\vec{n}]$ . The exchange-correlation potential for a homogeneous electron gas (HEG) at the electron density observed at position  $\vec{r}$ . This approximation uses only the local density to define the approximate exchange-correlation functional,

hence called local density approximation (LDA) and widely used.

$$\begin{aligned}
 E_{xc}^{LDA}(\vec{r}) &= \int n(\vec{r}\epsilon)_{xc}^{hom} n(\vec{r}) d\vec{r} \\
 &= \int [n(\vec{r}\epsilon)_x^{hom} n(\vec{r}) + n(\vec{r}\epsilon)_c^{hom} n(\vec{r})] d\vec{r} \\
 &= E_{xc}^{LDA}[n(\vec{r})]
 \end{aligned} \tag{3.41}$$

The LDA is very simple, corrections to the exchange-correlation energy due to the inhomogeneities in the electronic density are ignored. Because of exchange-correlation energy of inhomogeneous charge density can significantly different from HEG result. This leads to development of various generalized-gradient approximation (GGA). In the GGA approximation, the local electron density and local gradient in the electron density are included in the exchange and correlation energies. One example of GGA functional used in DFT is the Perdew-Burke Ernzerhof (PBE) functional. It is formulated as

$$E_{xc}^{PBE} = E_{xc}^{LDA} + E_c^{PBE}. \tag{3.42}$$

Where,  $E_{xc}^{PBE}$  is the exchange correlation energy calculated using the PBE functional.  $E_{xc}^{LDA}$  is the exchange correlation energy calculated using LDA approximation and  $E_c^{PBE}$  is the correlation energy term specific to the PBE functional.

The exchange correlation potential was solved by GGA functional that underestimates the band gap value. Therefore, the modified Becke-Johnson exchange potential and LDA correlation by Tran and Blaha in 2009 (TB-mBJ) allows the calculation of band gaps with an accuracy similar to very expensive *GW* calculations.

### 3.7 Local Density Approximation (LDA)

The Kohn Sham equation while exactly incorporating the kinetic energy  $T_s[n]$ , still leave the exchange correlational functional  $E_{xc}[n]$  unsettled. In Kohn Sham equation let us introduce the local density approximation proposed by Kohn and Sham. The kinetic energy  $T_s[n]$  is rigorously treated in the Kohn Sham scheme, we can use the uniform electron gas formula solely for the unknown part of the rest of the

## Density Functional Theory

---

energy functional. Thus we introduce the local density approximation (LDA) for exchange and correlation energy.

$$E_{xc}^{PBE}[n] = \int n(\vec{r})\epsilon_{xc}(n)d\vec{r} \quad (3.43)$$

Where,  $\epsilon_{xc}[n]$  indicates the exchange and correlation energy per particle of a uniform electron gas of density  $n$ . The corresponding exchange correlation potential then becomes,

$$\begin{aligned} V_{xc}^{LDA}(\vec{r}) &= \frac{E_{xc}^{PBE}[n]}{\delta n(\vec{r})} \\ &= \epsilon_{xc}(n(\vec{r})) + n(\vec{r})\frac{E_{xc}[n]}{\delta n(\vec{r})} \end{aligned} \quad (3.44)$$

and the Kohn Sham equations read, This self consistent solution defines the KS local density approximation, which in the literature is usually simply called Local Density Approximation (LDA) method. The function  $\epsilon_{xc}[n]$  can be divided into exchange and correlation contributions,

$$\epsilon_{xc}(n) = \epsilon_x(n) + \epsilon_c(n) \quad (3.45)$$

The exchange part is already known given by the Dirac exchange energy functional.

$$\epsilon_x(n) = -C_x n^{\frac{1}{3}}(\vec{r}) \quad (3.46)$$

where,

$$C_x = \frac{3}{4}\left(\frac{3}{\pi}\right)^{\frac{1}{3}} \quad (3.47)$$

### 3.8 Local Spin Density Approximation (LSDA)

The spin-density-functional theory is the necessary generalization for systems in the presence of an external magnetic field. It is also exceedingly important for systems in the absence of a magnetic field, because it allows one to build more physics into the approximate exchange-correlation functional through its spin dependence. In the presence of a magnetic field  $B(\vec{r})$  that acts only on the spins of the electrons,

## Density Functional Theory

---

the Hamiltonian of the system becomes,

$$H = -\frac{1}{2} \sum_i^N \nabla_i^2 + \sum_i^N V(\vec{r}_i) + \sum_{i<j}^N \frac{1}{r_{ij}} + 2\beta_e \sum_i^N B(\vec{r}_i) \cdot \vec{S}_i \quad (3.48)$$

Where,  $\beta_e = \frac{e\hbar}{2mc}$  is the Bohr magneton and  $\vec{S}_i$  is the electron angular momentum vector for the  $i^{\text{th}}$  electron. The added magnetic interaction is still a one-electron operator, just like the nuclear potential  $V(\vec{r})$ . We can combine terms in the following convenient way:

$$\hat{V} = \sum_i^N V(\vec{r}_i) + 2\beta_e \sum_i^N B(\vec{r}_i) \cdot \vec{S}_i \quad (3.49)$$

$$= \int v(\vec{r}) \hat{n}(\vec{r}) d\vec{r} - \int B(\vec{r}) \hat{m}(\vec{r}) d\vec{r} \quad (3.50)$$

where  $\hat{n}(\vec{r})$  is the operator for electron density,

$$\hat{n}(\vec{r}) = \sum_i^N \delta(\vec{r} - \vec{r}_i) \quad (3.51)$$

and  $\hat{m}(\vec{r})$  is the operator for the electron magnetization density,

$$\hat{m}(\vec{r}) = -2\beta_e \sum_i^N S_i \delta(\vec{r} - \vec{r}_i) \quad (3.52)$$

Both  $\hat{n}(\vec{r})$  and  $\hat{m}(\vec{r})$  are local operators. The expectation value of  $\hat{V}$  for the state  $|\psi\rangle$  is given by,

$$\langle \psi | \hat{V} | \psi \rangle = \int v(\vec{r}) n(\vec{r}) d\vec{r} - \int B(\vec{r}) m(\vec{r}) d\vec{r} \quad (3.53)$$

where the electron density is given by,

$$n(\vec{r}) = \langle \psi | \hat{n}(\vec{r}) | \psi \rangle \quad (3.54)$$

and the magnetization density by,

$$m(\vec{r}) = \langle \psi | \hat{m}(\vec{r}) | \psi \rangle \quad (3.55)$$

## Density Functional Theory

---

We shall discuss only the simple case of z-direction  $b(\vec{r})$ . We then have,

$$\langle \psi | \hat{V} | \psi \rangle = \int v(\vec{r})n(\vec{r})d\vec{r} - \int b(\vec{r})m(\vec{r})d\vec{r} \quad (3.56)$$

where,

$$\begin{aligned} m(\vec{r}) &= -2\beta_e \langle \psi | \sum_i^N S_z(i) \delta(\vec{r} - \vec{r}_i) | \psi \rangle \\ &= \beta_e [n^\beta(\vec{r}) - n^\alpha(\vec{r})] \end{aligned} \quad (3.57)$$

We obtain the spin-density-functional theory by breaking the minimum search for the ground-state energy into two steps. Namely,

$$E_0 = \min_{\psi} \langle \psi | T + V_{ee} + \sum_i^N U(\vec{r}_i) + 2\beta_e \sum_i^N b(\vec{r}_i) \cdot S_z(i) | \psi \rangle \quad (3.58)$$

$$= \min_{n^\alpha, n^\beta} \left\{ \min_{\psi \rightarrow n^\alpha, n^\beta} \langle \psi | T + V_{ee} \rangle + \int [v(\vec{r})n(\vec{r}) - \int b(\vec{r})m(\vec{r})d\vec{r}] \right\} \quad (3.59)$$

$$= \min_{n^\alpha, n^\beta} \left\{ F[n^\alpha, n^\beta] + \int [(V(\vec{r}) - \beta_e b(\vec{r}))n^\alpha(\vec{r}) + \beta_e b(\vec{r})n^\beta(\vec{r})]d\vec{r} \right\} \quad (3.60)$$

where,

$$F[n^\alpha, n^\beta] = \min_{\psi \rightarrow n^\alpha, n^\beta} \langle \psi | T + V_{ee} | \psi \rangle \quad (3.61)$$

This provides constrained-search formulation of the universal functional  $F[n^\alpha, n^\beta]$ . The functional  $F[n^\alpha, n^\beta]$  searches all  $\psi$  that yield the input  $n^\alpha(\vec{r})$  and  $n^\beta(\vec{r})$ , then  $F[n^\alpha, n^\beta]$  assumes the minimum of  $\langle F + V_{ee} \rangle$ . The last equality of (8.1.10) is the basis of the spin-density-functional theory:  $n^\alpha$  and  $n^\beta$  are all that are needed to describe the ground state of the many-electron system in the presence of a magnetic field  $b(\vec{r})$ . However,  $F[n^\alpha, n^\beta]$  is unknown, and approximation is necessary for the theory to be implemented.

The Kohn-Sham method can now be introduced to rigorously handle the kinetic energy contribution to  $F[n^\alpha, n^\beta]$ ,

$$F[n^\alpha, n^\beta] = T_s[n^\alpha, n^\beta] + J[n^\alpha + n^\beta] + E_{xc}[n^\alpha, n^\beta] \quad (3.62)$$

where,  $T_s[n^\alpha, n^\beta]$  is the Kohn-Sham kinetic-energy functional corresponding to a

## Density Functional Theory

---

system of non-interacting electrons with densities  $n^\alpha$  and  $n^\beta$  and  $E_{xc}[n^\alpha, n^\beta]$  is the exchange correlation energy functional. A constrained search definition of  $T_s$  can also be given,

$$T_s[n^\alpha, n^\beta] = \min \sum_{i\alpha} n_{i\alpha} \int d\vec{r} \phi_{i\alpha}^*(\vec{r}) \left(\frac{1}{2} \nabla^2\right) \phi_{i\alpha}(\vec{r}) \quad (3.63)$$

where the minimization is over the set of  $n_{i\alpha}$  and  $\phi_{i\alpha}$ , with constraints,

$$\sum_i n_{i\alpha} |\phi_{i\alpha}(\vec{r})|^2 = n^\alpha(\vec{r}) \quad (3.64)$$

$$\sum_i n_{i\beta} |\phi_{i\beta}(\vec{r})|^2 = n^\beta(\vec{r}) \quad (3.65)$$

We may express the energy (3.55) as a functional of the orbitals  $\phi_{i\alpha}$ ,

$$\begin{aligned} E[n^\alpha, n^\beta] &= \sum_{i\alpha} n_{i\alpha} \int d\vec{r} \phi_{i\alpha}^*(\vec{r}) \left(-\frac{1}{2} \nabla^2\right) \phi_{i\alpha}(\vec{r}) + J[n^\alpha + n^\beta] + E_{xc}[n^\alpha, n^\beta] \\ &+ \int [(V(\vec{r}) + \beta_e b(\vec{r}))n^\alpha(\vec{r}) + (V(\vec{r}) - \beta_e b(\vec{r}))n^\beta(\vec{r})] d(\vec{r}) \end{aligned} \quad (3.66)$$

The variational search for the minimum of  $E[n^\alpha, n^\beta]$  can then be carried out through orbitals, subject to normalization constraints,

$$\int \phi_{i\alpha}^*(\vec{r}) \phi_{i\alpha}(\vec{r}) d\vec{r} = 1 \quad (3.67)$$

The resulting Kohn-Sham equations are,

$$\hat{h}_{eff}^\alpha \phi_{i\alpha}(\vec{r}) = \left[-\frac{1}{2} \nabla^2 + V_{eff}^\alpha\right] \phi_{i\alpha}(\vec{r}) = \epsilon_{i\alpha} \phi_{i\alpha}(\vec{r}) \quad (3.68)$$

and

$$\hat{h}_{eff}^\beta \phi_{j\beta}(\vec{r}) = \left[-\frac{1}{2} \nabla^2 + V_{eff}^\beta\right] \phi_{j\beta}(\vec{r}) = \epsilon_{j\beta} \phi_{j\beta}(\vec{r}) \quad (3.69)$$

where the spin-dependent effective potentials are,

$$v_{eff}^\alpha(\vec{r}) = v(\vec{r}) + \int \frac{n(\vec{r}')}{|\vec{r} - \vec{r}'|} d\vec{r}' + \frac{\delta E_{xc}[n^\alpha, n^\beta]}{\delta n^\alpha(\vec{r})} + \beta_e b(\vec{r}) \quad (3.70)$$

$$v_{eff}^{\beta}(\vec{r}) = v(\vec{r}) + \int \frac{n(\vec{r}')}{|\vec{r} - \vec{r}'|} d\vec{r}' + \frac{\delta E_{xc}[n^{\alpha}, n^{\beta}]}{\delta n^{\beta}(\vec{r})} + \beta_e b(\vec{r}) \quad (3.71)$$

In equations (3.65) and (3.66), the number of electrons with  $\alpha$  spin and  $\beta$  spin,

$$N^{\alpha} = \int n^{\alpha}(\vec{r}) d\vec{r} \quad (3.72)$$

and

$$N^{\beta} = \int n^{\beta}(\vec{r}) d\vec{r} \quad (3.73)$$

need also to be varied to achieve minimum total energy under the constraint,

$$N = N^{\alpha} + N^{\beta} \quad (3.74)$$

With the spin-polarized Kohn-Sham equations, the kinetic energy is handled exactly and only the exchange-correlation energy remains to be determined. The exchange-correlation contribution can be separated into exchange and correlation pieces,

$$E_{xc}[n^{\alpha}, n^{\beta}] = E_x[n^{\alpha}, n^{\beta}] + E_c[n^{\alpha}, n^{\beta}] \quad (3.75)$$

where the exchange part is defined as,

$$E_x[n^{\alpha}, n^{\beta}] = -\frac{1}{2} \int \int \frac{1}{r_{12}} \{ |n_1^{\alpha, \alpha}(\vec{r}_1, \vec{r}_2)|^2 + |n_1^{\beta, \beta}(\vec{r}_1, \vec{r}_2)|^2 \} d\vec{r}_1 d\vec{r}_2 \quad (3.76)$$

with

$$n_1^{\alpha, \alpha}(\vec{r}_1, \vec{r}_2) = \sum_i n_{i\alpha} \phi_{i\alpha}(\vec{r}_1) \phi_{i\alpha}^*(\vec{r}_2) \quad (3.77)$$

$$n_1^{\beta, \beta}(\vec{r}_1, \vec{r}_2) = \sum_i n_{i\beta} \phi_{i\beta}(\vec{r}_1) \phi_{i\beta}^*(\vec{r}_2) \quad (3.78)$$

The  $n_{i\alpha}$  and  $\phi_{i\alpha}$  are those giving the Kohn-Sham kinetic energy, they are determined by  $p^{\alpha}$  and  $p^{\beta}$ .

$$E_x[n^{\alpha}, n^{\beta}] = \frac{1}{2} E_x[n^{\alpha}, n^{\alpha}] + \frac{1}{2} E_x[n^{\beta}, n^{\beta}] \quad (3.79)$$

$$= \frac{1}{2} E_x^0[2n^{\alpha}] + \frac{1}{2} E_x^0[2n^{\beta}] \quad (3.80)$$

where,

$$E_x^0[n] = E_x\left[\frac{1}{2}n, \frac{1}{2}n\right] \quad (3.81)$$

The Dirac local-density approximation (LDA) for exchange is for the spin-compensated case. Thus from above equations, we obtain the local spin-density approximation (LSDA) for the exchange energy functional,

$$E_x^{LSDA}[n^\alpha, n^\beta] = 2^{\frac{1}{3}}C_x \int [(n^\alpha)^{\frac{4}{3}} + (n^\beta)^{\frac{4}{3}}]d\vec{r} \quad (3.82)$$

### 3.9 Generalized Gradient Approximation (GGA)

The LDA neglects the inhomogeneties of the real charge density which could be very different from the HEG. The XC energy of inhomogeneous charge density can be significantly different from the HEG result. This leads to be the development of verious generalized-gradient approximations (GGA) which include density gradient corrections and higher spatial derivatives of the electron density and give better result than LDA in many cases. Three most widely used GGA's are the from proposed by Becke [85], Perdew et al. [86], Burke and Enzerhof [87]. The definition of the XC energy functional of GGA is the generalized form in the equation of LSDA to include corrections ,

$$E_{XC}^{LSDA}[n_\downarrow(r), n_\uparrow(r)] = \int n(r)\epsilon_{XC}^{hom}[n_\downarrow(r), n_\uparrow(r)]dr \quad (3.83)$$

Where XC energy density  $\epsilon_{XC}^{hom}(n(r))$  is a function of the density alone and is composed into exchange energy density  $\epsilon_X^{hom}(n(r))$  and correlation energy density  $\epsilon_C^{hom}(n(r))$  . So that the XC energy functional is decomposed into exchange energy function  $E_X^{LDA}(n(r))$  linearly. From density gradient  $\nabla(\vec{r})$  as,

$$\begin{aligned} E_{XC}^{GGA}[n_\downarrow(r), n_\uparrow(r)] &= \int n(r)\epsilon_{XC}^{hom}[n_\downarrow(r), n_\uparrow(r), |\nabla \uparrow(r)|, |\nabla \downarrow(r)|, \dots]dr \\ &= \int n(r)\epsilon_X^{hom}n(r)F_{XC}[n_\downarrow(r), n_\uparrow(r), |\nabla \uparrow(r)|, |\nabla \downarrow(r)|, \dots]dr \end{aligned} \quad (3.84)$$

## Density Functional Theory

---

Where  $F_{XC}$  is dimensionless and  $\epsilon_{XC}^{hom}n(r)$  is the exchange energy density of the unpolarized HEG. FXC can be decomposed linearly into exchange contribution  $F_{XC} = F_X + F_C$ . Generally GGA works better than LDA, in predicting binding energy of molecules and bond length, crystal lattice constants, especially the system where charge density varied rapidly. In case of ionic crystal, GGA overcorrects LDA results where the lattice constants of LDA fit well than GGA. But in case of transition metal oxides and rare-earth element, both LDA and GGA perform badly. This drawback leads to approximations beyond LDA and GGA.

### 3.10 LDA+U method

Strongly correlated system usually contain transition metal or rare-earth metal ions with partially filled d or f shells. Because of the orbital-independent potentials in LSDA and GGA, they cannot properly describe such systems. The total energy in LSDA+U [88] method is given by,

$$E_{tot}^{LDA+U}[\rho_\sigma(r), n_\sigma] = E^{LSDA}[\rho_\sigma(r)] + E^U[n_\sigma] - E_{dc}[n(r)] \quad (3.85)$$

where,  $\sigma =$  spin indexes  $\rho(r) =$  electron density for spin- electrons  $n =$  density matrix of f or d electron for spin- $\sigma$  electrons  $E^{LSDA}[\rho_\sigma(r)] =$  standard LSDA energy functional  $E^U[n(r)] =$  electron-electron coulomb interaction energy. The last term is double counting term which remove the average LDA energy contribution of d or f electrons from the LDA energy

$$E_{dc}[n(r)] = \frac{1}{2}UN(N-1) - \frac{1}{2}J[N_\uparrow(N_\uparrow-1) + N_\downarrow(N_\downarrow-1)] \quad (3.86)$$

where,  $N = N_\uparrow + N_\downarrow$ . U and J are coulomb and exchange parameters. If exchange and non sphericity is neglected then,

$$E_{tot}^{LDA+U} = E_{LDA} + \frac{1}{2}U \sum_{i \neq j} n_i n_j - \frac{1}{2}UN(N-1) \quad (3.87)$$

## Density Functional Theory

---

The orbital energies  $\epsilon_i$  are derivative of above equation with respect to orbital occupations  $n_i$ :

$$\epsilon_i = \frac{\partial E}{\partial n_i} = \epsilon_{LDA} + U\left(\frac{1}{2} - n_i\right) \quad (3.88)$$

For  $n_i = 1$ , LDA orbital energies are shifted by  $-\frac{U}{2}$  and by  $\frac{U}{2}$  and by for unoccupied orbitals ( $n_i = 0$ ), resulting the upper and lower Hubbard bands, which opens a gap at the Fermi energy in transition metal oxides. In case of double counting term, it has two different treatment: AMF and FLL. The former is most suitable for small U system [89] and the latter for large U system [90]. The energies for double counting is given by [91],

$$E_{dc}^{AMF} = \frac{1}{2}UN^2 - \frac{U + 2lJ}{2l + 1} \frac{1}{2} \sum_{\sigma} N_{\sigma}^2 \quad (3.89)$$

and

$$E_{dc}^{AMF} = \frac{1}{2}UN(N - 1) - \frac{1}{2}J \sum_{\sigma} N_{\sigma}(N_{\sigma-1}) \quad (3.90)$$

where,  $\frac{N}{2(2l+1)}$  = average occupation of the correlated orbitals,

$\frac{N_{\sigma}}{2l+1}$  = average occupation of a single spin of the correlated orbital.

# Results and Discussion

---

### 4.1 Computational frameworks

The structural, mechanical, optoelectronic, and thermoelectric properties of double perovskites  $K_2AgXI_6$  ( $X = Sb, Bi$ ) are studied using the Full Potential Linear Augmented Plane Wave (FP-LAPW) method, based on Density Functional Theory (DFT) and incorporated in the WIEN2k code [92]. A reliable analytical parameter, the Goldschmidt tolerance factor, was used to analyze the stable structures of the perovskite materials. The Perdew-Burke-Ernzerhof and Generalized Gradient Approximation (PBE-GGA) functional was utilized to compute structural characteristics, while the modified Becke and Johnson (mBJ) potential functional was employed to compute the optoelectronic and thermal properties of the compounds [87]. WIEN2k is a widely recognized and efficient software package for performing DFT calculations, offering robust capabilities for studying the electronic, optical, and mechanical properties of materials. Additionally, we have effectively employed the Tran and Blaha modified Becke and Johnson potential (TB-mBJ), leading to a notable improvement in bandgap accuracy [93]. The BoltzTraP code [94] was used to investigate the thermoelectric characteristics of the materials. We set  $R_{MT} \times K_{max} = 8$ , where  $R_{MT}$  is the smallest muffin-tin radius and  $K_{max}$  is the largest recipro-

## Results and Discussion

---

cal lattice vector used in the expansion of the plane wave functions. The largest expansion Fourier of charge density was up to  $G_{max} = 24$ , and angular momentum vector  $l_{max} = 10$ . Moreover, the number of  $k$ -point is selected to 4000 in Brillouin zone. When the total energy and charge of the system is stable within the energy of 0.00001 Ry and 0.001 e respectively, then self-consistent equation is converged. For mechanical properties, Charpin method is applied while Kramer-Krong model was used to calculate the optical characteristics [95].

### 4.2 Structural properties

The structural stability of materials is extremely valuable in determining their physical or chemical performance. We calculated the structures of the alkali metal-based double perovskites  $K_2AgXI_6$  ( $X = Sb, Bi$ ), which belong to the space group  $Fm\bar{3}m$  (space group no: 225). These structures were optimized to eliminate strain forces among the atoms, ensuring accurate structural parameters as illustrated in Figure 4.1, where K is a alkali cation, Ag is a monovalent-transition cation, Sb/Bi is a trivalent-transition cation and I is a halide ion. Here, sky blue, violet, green and dark red colors are presenting the identity of atoms with K, Sb/Bi, Ag and I.  $K_2AgSbI_6$  and  $K_2AgBiI_6$  compounds have fourteen octahedras with (Ag Sb/BiI<sub>6</sub>) which are located at the corners and interior of the cubic structures. In the unit cell structure, K atoms have a face-centered position with an 8c Wyckoff site and fractional coordinates (0.25, 0.25, 0.25), the Sb/Bi atoms have a body-centered position with a 4b Wyckoff site and fractional coordinates (0.5, 0.5, 0.5), Ag atoms are located in the corner positions with a 4a Wyckoff site and fractional coordinates (0, 0, 0) and I atoms have face-centered positions with a 24e Wyckoff site and fractional coordinates (0.24808, 0, 0).

The stability of our compound is demonstrate with tolerance factor ( $\tau$ ) as well as octahedral factor ( $\mu$ ). And these components can be represents by the following equations [96, 97]:

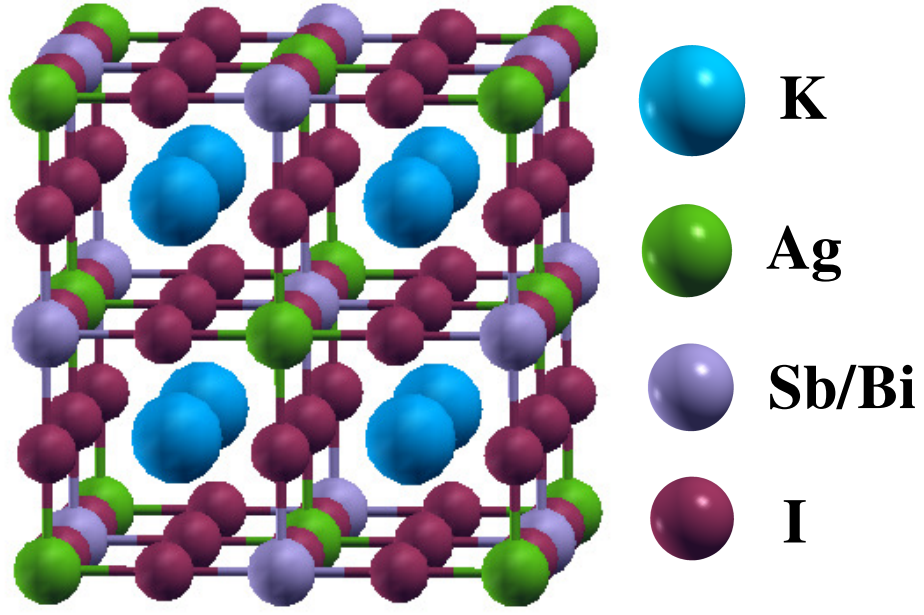


**Figure 4.1:** Crystal structure of cubic double perovskites  $K_2AgXI_6$  ( $X = Sb, Bi$ ) at 0 GPa pressure.

$$\tau = \frac{r_a + r_o}{\sqrt{2}\left(\frac{r_b + r_x}{2}\right) + r_o} \quad (4.1)$$

$$\mu = \frac{r_b + r_x}{2r_o} \quad (4.2)$$

Here,  $r_a$ ,  $r_b$ ,  $r_x$  and  $r_o$  represents the ionic radius of K, Ag, Sb/Bi and I components of double perovskite. For a stable double perovskite, the value of tolerance factor is between 0.81 to 1, while the value of octahedral factor is between 0.42 to 0.75 [97, 98]. Furthermore, research has demonstrated that materials exhibiting a tolerance factor ranging from 0.89 to 1.00 indicate a cubic structure [99]. For the material  $K_2AgXI_6$  ( $X = Sb, Bi$ ) double perovskites, the ionic radius of K, Ag, Sb, Bi, and I is used 1.33 Å, 1.15 Å, 0.76 Å, 1.03 Å and 2.20 Å respectively. The values of the tolerance factor for  $K_2AgSbI_6$  and  $K_2AgBiI_6$  have been determined to be 0.99 and 0.94 respectively. The values of the octahedral factor for  $K_2AgSbI_6$  and  $K_2AgBiI_6$  have been determined to be 0.434 and 0.495 respectively. The value ensures that the material exhibiting the form of cubic structure having the space group of  $Fm\bar{3}m$ , which corresponds to space group number 225.

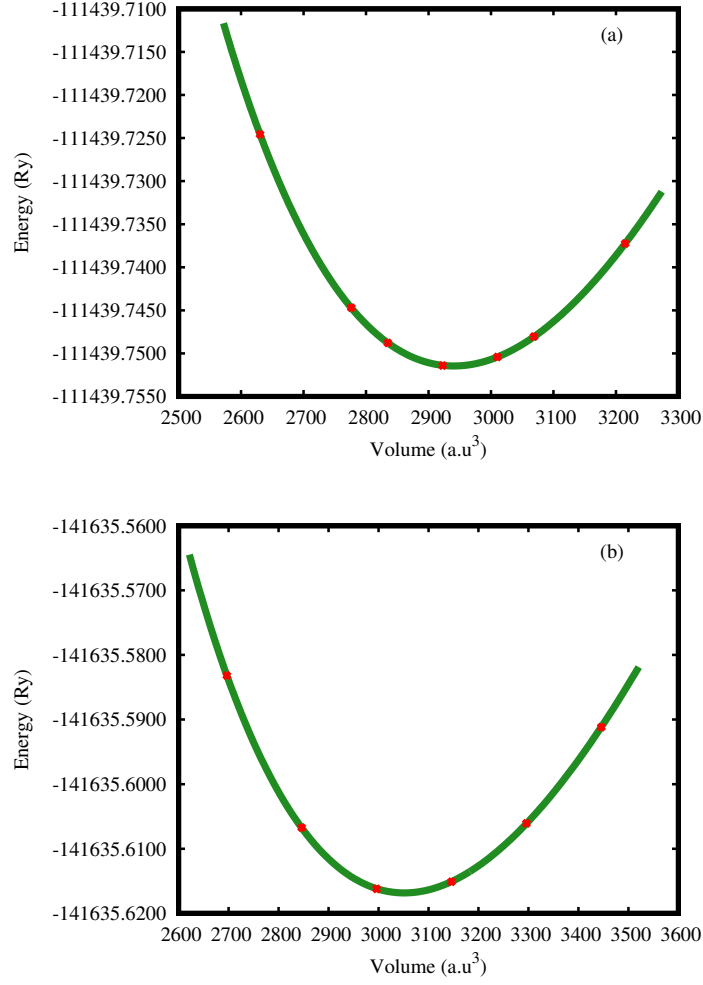


**Figure 4.2:** Energy versus unit cell volume curve of cubic double perovskite (a)K<sub>2</sub>AgSbI<sub>6</sub> and (b) K<sub>2</sub>AgBiI<sub>6</sub> at 0 GPa pressure.

To determine the most stable structure with the system's ground state energy, a volume optimization computation has been carried out. The volume optimization is provided with WIEN2k package that determines the minimum energy possessed by a system by plotting volume vs energy graph which has been shown in Figure 4.2. By volume optimization, the lattice constant has been found to be 12.03 Å for K<sub>2</sub>AgSbI<sub>6</sub> and 12.18 Å for K<sub>2</sub>AgBiI<sub>6</sub>. In the reported paper, the authors found the lattice constants to be 12.01 Å for K<sub>2</sub>AgSbI<sub>6</sub> and 12.11 Å for K<sub>2</sub>AgBiI<sub>6</sub>. In order to determine the optimized ground states of the materials being studied, the energy versus volume of a unit cell of the crystals was calculated and also absorbed that the most optimized material is K<sub>2</sub>AgBiI<sub>6</sub> because its ground state energy is less as compared to the K<sub>2</sub>AgSbI<sub>6</sub>. Furthermore, in the reported paper, the formation energy of

## Results and Discussion

---

$\text{K}_2\text{AgSbI}_6$  and  $\text{K}_2\text{AgBiI}_6$  are given -7.35 eV and -7.72 eV which exhibits the confirmation of structure stability. In the basis of formation energy  $\text{K}_2\text{AgBiI}_6$  compound is more stable as compared to the  $\text{K}_2\text{AgSbI}_6$  compound. The lattice constants are calculated by utilizing the PBE-GGA functional. The optimized crystal structure and the variation of optimization energy with unit cell volumes for  $\text{K}_2\text{AgXI}_6$  ( $X = \text{Sb, Bi}$ ) are represented in Figure 4.1 and Figure 4.2.

### 4.3 Electronic Properties

The electronic properties of a material are related to the manner in which electrons behave within it. To explore potential practical applications of the studied compounds, it is essential to investigate their band structure and density of states. Understanding electronic band structures and density of states is crucial for comprehending the physical properties of any material. Partial density of states is important to know the different angular momentum component contribution. It provides information to identify the nature of orbitals whether the states are *s*-like, *p*-like, *d*-like or *f*-like. The electronic band structure and density of states under various pressure are calculated and discussed in this section.

#### 4.3.1 Band Structure

The configuration of energy levels, or bands, occupied by electrons in a material is called band structure. The electrons in a crystalline material experience a periodic potential, which causes the electrons' energy levels to divide into discrete levels with small spacings when the atoms combine to form a crystal. The permitted energy levels in a solid create bands of states that are isolated from one another by spaces where there are no energy states. The energy scale where no electron state can remain is referred as the band gap. Other names for it are "Energy gap" and "Forbidden gap". The electronic band structure is necessary to understand the physical properties of crystalline solids which describe optical as well as transport properties.

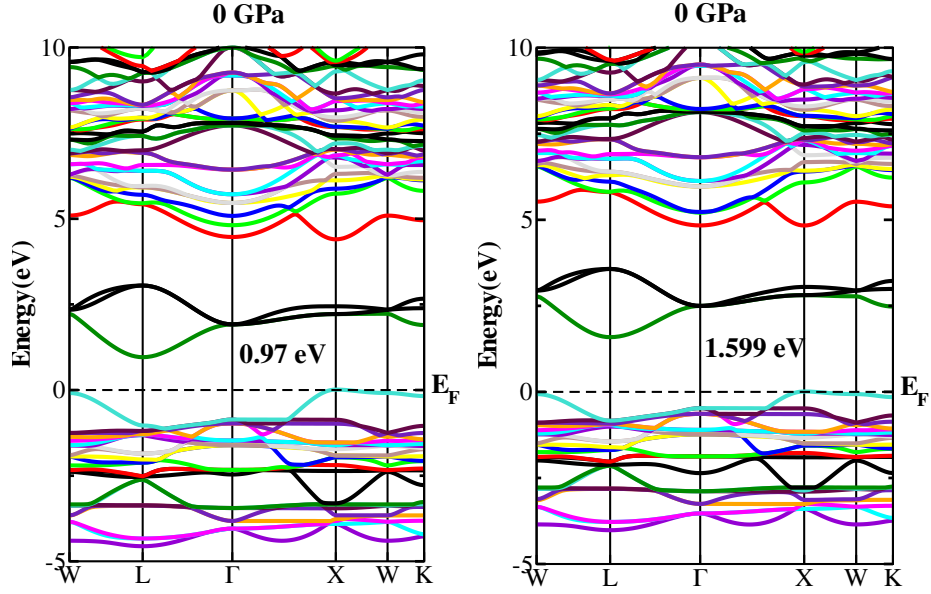


**Figure 4.3:** The band structure of  $\text{K}_2\text{AgSbI}_6$  and  $\text{K}_2\text{AgBiI}_6$  at 0 GPa pressure.

The calculated band structure plotted along with high symmetry directions in the first Brillouin zone is presented in Figure 4.3. The ability to classify materials such as metals, semimetals, insulator, and semiconductor requires an understanding of electronic band structure. From Figure 4.3, we can see that, the valance band maxima lie at W or X symmetry directions, while conduction band minima lie at L symmetry direction in the first Brillouin zone. Thus from band structures it is evident that the  $\text{K}_2\text{AgXI}_6$  ( $X = \text{Sb}, \text{Bi}$ ) double perovskite materials represent indirect band gap semiconductor because the top of valance bands and the bottom of conduction bands are located in different direction in first Brillouin zone. The calculated band gap for  $\text{K}_2\text{AgSbI}_6$  is 0.97 eV, and for  $\text{K}_2\text{AgBiI}_6$ , it is 1.599 eV at ambient pressure using the mBJ potential. Due to the higher effective mass of holes compared to electrons, there are more states at the valance band (VB) edge, which is significantly closer to the Fermi level than the conduction band (CB). Consequently, the double perovskite under investigation appears to exhibit p-type characteristics in both systems.

The effect of hydrostatic pressure on the electronic properties of these materials has been investigated under hydrostatic pressure ranging from 0-20 GPa for the  $\text{K}_2\text{AgSbI}_6$  compound and 0-50 GPa for the  $\text{K}_2\text{AgBiI}_6$  compound. Understanding

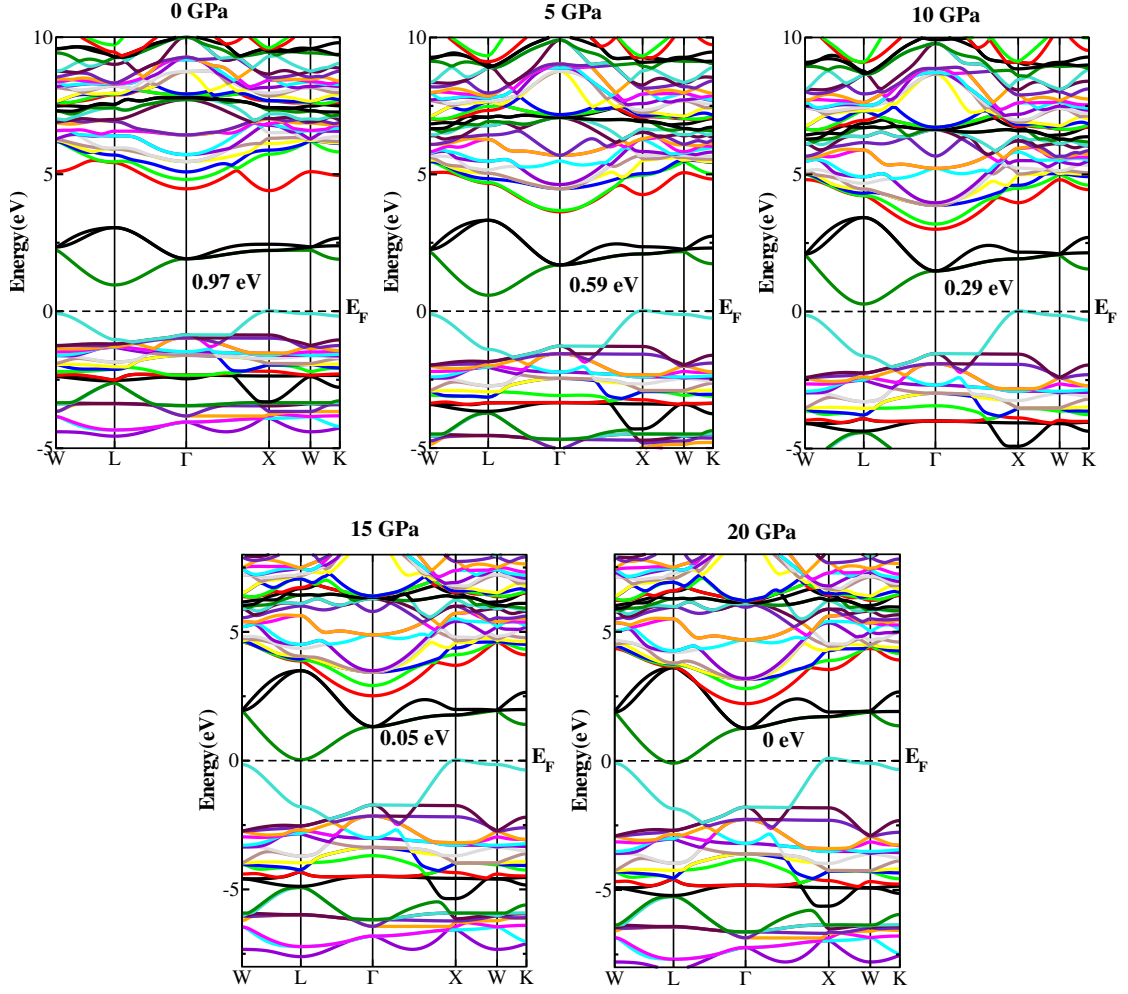


**Figure 4.4:** The band structure of  $\text{K}_2\text{AgSbI}_6$  at 0 GPa, 5 GPa, 10 GPa, 15 GPa and 20 GPa pressure.

the impact of pressure on electronic properties is crucial, as it provides valuable insights into surface characteristics. We performed band gap calculations under various pressures to study how our compounds respond to pressure changes. Table 4.1 and Table 4.2 display the band gap variations under different pressures, showing a decrease in lattice constant as pressure increases. The calculated band structures and high symmetry directions of the Brillouin zone (BZ) under different pressures are presented in Figure 4.4, Figure 4.5 and Figure 4.6 respectively. The horizontal line at 0 eV denotes the Fermi level for all pressures. As seen in Figure 4.4, for the  $\text{K}_2\text{AgSbI}_6$  compound at 0 GPa, there is an indirect band gap of 0.97 eV, as the valence band maxima and conduction band minima are located in different directions in the first Brillouin zone. When pressure is applied, the band gap significantly reduces due to

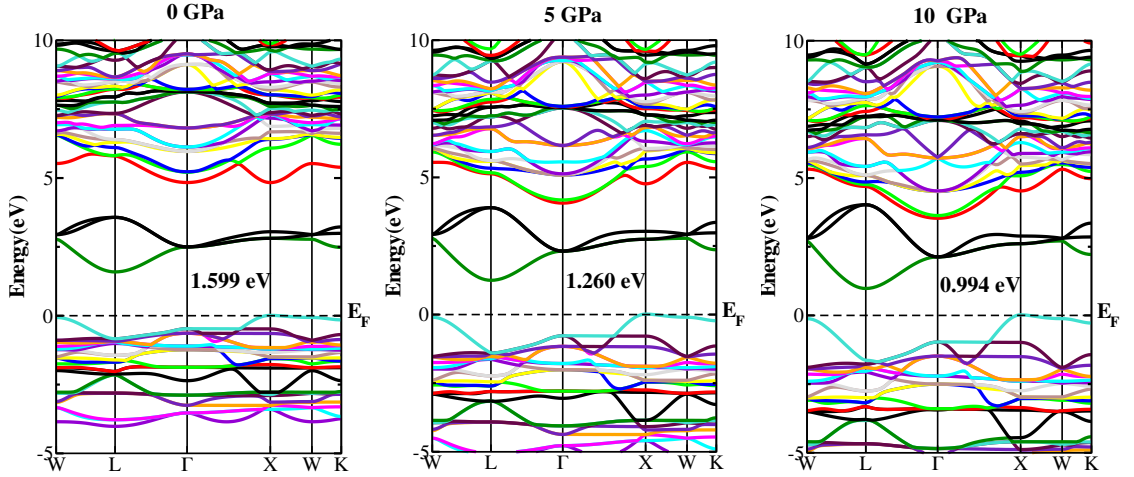


**Figure 4.5:** The band structure of  $\text{K}_2\text{AgBiI}_6$  at 0 GPa, 5 GPa, 10 GPa pressure.

**Table 4.1:** Variation of lattice constants and band gap of  $\text{K}_2\text{AgSbI}_6$  under pressure.

Pressures (GPa)	lattice constants ( $\text{\AA}$ )	Band gap (eV)
0	12.03	0.97
5	11.38	0.59
10	11.03	0.29
15	10.80	0.05
20	10.63	0.00

the expansion of the energy bands. At 20 GPa, the band gap reduces to a value of 0 eV, indicating a semiconductor-to-metallic transition.

Similarly, from Figure 4.5 and Figure 4.6, for the  $\text{K}_2\text{AgBiI}_6$  compound at 0 GPa, the indirect band gap is 1.599 eV. After applying pressure of 50 GPa, the band gap significantly reduces to a value of 0 eV, also indicating a semiconductor-to-metallic transition. Accordingly, it can be said that as pressure increases, a growing number of electrons shift from the valence to the conduction bands, enhancing conductivity and other optoelectronic properties that are better suited for device applications in both systems.

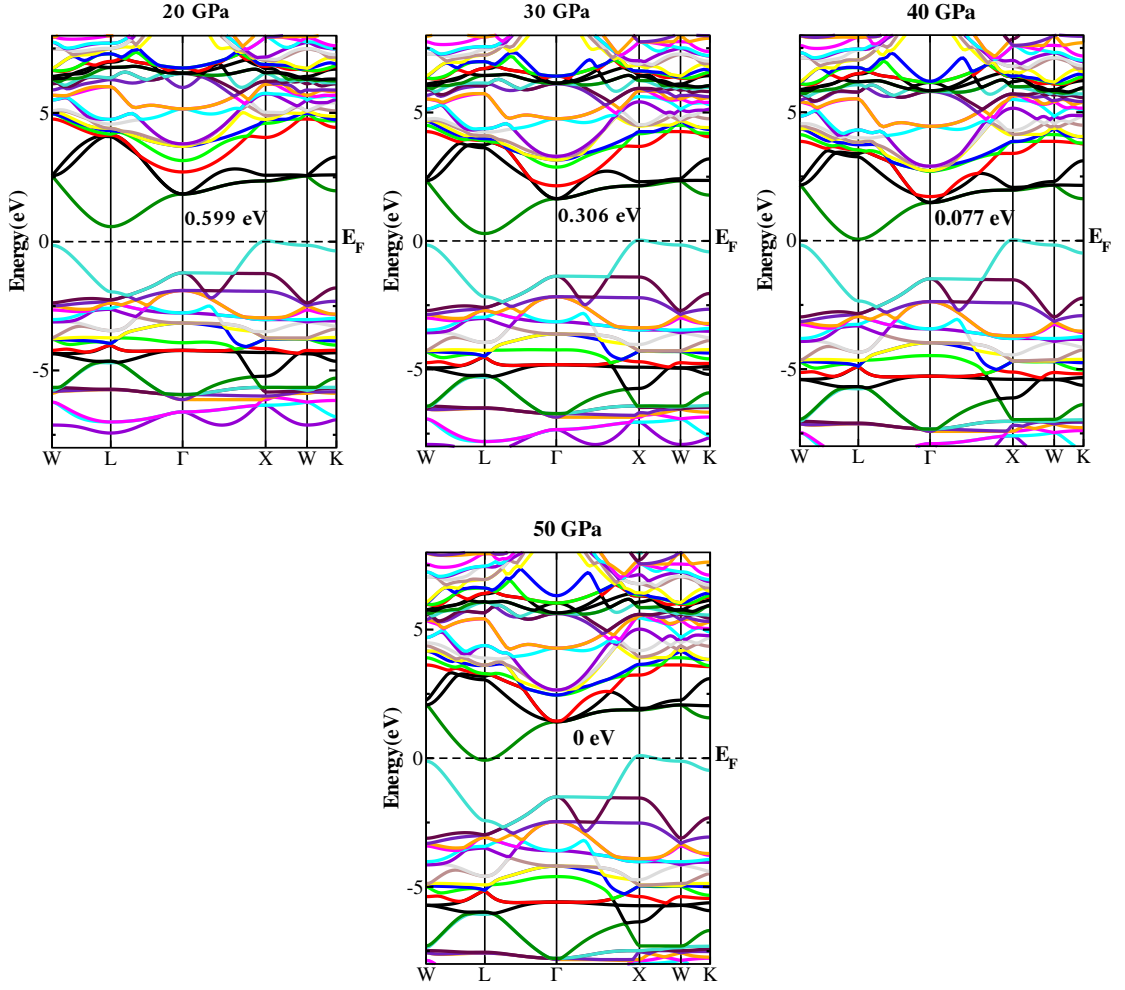


**Figure 4.6:** The band structure of  $\text{K}_2\text{AgBiI}_6$  at 20 GPa, 30 GPa, 40 GPa and 50 GPa pressure.

### 4.3.2 Density of states

The density of states (DOS) is a concept used in physics to describe the distribution of energy levels within a system, typically a solid, though it can be applied to other systems as well. It provides information about the number of states (such as electronic states or vibrational states) at each energy level within a given energy range. To analyze the potential electronic transitions from the valence to the conduction band and the hybridization among the constituent states, the total and partial density of states (DOS) of  $\text{K}_2\text{AgSbI}_6$  at ambient pressure are calculated, as illustrated in Figure 4.7. The total and partial DOS reveal the individual contributions of different atoms and states within the valence band (VB) and conduction band (CB), which corresponds to the information depicted in the band structure.

## Results and Discussion

---

**Table 4.2:** Variation of lattice constants and band gap of  $K_2AgBiI_6$  under pressure.

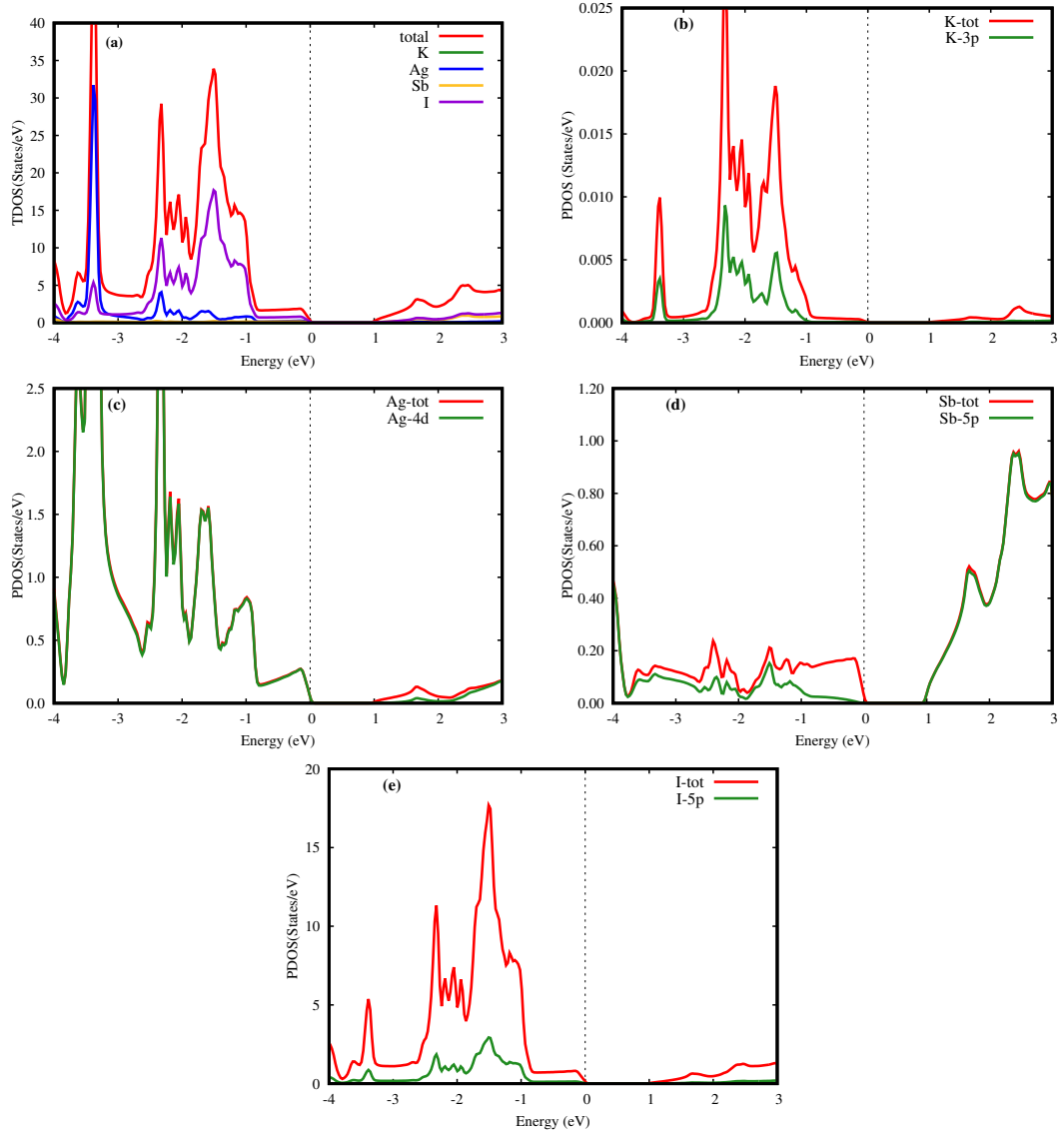
Pressures (GPa)	lattice constants ( $\text{\AA}$ )	Band gap (eV)
0	12.18	1.599
5	11.50	1.260
10	11.16	0.994
20	10.75	0.599
30	10.49	0.306
40	10.31	0.077
50	10.16	0.000

Figure 4.7 (a) represent the total density of states for  $K_2AgSbI_6$ , the contribution of elements mainly lies below the fermi level compared to above fermi level. Figure 4.7 (b,c,d,e) illustrates the partial density of states of  $K_2AgSbI_6$  which are plotted, see the role of sublevels in the hybridization. The electronic configuration of individual atom K, Ag, Sb, Bi, and I are  $[\text{Ar}] 4s^1$ ,  $[\text{Kr}] 4d^{10} 5s^1$ ,  $[\text{Kr}] 4d^{10} 5s^2 5p^3$ ,  $[\text{Xe}] 4f^{14} 5d^{10} 6s^2 6p^3$ , and  $[\text{Kr}] 4d^{10} 5s^2 5p^2$  respectively. Only the valence electrons are responsible for hybridization and inter-band transitions. In total DOS from Figure 4.7, the valence band near the fermi level mostly originated by I-5p states with a small contribution Ag-4d states. Whereas the conduction band minimum is mainly originated by I-5p states and Sb-5p states. In  $K_2AgSbI_6$  systems, the I atom contribution in the density of states is higher than other atoms.

The influence of varying pressures on electronic properties has been extensively analyzed using the mBJ potential. Understanding how pressure affects electronic properties is crucial as it provides insights into surface characteristics. This analysis involved studying the impact of pressure by decreasing the lattice parameter from its equilibrium value.

We performed band gap calculations under different pressures to examine how our compound responds to these changes. The variation of the band gap under different pressures is shown in Table 4.1. We have investigated the changes in the DOS for  $K_2AgSbI_6$  double perovskite under hydrostatic pressures. Figure 4.8 shows the

## Results and Discussion



**Figure 4.7:** (a) Total density of states of  $\text{K}_2\text{AgSbI}_6$ , (b) Partial density of states of K, (c) Partial density of states of Ag, (d) Partial density of states of Sb and (e) Partial density of states of I at ambient pressure.

computed total and partial density of states of  $\text{K}_2\text{AgSbI}_6$  double perovskite materials under various pressures. It has been observed that the DOS at the Fermi level changes as the pressure changes. We can relate this to the band gap, as the band gap changes with pressure. Consequently, the energy distance between the valence band (VB) and conduction band (CB) from the Fermi level also changes. Similar to its behavior at 0 GPa, the  $\text{K}_2\text{AgSbI}_6$  system demonstrates p-type semiconducting nature at all applied pressures. The uppermost valence electronic states in the range of -2 to -4 eV change to 1 to 3 eV in the conduction band, showing a significant pressure influence on TDOS for this system.

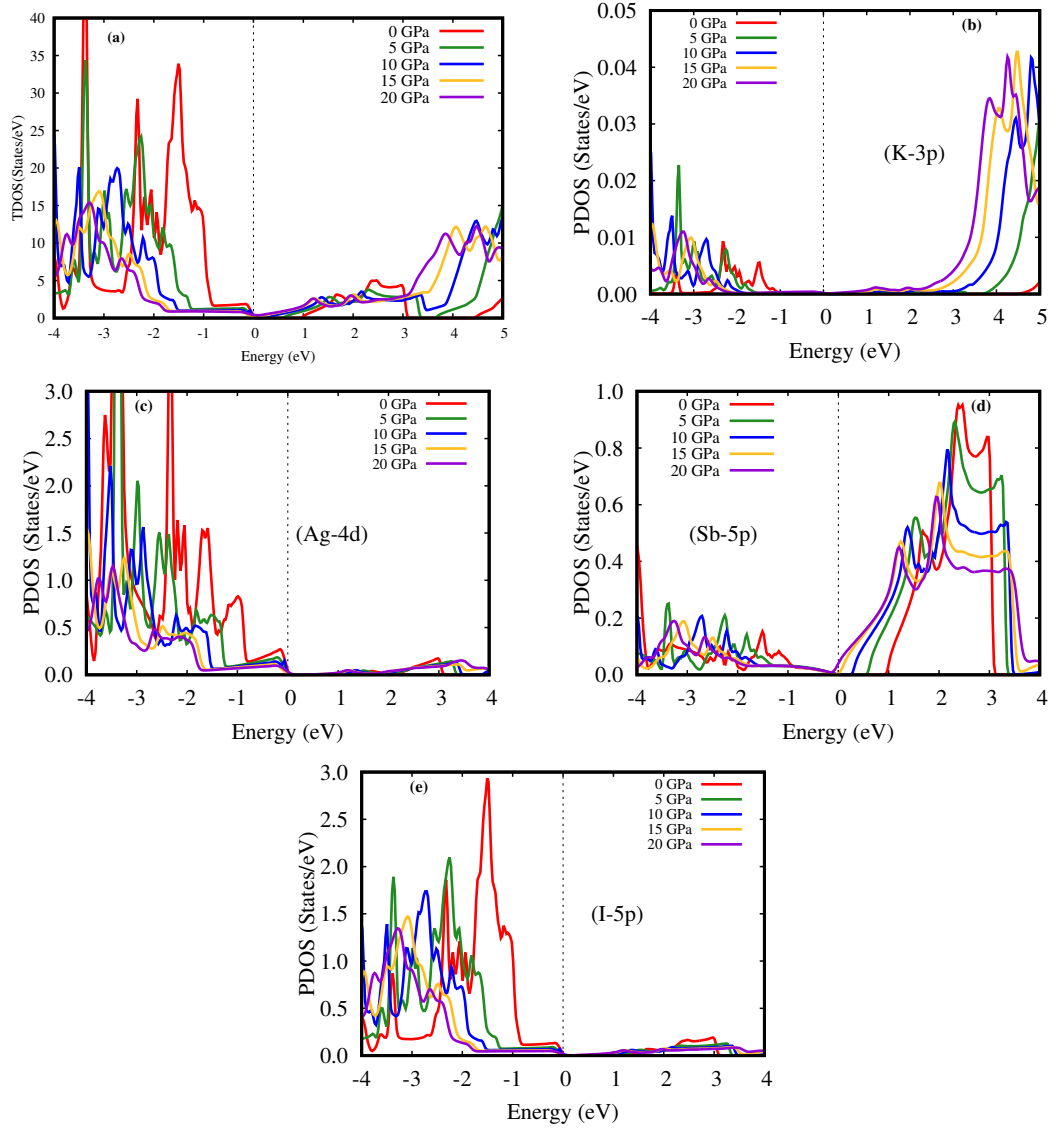


**Figure 4.8:** (a) Total density of states of  $\text{K}_2\text{AgSbI}_6$ , (b) Partial density of states of K, (c) Partial density of states of Ag, (d) Partial density of states of Sb and (e) Partial density of states of I under different hydrostatic pressure.

Only the valence electrons participate in inter-band transitions and hybridization. It is evident from the partial density plot of K, Ag, Sb and I that the valence band for all pressure near the fermi level mostly originated by I-5p states with a small contribution of Ag-4d states. Whereas the conduction band minimum is mainly originated by I-5p and Sb-5p states. All sharp peaks subjected to pressure progressively move downward. This peak shifting results in a reduction of the band gap under pressure. Similarly, we have calculated the density of states (DOS) for another system,  $\text{K}_2\text{AgBiI}_6$ , at ambient pressure and under hydrostatic pressure.

## Results and Discussion

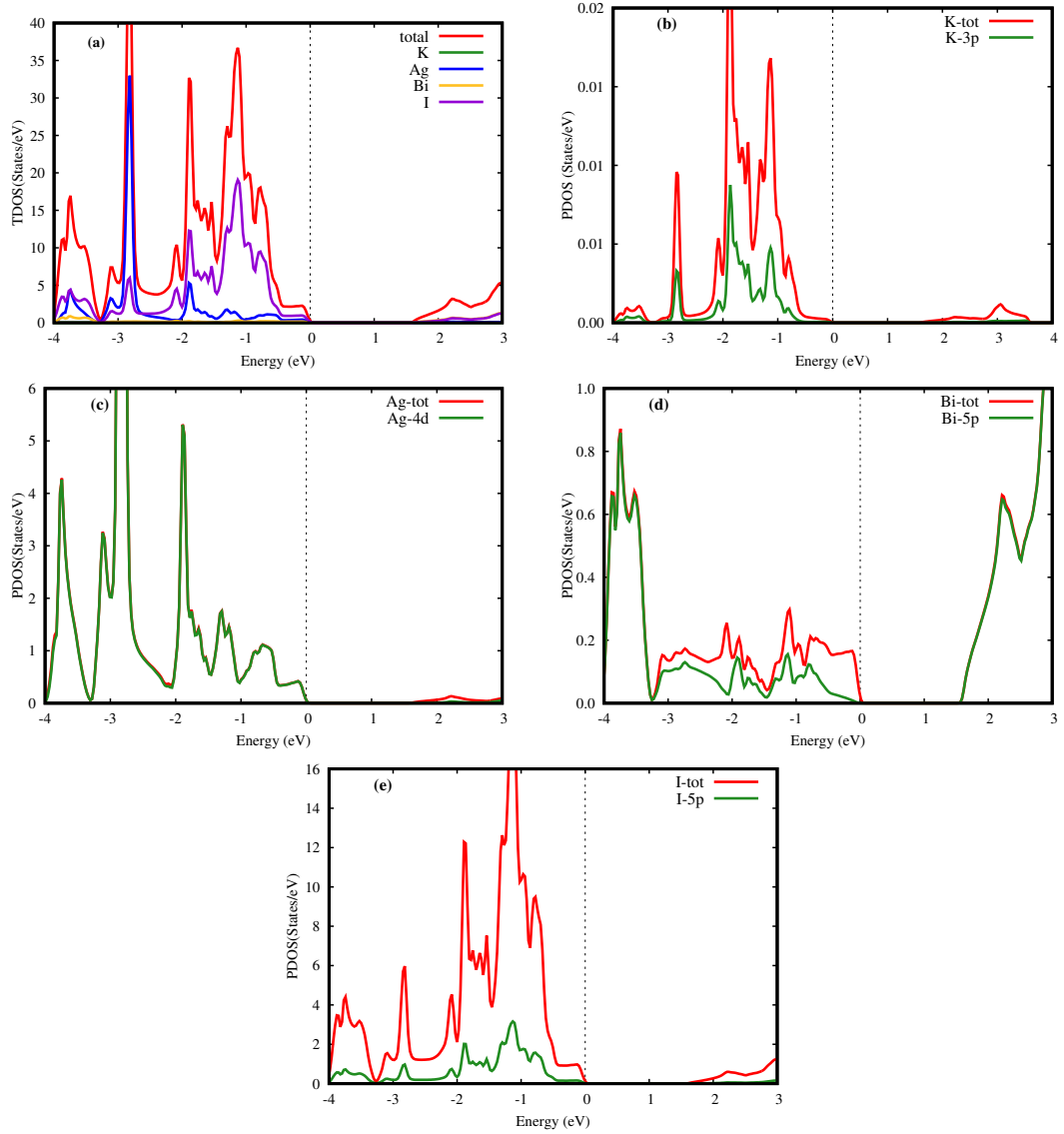


**Figure 4.9:** (a) Total density of states of  $\text{K}_2\text{AgBiI}_6$ , (b) Partial density of states of K, (c) Partial density of states of Ag, (d) Partial density of states of Bi and (e) Partial density of states of I at ambient pressure.

Figure 4.9 shows the computed total and partial density of states of the  $\text{K}_2\text{AgBiI}_6$  double perovskite material at ambient pressure. From the total DOS in Figure 4.9, the valence band near the Fermi level is mostly originated from I-5p states with a small contribution from Ag-4d states. In contrast, the conduction band minimum is mainly originated from I-5p states and Bi-5p states. Thus, at ambient pressure for the system  $\text{K}_2\text{AgBiI}_6$ , the I-5p states dominate over other atoms in both the valence and conduction bands. We have investigated the changes in the DOS for  $\text{K}_2\text{AgBiI}_6$  double perovskite under hydrostatic pressures. The variation of the band gap for  $\text{K}_2\text{AgBiI}_6$  under different pressures is shown in Table 4.2. Figure 4.10 shows

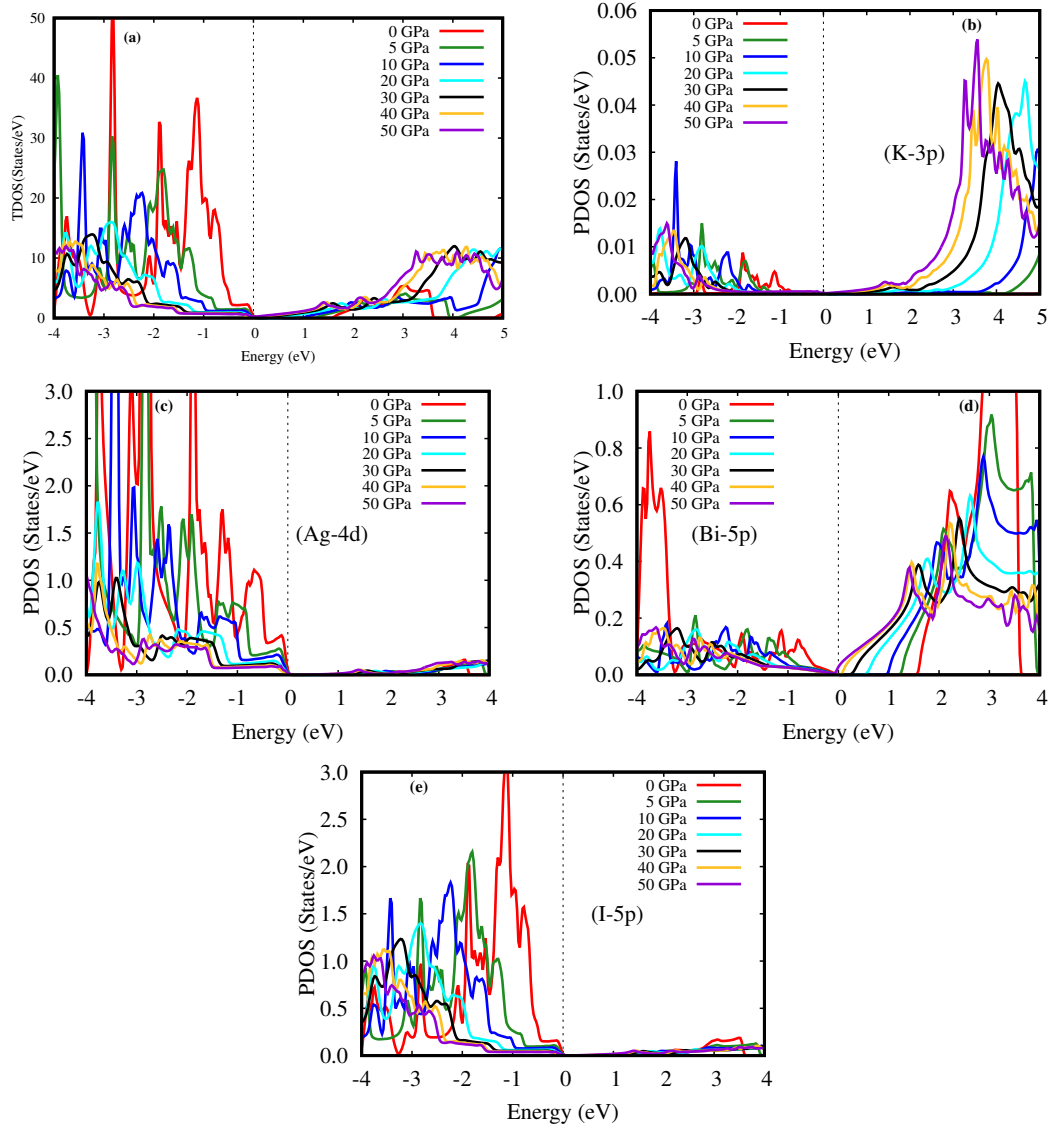


**Figure 4.10:** (a) Total density of states of  $\text{K}_2\text{AgBiI}_6$ , (b) Partial density of states of K, (c) Partial density of states of Ag, (d) Partial density of states of Bi and (e) Partial density of states of I under hydrostatic pressure.

the computed total and partial density of states of  $\text{K}_2\text{AgBiI}_6$  double perovskite materials under various pressures. It has been observed that the DOS at the Fermi level changes as the pressure changes. The uppermost valence electronic states in the range of -2 to -4 eV change to 1 to 3 eV in the conduction band, showing a significant pressure influence on TDOS for this system. From the partial density plot of K, Ag, Bi and I that the valence band for all pressure near the fermi level mostly originated by I-5p states with a small contribution of Ag-4d states. Whereas the conduction band minimum is mainly originated by I-5p and Bi-5p states.

## Results and Discussion

---

In summery, the physical properties of a compound are determined solely by the states that make up the valence band maxima and conduction band minima. Thus, it can be concluded that in our computed  $K_2AgXI_6$  ( $X = Sb, Bi$ ) systems, the potential indirect transition occurs from I-5p in the valence band to the conduction band. Consequently, the p-p hybridizations are responsible for excitation and recombination in our system.

### 4.4 Optical properties

The optical properties of the studied double perovskites (DPs) illustrate their behavior against light energy, highlighting their importance for solar cell applications. The optical characteristics of the considered  $K_2AgXI_6$  ( $X = Sb, Bi$ ) include the dielectric function, absorption coefficient, optical conductivity, reflectivity, and refractive index. These optical characteristics are crucial for their potential use in infrared (IR), electronic, and optical applications. The interaction between the incident electromagnetic frequency and the bound lattice constant ( $a_0$ ) electrons in the valence band affects the optical response. This type of recombination is used to evaluate the material's potential for optoelectronic applications, as the bound electrons absorb the incident energy and transition to the conduction band [100].

The impact of pressure on the optical properties of a material can lead to changes in electronic transitions, alterations in lattice vibrations affecting phonon modes, variations in density influencing the refractive index, and potential phase transitions. To understand the nature of light-matter interactions in these systems for practical applications, the optical properties of  $K_2AgXI_6$  ( $X = Sb, Bi$ ) under induced pressure have been calculated. In this study, the optical properties (real and imaginary parts of the dielectric function, absorption coefficient, optical conductivity, reflectivity, and refractive index) of  $K_2AgXI_6$  ( $X = Sb, Bi$ ) are analyzed and discussed under hydrostatic pressure.

#### 4.4.1 Dielectric function

We have calculated the real and imaginary imaginary dielectric function by the help of Kramer-Kronig relation [101]. The dielectric function is dependent on frequency of electron gas and can be written as  $\epsilon(\omega)$ . The complex dielectric function written as:

$$\epsilon(\omega) = \epsilon_1(\omega) + i\epsilon_2(\omega). \quad (4.3)$$

Where,  $\epsilon_1(\omega)$  and  $\epsilon_2(\omega)$  are represents real and imaginary parts of the dielectric function. The real part describes the ability of the material to store energy in an electromagnetic field, while the imaginary part describes the loss of energy due to absorption or scattering by the material. The formula for calculating  $\epsilon_2(\omega)$  with cubic symmetry substance [102]:

$$\epsilon(\omega) = \frac{8}{2\pi\omega^2} \sum_{nn'} \int_{BZ} |P_{nn'}(k)|^2 \frac{dS_k}{\nabla\omega_{nn'}(k)} \quad (4.4)$$

And  $\epsilon_1(\omega)$  can be found using Kramers–Kronig relation which is [103]:

$$\epsilon(\omega) = 1 + \frac{2}{\pi} P \int_0^\infty \frac{\omega' \epsilon_2(\omega')}{\omega'^2 - \omega^2} d\omega' \quad (4.5)$$

In equation 4.5,  $\omega_{nn'}$  is the energy difference between the two states,  $dS_k$  is an energy surface with constant value, and  $P_{nn'}$  is the dipole matrix element between the initial and final states. In 4.5,  $P$  denotes the principal part of the integral. The dielectric function is a useful tool for calculating various optical properties, as we will explore in the following sections.

The Figure 4.11 shows the variation of the real dielectric function  $\epsilon_1(\omega)$  with energy at ambient conditions and under hydrostatic pressure for  $K_2AgSbI_6$  ( $X = Sb, Bi$ ) systems. In the case of  $K_2AgSbI_6$ , the static dielectric constant  $\epsilon_1(0)$  is 5.8 and increases with the energy of the incident electromagnetic wave. From the graph, it is evident that  $\epsilon_1(\omega)$  first increases with energy, reaches a peak value, and then decreases. The negative  $\epsilon_1(\omega)$  indicates that the typical semiconductor behavior changes to metallic

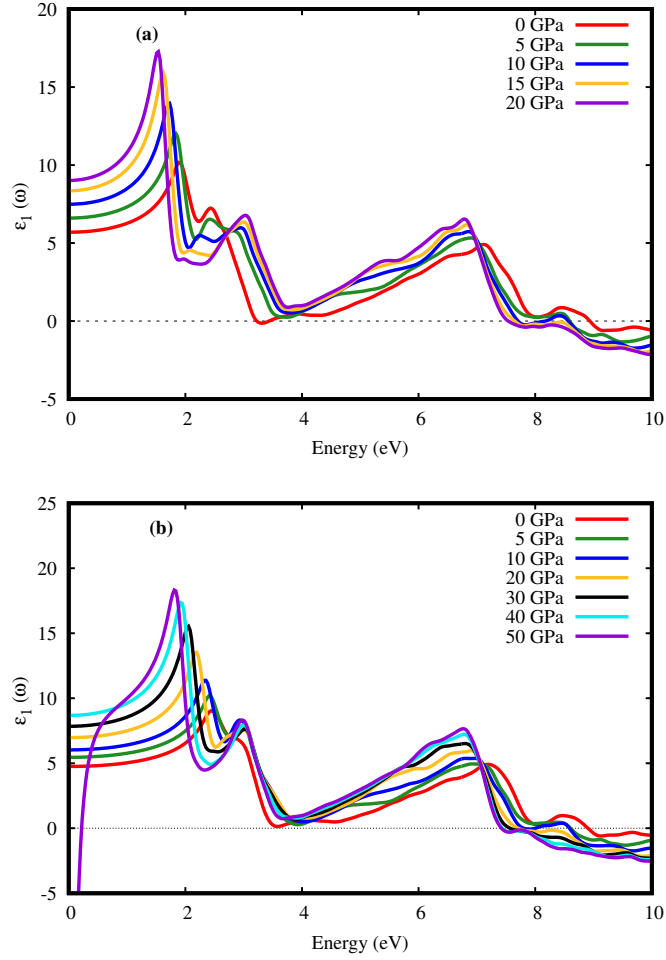


**Figure 4.11:** The computed optical (a) Real dielectric function of  $\text{K}_2\text{AgSbI}_6$  and (b) Real dielectric function of  $\text{K}_2\text{AgBiI}_6$  at ambient and under hydrostatic pressure pressure.

behavior in the studied halide double perovskite. For the  $\text{K}_2\text{AgSbI}_6$  system, at 0 GPa, the static part of  $\epsilon_1(\omega)$ , expressed as  $\epsilon_1(0)$ , is 5.8. It increases with energy and reaches a maximum around 2 eV. Similarly, for the  $\text{K}_2\text{AgBiI}_6$  system, at 0 GPa, the static part of  $\epsilon_1(\omega)$ , expressed as  $\epsilon_1(0)$ , is 4.9. It increases with energy and reaches a maximum around 2.79 eV. Interestingly, the decreasing band gap due to applied pressure shifts this maximum to higher energy for both systems, as shown in Figure 4.11. This illustrates the tunable transparency for visible radiation, suggesting potential optical applications.

The variation of the imaginary dielectric function  $\epsilon_2(\omega)$  plotted against the energy range of 0-10 eV is shown in Figure 4.12 at ambient conditions and under induced pressure. For both systems  $\text{K}_2\text{AgXI}_6$  ( $X = \text{Sb}, \text{Bi}$ ),  $\epsilon_2(\omega)$  shows light absorption

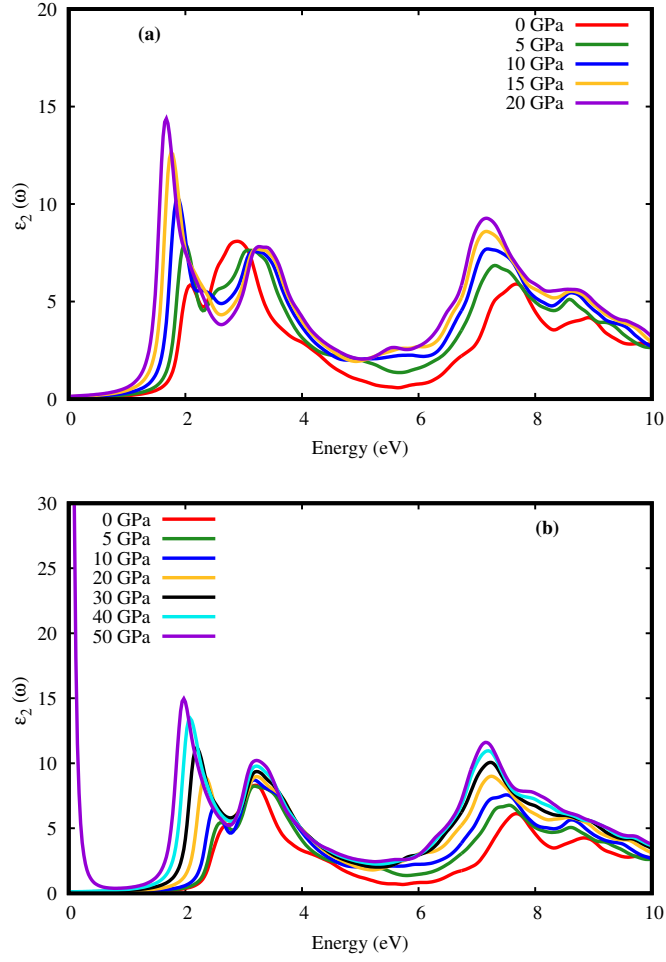


**Figure 4.12:** The computed optical (a) Imaginary dielectric function of  $\text{K}_2\text{AgSbI}_6$  and (b) Real dielectric function of  $\text{K}_2\text{AgBiI}_6$  at ambient and under hydrostatic pressure.

when light of a suitable frequency falls on it. The threshold values for light absorption are proportional to the optical band gaps, and after these threshold energies, light absorption starts. These threshold values are 1.8 eV as calculated from  $\epsilon_2(\omega)$  for  $\text{K}_2\text{AgSbI}_6$  and 2.2 eV for  $\text{K}_2\text{AgBiI}_6$ .

The imaginary dielectric constant  $\epsilon_2(\omega)$  exhibits positive values for all energies, and overall higher energy shifts occur with increasing external pressure. In Figure 4.12,  $\epsilon_2(\omega)$  shows maximum values in the visible region for both systems with increasing pressure. Therefore,  $\text{K}_2\text{AgXI}_6$  ( $X = \text{Sb}, \text{Bi}$ ) is suitable for solar cell applications.

### 4.4.2 Absorption coefficient

The "absorption coefficient" is defined as the percentage of radiation absorption per unit distance through a material to the amount of radiation that hits the medium. It measures the extent to which a substance absorbs electromagnetic radiation, including light. The absorption coefficient depends on a number of things, like material's composition, structure, thickness, along with frequency or wavelength of the radiation that hits it. In general, materials with closely bound electrons or greater thickness will absorb radiation more efficiently than those with less tightly bound electrons or more dispersed electrons. The absorption coefficient can be represented by the dielectric constant using the equation [104]:

$$\alpha(\omega) = \frac{\sqrt{2}\omega}{c} [(\epsilon_1(\omega)^2 + \epsilon_2(\omega)^2)^{\frac{1}{2}} - \epsilon_1(\omega)]^{\frac{1}{2}} \quad (4.6)$$

The absorption coefficient  $\alpha(\omega)$  is a significant physical property that defines a material's ability to absorb and reduce the intensity of electromagnetic radiation. When a substance is illuminated, both transmission and surface reflection are observable. The decrease in light intensity as it travels through the medium indicates the absorption coefficients. The absorption coefficient  $\alpha(\omega)$  quantifies the light energy absorbed by the semiconductor. It is crucial to note the sharp absorption edges when the incident energy surpasses the bandgap, as these edges are essential for determining the bandgap. Both  $\alpha(\omega)$  and  $\epsilon_2(\omega)$  represent the absorption of light. In Figure 4.13, we can see the variation of the absorption coefficient with energy for  $\text{K}_2\text{AgXI}_6$  ( $X = \text{Sb}, \text{Bi}$ ) double perovskite materials at ambient and under induced pressure. The range of photon energies for visible light is 1.65 eV to 3.26 eV. As the incident energy increases, the absorption coefficient increases in the visible region, with much larger absorption coefficients observed in the ultraviolet (UV) region. When pressure increases in the early UV region, the absorption coefficient decreases, but after 6 eV, it increases as the photon energy continues to rise for both systems. For both systems, the absorption significantly increases in the 8-10 eV region compared to 0 GPa. Our compounds show that the absorption coefficient increases under applied hydrostatic pressure, indicating that both systems can

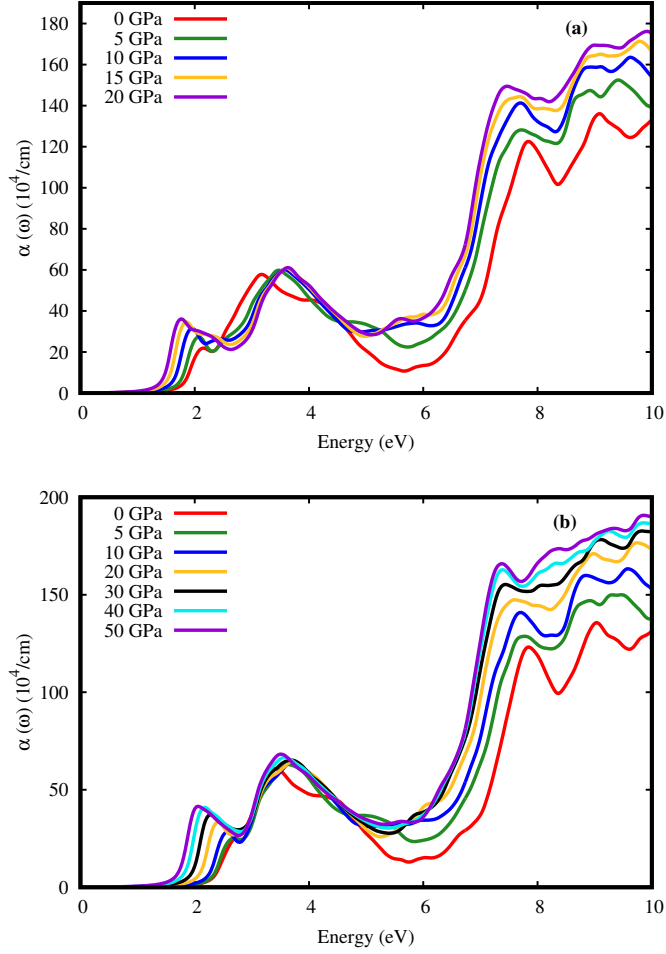


**Figure 4.13:** The computed optical (a) Absorption coefficient of  $\text{K}_2\text{AgSbI}_6$  and (b) Absorption coefficient of  $\text{K}_2\text{AgBiI}_6$  at ambient and under hydrostatic pressure.

be potential absorbers in the ultraviolet region. The diagrams of the absorption coefficient under various pressures can be seen in Figure 4.13.

### 4.4.3 Optical conductivity

Optical conductivity is a property of a material that describes the relationship between the magnitudes of the inducing electric fields and the induced current density of the material. It provides information about the material's atomic-level electronic structure and behavior. Figure 4.14 depicts the optical conductivity of our compounds  $\text{K}_2\text{AgXI}_6$  ( $X = \text{Sb}, \text{Bi}$ ) at ambient conditions and under pressure. This figure indicates the degree to which a material conducts electricity when subjected to an applied electric field. The image illustrates how our compound's conductivity

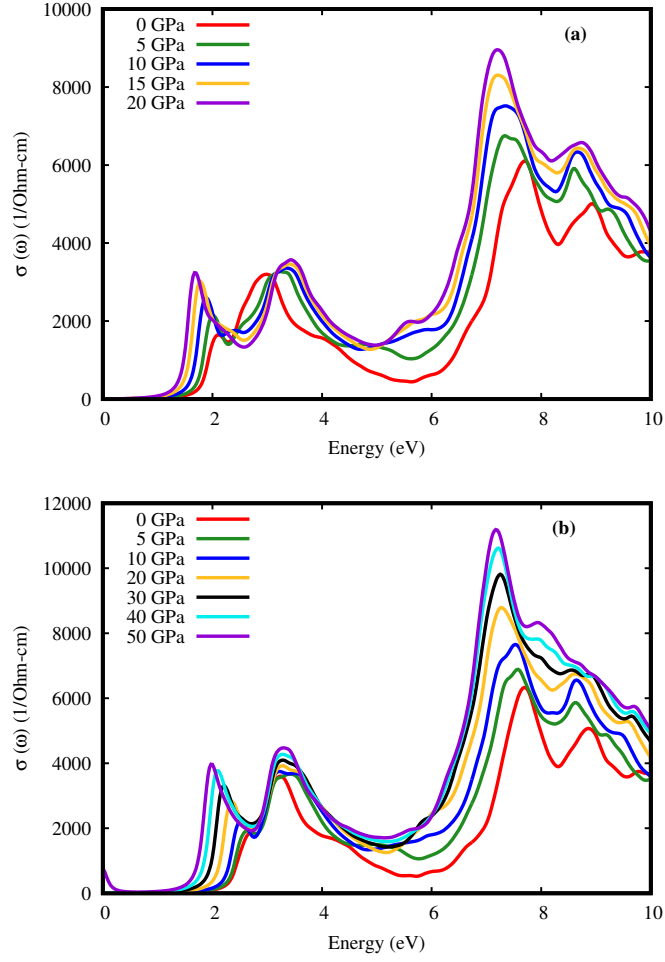


**Figure 4.14:** The computed optical (a) Conductivity of  $\text{K}_2\text{AgSbI}_6$  and (b) Conductivity of  $\text{K}_2\text{AgBiI}_6$  at ambient and under hydrostatic pressure.

increases as it crosses the x-axis band gap energy. This is necessary for our compound to excite its electrons from the valence band (VB) to the conduction band (CB) to this degree of energy. As a result, the CB in the material gains free electrons, enabling electrical conductivity. The behavior of optical conductivity and absorption coefficient plots are similar because the attenuation of incident light increases electron concentration in the conduction band. The peaks of optical conductivity become sharper with the application of hydrostatic pressure in the UV region at 7 eV for  $\text{K}_2\text{AgSbI}_6$  and 7.2 eV for  $\text{K}_2\text{AgBiI}_6$ . Therefore, the optical conductivity increases with increasing pressure for both systems compared to ambient pressure. The conductivity begins to decline after reaching an energy of 10 eV for both systems.

#### 4.4.4 Optical reflectivity

Optical reflectivity  $R(\omega)$  is the fraction of incident light that is reflected off the surface of a material. It can be defined as the ratio of the intensity of incident radiation to the intensity of reflected radiation. The optical reflectivity can be directly represented by the dielectric constant, as stated in reference [104]:

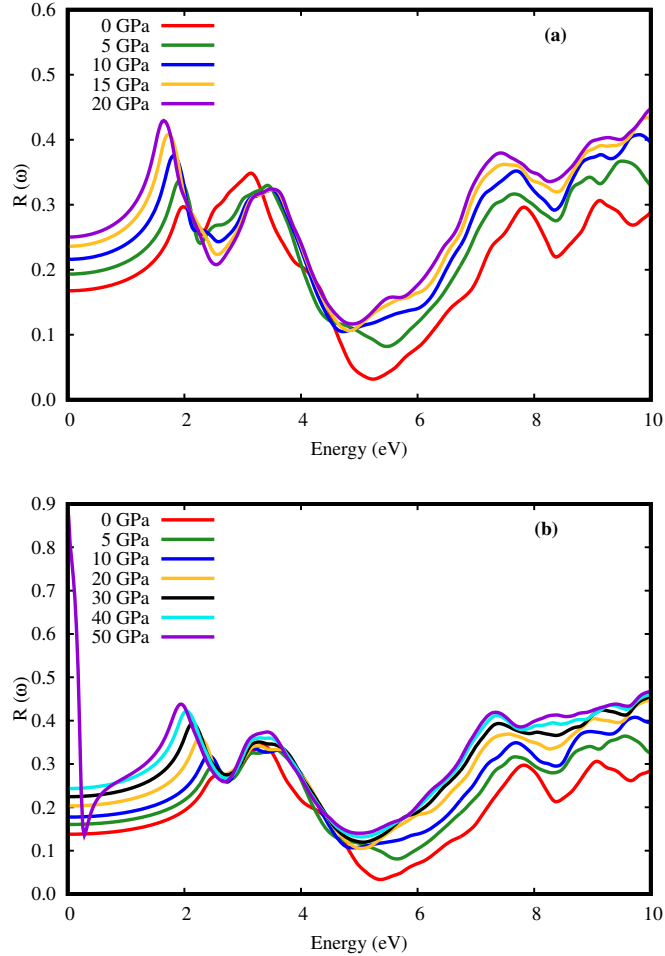


**Figure 4.15:** The computed optical (a) Reflectivity of  $K_2AgSbI_6$  and (b) Reflectivity of  $K_2AgBiI_6$  at ambient pressure and under hydrostatic pressure.

$$R(\omega) = \frac{-i\omega(\epsilon_2(\omega) - 1)}{4\pi} \quad (4.7)$$

The optical reflectivity is influenced by various factors such as the material's composition, structure, and surface properties. Additionally, the wavelength and angle of the incident radiation also play significant roles. Optical reflectivity finds ap-

## Results and Discussion

---

plications in various fields like mirrors, photovoltaics, sensing, and nano-photonics. A material's ability to reflect light is measured by its optical reflectivity. Figure 4.15 shows how our material's optical reflectivity for  $\text{K}_2\text{AgXI}_6$  ( $X = \text{Sb}, \text{Bi}$ ) varies with different energies at ambient pressure and under applied pressure. At ambient pressure, reflectivity starts increasing after a threshold and peaks at the boundary of the visible region, making a sharp peak at 3.3 eV for  $\text{K}_2\text{AgSbI}_6$  and at 3.5 eV for  $\text{K}_2\text{AgBiI}_6$ . At ambient pressure, the reflectivity is less than 30 percent of the incident electromagnetic wave for both systems. Under applied pressure, reflectivity increases to about 43 percent for both systems. In the visible region, the maximum reflectivity is greater than 30 percent for both systems under all applied pressures. Therefore, a large value of  $R(\omega)$  compared to 0 GPa pressure influences the performance of any optical device.

### 4.4.5 Refractive index

The refractive index is defined as the ratio of the speed of light at a specific substance to its speed in vacuum, and it is used to characterize the degree to which light is slowed down as it passes through a material. The relationship between the refractive index  $n(\omega)$  as a function of frequency and the dielectric constant can be expressed through equation as stated in reference [104]:

$$n(\omega) = \frac{\sqrt{[\epsilon_1^2 + \epsilon_2^2]^{\frac{1}{2}} + \epsilon_1(\omega)^2}}{\sqrt{2}} \quad (4.8)$$

The refractive index controls both the amount of light bending (or refraction) that occurs when light travels through a material and the angle at which light is reflected at its outermost layer. A refractive index diagram of  $\text{K}_2\text{AgXI}_6$  ( $X = \text{Sb}, \text{Bi}$ ) double perovskites at ambient pressure and under hydrostatic pressure is presented in Figure 4.16, along with a graph illustrating the relationship between photon energy and refractive index. The change of  $n(\omega)$  with respect to energy is similar to  $\epsilon_1(\omega)$ , and both express the same information about the material. The relation between the static values of the real dielectric constant and the refractive index,  $n(0) = \epsilon_1(0)^{1/2}$ ,

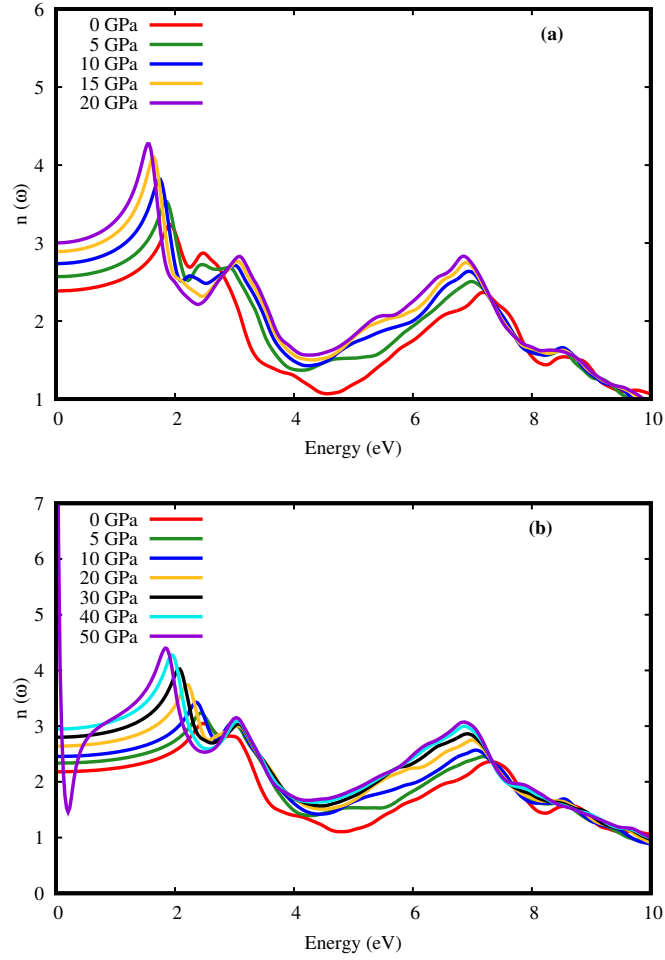


**Figure 4.16:** The computed optical (a) Refraction of  $K_2AgSbI_6$  and (b) Refraction of  $K_2AgBiI_6$  at ambient and under hydrostatic pressure.

is satisfied, as evidenced by the static real dielectric constant. From the figure, in the case of  $K_2AgSbI_6$ , under all applied pressures compared to 0 GPa,  $n(\omega)$  increases when light energy enters the visible region and becomes maximum at 20 GPa. Similarly, in the case of  $K_2AgBiI_6$ ,  $n(\omega)$  increases in the visible region and becomes maximum at 50 GPa. Therefore, there is a significant influence of applied pressure on the refractive index compared to 0 GPa.

In summary, all the calculated optical properties under applied pressure compared to ambient conditions indicate the improved optical usability of  $K_2AgXI_6$  ( $X = Sb, Bi$ ) as an optoelectronic device. But between the two systems,  $K_2AgBiI_6$  is more suitable than  $K_2AgSbI_6$  based on the dielectric function, optical absorption, optical conductivity, reflectivity, and refractive index.

## 4.5 Thermoelectric properties

The potential difference produced by a heat gradient during energy transfer can be utilized in thermoelectric materials for converting thermal energy into electrical energy. Temperature gradients are caused by the movement of charges for energy transfer, resulting in a potential difference and a thermoelectric effect. Thermoelectric compounds have been studied for converting heat power into electricity for use in computer cooling, tiny sensor devices, and thermoelectric refrigerators over the past few years.

Different parameters of transport properties are shown in graphs for  $K_2AgXI_6$  ( $X = Sb, Bi$ ) compounds. A higher Seebeck coefficient, higher electrical conductivity, and higher thermal conductivity result in fascinating thermoelectric performance. The thermoelectric properties of lead-free halide  $K_2AgXI_6$  ( $X = Sb, Bi$ ) double perovskites at ambient pressure and under hydrostatic pressure were calculated using the BoltzTrap package. We determined the transport coefficients such as the Seebeck coefficient ( $S$ ), electrical conductivity ( $\sigma/\tau$ ), thermal conductivity ( $\kappa_e/\tau$ ), power factor ( $S^2\sigma/\tau$ ), and dimensionless figure of merit ( $ZT$ ) as a function of temperature, combined in a compressed form as [105].

$$ZT = \frac{S^2\sigma T}{\kappa}. \quad (4.9)$$

### 4.5.1 Seebeck coefficient

The Seebeck coefficient measure the magnitude of induced change in voltage by applying the change in temperature, which can be seen in the mathematical form,

$$S = \frac{\mu \nabla V}{\nabla T} \quad (4.10)$$

We accomplished the Seebeck coefficient ( $S$ ) against temperature as demonstrated in Figure 4.17 for halide double perovskites  $K_2AgXI_6$  ( $X = Sb, Bi$ ). At 300 K temperature  $S$  found maximum about  $264 \mu V/K$  for  $K_2AgSbI_6$  compound and about

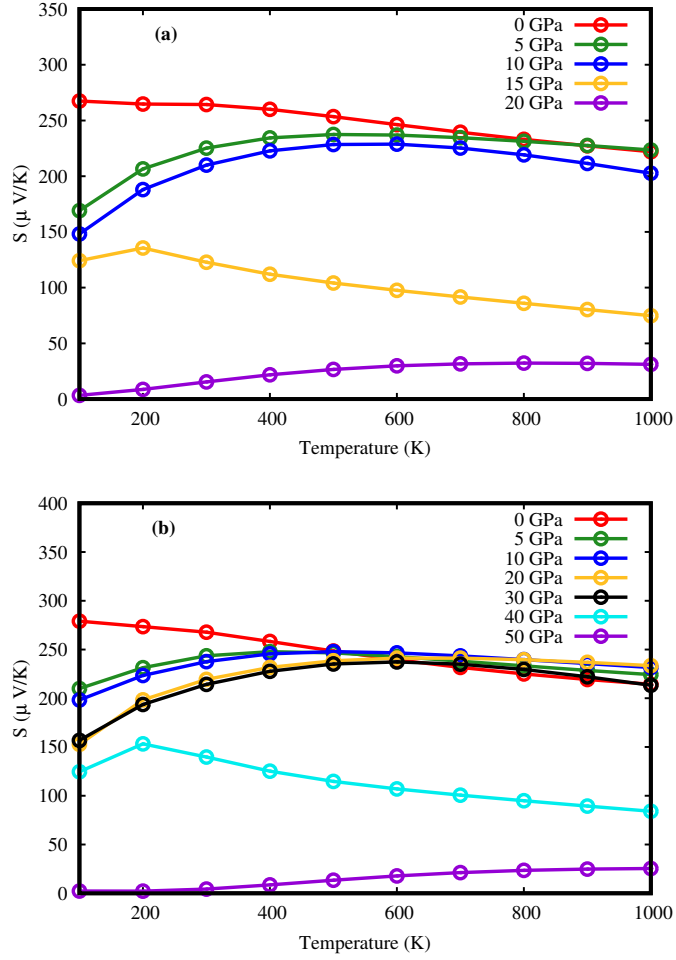


**Figure 4.17:** Calculated thermal properties to observe the (a) Seebeck coefficient of  $\text{K}_2\text{AgSbI}_6$  and (b) Seebeck coefficient of  $\text{K}_2\text{AgSbI}_6$  at ambient and under hydrostatic pressure

268  $\mu\text{V}/\text{K}$  for  $\text{K}_2\text{AgBiI}_6$  compound while with increasing temperature  $S$  linearly decreased, observed 214  $\mu\text{V}/\text{K}$  and 222  $\mu\text{V}/\text{K}$  for  $\text{K}_2\text{AgSbI}_6$  and  $\text{K}_2\text{AgBiI}_6$  compounds at 1000 K temperature as shown in the figure. We investigated the Seebeck coefficient against temperature for  $\text{K}_2\text{AgXI}_6$  ( $X = \text{Sb}, \text{Bi}$ ) double perovskites under different pressures, up to 20 GPa for the  $\text{K}_2\text{AgSbI}_6$  system and up to 50 GPa for the  $\text{K}_2\text{AgBiI}_6$  system, as shown in Figure 4.17. From the figure, we see that the Seebeck coefficient decreases with rising temperature and also decreases under pressure. Excellent thermoelectric materials are indicated by  $S \geq 200 \mu\text{V}/\text{K}$  [106]. At room temperature, our computations at ambient pressure yield 264  $\mu\text{V}/\text{K}$  for the  $\text{K}_2\text{AgSbI}_6$  system and 268  $\mu\text{V}/\text{K}$  for the  $\text{K}_2\text{AgBiI}_6$  system, which are highly exceptional compared to the quoted number. Under all applied pressures, the value

## Results and Discussion

of  $S$  gradually decreases compared to 0 GPa for both systems. Thus, the studied double perovskite materials at ambient pressure are excellent for thermoelectric applications and among the two systems  $K_2AgBiI_6$  is more suitable for thermoelectric applications than  $K_2AgSbI_6$ .

### 4.5.2 Electrical conductivity

Conduction in materials is induced by the free motion of carriers from one point to another. In semiconductor materials, there are two key factors for conductivity: carrier concentrations and carrier mobilities. These can be expressed mathematically

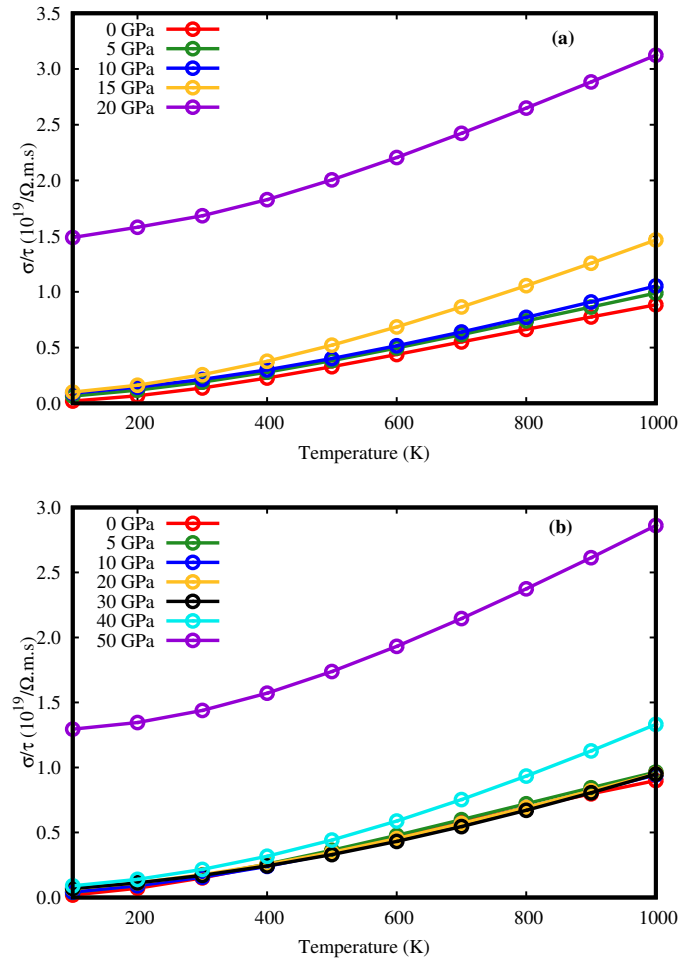


**Figure 4.18:** Calculated thermal properties to observe the (a) Electrical conductivity of  $K_2AgSbI_6$  and (b) Electrical conductivity of  $K_2AgBiI_6$  at ambient and under induced pressure

## Results and Discussion

---

as  $\sigma = n_e\mu_e + n_h\mu_h$ . The electrical conductivity of a material quantifies the flow of charge through it. We computed the electrical conductivity per relaxation time ( $\sigma/\tau$ ) against temperatures ranging from 100 K to 1000 K, as shown in Figure 4.18 for  $\text{K}_2\text{AgXI}_6$  ( $X = \text{Sb}, \text{Bi}$ ) double perovskite materials. From the figure, we can see that the conductivity of the compounds increases linearly with temperature, indicating an increase in carrier concentration associated with electrical conduction. The investigated compounds' semiconductor nature is supported by the increase in electrical conductivity, which represents a continually growing carrier concentration and implies a negative temperature coefficient of resistance. We also computed the electrical conductivity per relaxation time ( $\sigma/\tau$ ) against temperature, as shown in Figure 4.18, for  $\text{K}_2\text{AgXI}_6$  ( $X = \text{Sb}, \text{Bi}$ ) double perovskite materials under hydrostatic pressure. From the figure, we see that under induced pressure, the value of  $\sigma/\tau$  increases continuously with temperature. At 20 GPa for the  $\text{K}_2\text{AgSbI}_6$  system and at 50 GPa for the  $\text{K}_2\text{AgBiI}_6$  system, the value of  $\sigma/\tau$  becomes maximum, which means that with increasing pressure, more and more electrons get excited, contributing to an increase in carrier concentration.

### 4.5.3 Thermal conductivity

Thermal conductivity explains the transportation through a material as the materials atom are constantly moving in rotational, translational or vibrational motion. The variation of atoms is responsible for generating heat or thermal energy in a material. We investigated thermal conductivity ( $\kappa_e/\tau$ ) for  $\text{K}_2\text{AgXI}_6$  ( $X = \text{Sb}, \text{Bi}$ ) compounds as shown in Figure 4.19. From figure we can see, the conductivity of the compound increases linearly with temperature which is similar behavior as electrical conductivity.

We also computed the thermal conductivity per relaxation time ( $\kappa_e/\tau$ ) against temperature as shown in Figure 4.19 for potassium based  $\text{K}_2\text{AgXI}_6$  ( $X = \text{Sb}, \text{Bi}$ ) double perovskites materials under hydrostatic pressure. We see from figure, under induced pressure, the value of  $\kappa_e/\tau$  increases continuously with temperature. At 20 GPa for  $\text{K}_2\text{AgSbI}_6$  system and at 50 GPa for  $\text{K}_2\text{AgBiI}_6$  system, the value of  $\kappa_e/\tau$

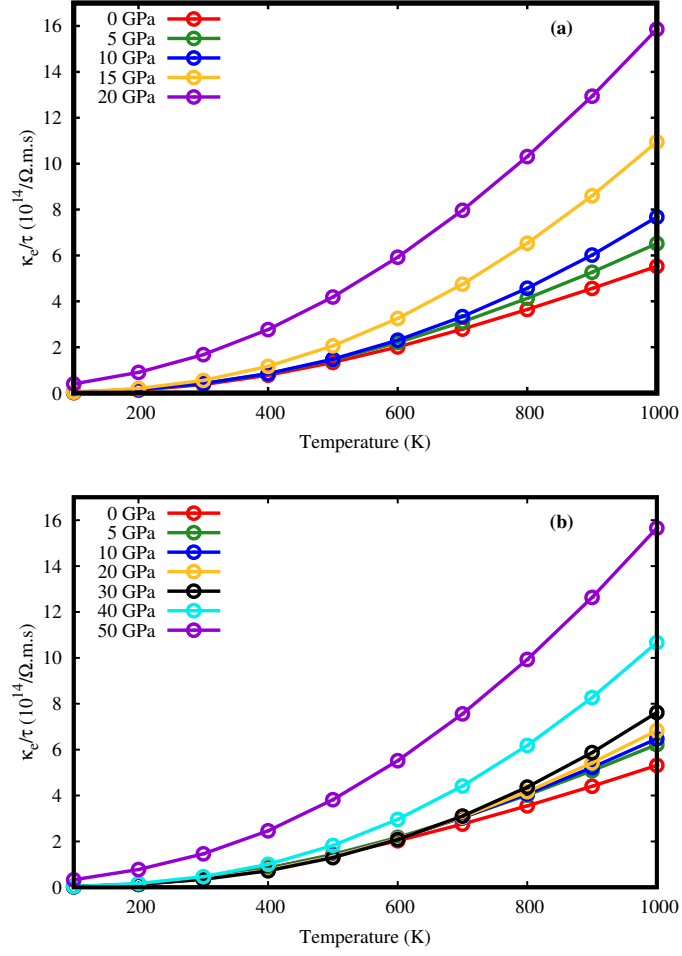


**Figure 4.19:** Calculated thermal properties to observe the (a) Thermal conductivity of  $K_2AgSbI_6$  and (b) Thermal conductivity of  $K_2AgBiI_6$  at ambient and under induced pressure

becomes maximum. Thus, better thermoelectric efficiency can only be achieved by a thermoelectric material with optimal thermal and electronic conductivities under hydrostatic pressure compared to ambient conditions.

#### 4.5.4 Power factor

The power factor ( $S^2\sigma/\tau$ ) of a material is a measure of how efficiently it can convert electric power into useful mechanical work or vice versa. Power factor of a material provides electrical energy. Figure 4.19 shows the power factor against temperature for  $K_2AgXI_6$  ( $X = Sb, Bi$ ) compounds and observed it at 300 K for both materials are approximately  $0.9 \times 10^{11}$  W/mK<sup>2</sup>s and  $1.1 \times 10^{11}$  W/mK<sup>2</sup>s respectively. The value of power factor increases continuously with temperature. At 1000 K temperature,

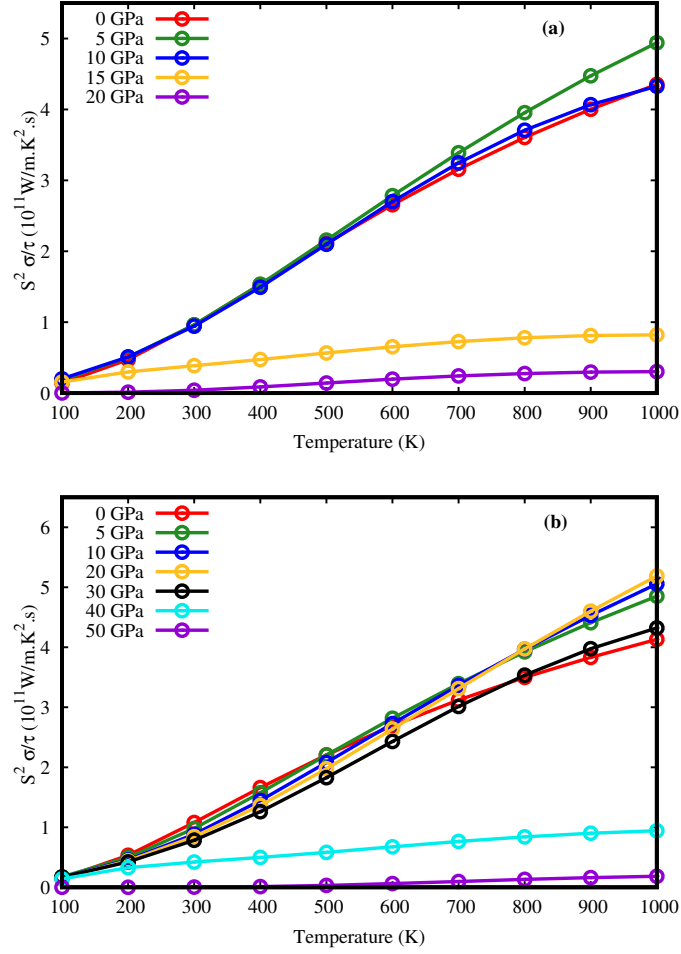


**Figure 4.20:** Calculated thermal properties to observe the (a) Power factor of  $\text{K}_2\text{AgSbI}_6$  and (b) Power factor of  $\text{K}_2\text{AgBiI}_6$  at ambient and under induced pressure

the value of power factor becomes maximum for both systems. We investigated power factor against temperature under hydrostatic pressure for both  $\text{K}_2\text{AgXI}_6$  ( $X = \text{Sb, Bi}$ ) compounds as shown in Figure 4.20. Without considering thermal conductivity, the power factor of a thermoelectric material can be used to explain its efficiency. At ambient pressure the power factor increases from  $0.9 \times 10^{11} \text{ W/mK}^2\text{s}$  to  $4.3 \times 10^{11} \text{ W/mK}^2\text{s}$  with temperature for  $\text{K}_2\text{AgSbI}_6$  compound and  $1.1 \times 10^{11} \text{ W/mK}^2\text{s}$  to  $4.1 \times 10^{11} \text{ W/mK}^2\text{s}$  for  $\text{K}_2\text{AgBiI}_6$  compound. After applying pressure, the power factor increases gradually for both systems.

### 4.5.5 Figure of merits

Dimensionless parameter which can measure the material quality for the thermal devices use is figure of merits. In last we computed the figure of merits (ZT) can be seen in Figure 4.21 for  $K_2AgXI_6$  ( $X = Sb, Bi$ ) compounds at ambient pressure. At temperature 300 K, ZT value examined approximately 0.776 and by increase temperature ZT increased til for  $K_2AgSbI_6$  about 0.79 at 500 K temperature. Then the ZT value decreases with increases temperature. Similary at temperature 300 K, ZT value examined approximately 0.791 and by increase temperature ZT increased til for  $K_2AgBiI_6$  about 0.797 at 500 K temperature. Then the ZT value decreases with increasing temperature. The figure of merit (ZT) is used to measure the quality of

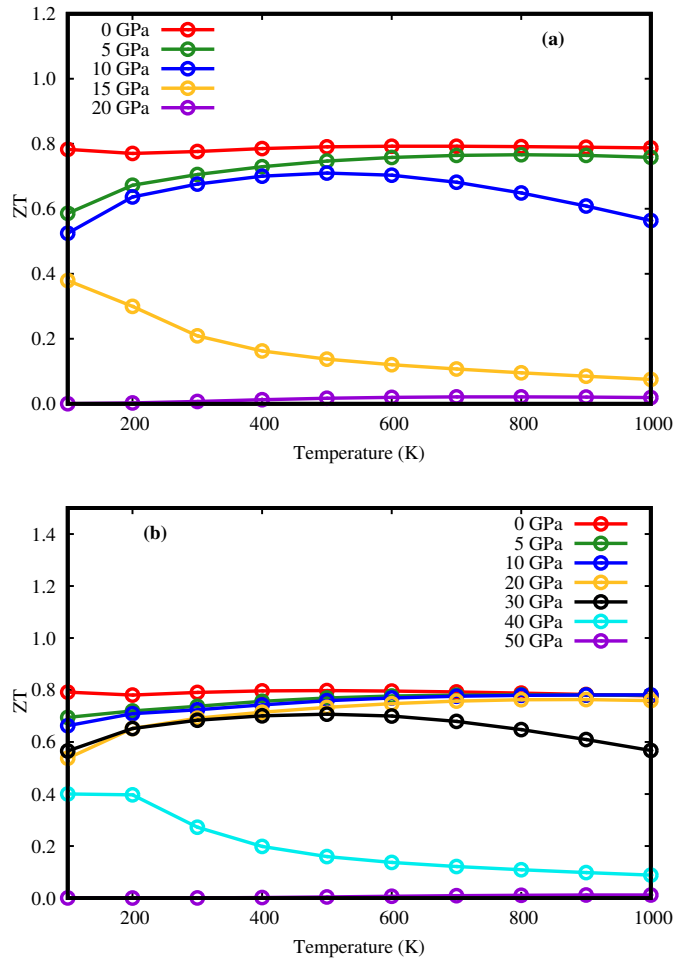


**Figure 4.21:** Calculated thermal properties to observe the (a) Figure of merits of  $K_2AgSbI_6$  and (b) Figure of merits of  $K_2AgBiI_6$  at ambient and under induced pressure

## Results and Discussion

---

materials for thermal devices. The ZT values of  $K_2AgXI_6$  ( $X = Sb, Bi$ ) compounds have been examined, as shown in Figure 4.21, under induced pressure. Under applied pressure, the ZT value gradually decreases for both systems compared to ambient conditions. In summary,  $K_2AgXI_6$  ( $X = Sb, Bi$ ) compounds exhibit enhanced electrical and thermal conductivity when exposed to pressure, owing to the presence of more free electrons in the conduction band. This results in improved thermoelectric performance, making it highly viable for devices.

### 4.6 Mechanical properties

The mechanical characteristics provides information about the possible industrial applications and about the micro cracks at the growing process. Mechanical characteristics show a material's capacity to return to its original shape in the event that distortion forces are removed. Since these characteristics are linked to the behaviors of materials, such as hardness, durability, strength, reliability, and performance necessary to identify the type of application and fabrication, the elastic constants of a material play a crucial role in determining how it responds to an applied stress. A system's need for an adequate number of elastic constants is directly correlated with its structural symmetry. The fewer elastic constants needed to investigate the mechanical behavior of the system, the more symmetrical the structure. In case of the cubic symmetry as in our case, only three elastic constants viz.  $C_{11}$ ,  $C_{12}$ , and  $C_{44}$  are required to define the various mechanical behavior of the materials. The calculated elastic parameters for  $K_2AgXI_6$  ( $X = Sb, Bi$ ) are reported in Table (4.3-4.6) respectively at ambient and under induced pressure.

Second order elastic constants ( $C_{ij}$ ), bulk modulus, Young's modulus, shear modulus, Poisson's ratio, anisotropy, brittleness, ductility, elastic wave propagation, and other solid state phenomena are examples of properties. For cubic crystals the required requirements for existing in stable or meta-stable phase is established in form stability condition [107],

$$C_{11} - C_{12} > 0, C_{11} > 0, C_{44} > 0, C_{11} + 2C_{12} > 0, C_{12} < B < C_{11}$$

## Results and Discussion

---

**Table 4.3:** Calculated the estimated elastic constant  $C_{11}$ ,  $C_{12}$ ,  $C_{44}$ , Cauchy's pressure of  $K_2AgSbI_6$  under hydrostatic pressure.

Pressures (GPa)	$C_{11}$	$C_{12}$	$C_{44}$	$C_{12} - C_{44}$
0	40.42	9.49	5.79	3.70
5	82.36	16.76	6.34	10.42
10	136.88	15.36	7.41	7.95
15	173.73	13.84	9.45	4.39
20	198.13	16.47	9.63	6.84

The compounds' mechanical stability under all pressures and ambient conditions is demonstrated by the positive values of the constants, which meet the established stability criterion. Using the computed elastic constants, various other mechanical parameters can be defined. The bulk and shear moduli that can forecast the hardness of material can be found using the Voigt-Reuss-Hill averaging scheme approach [108]. The Voigt limits of the bulk modulus ( $B$ ) and shear modulus ( $G$ ) for the cubic system are as follows:

$$B_v = \frac{(C_{11} + 2C_{12})}{3} \quad (4.11)$$

$$G_v = \frac{(C_{11} - C_{12} + 3C_{44})}{5} \quad (4.12)$$

However, the Reuss formulae for the bulk and shear moduli are:

$$B_v = B_R \quad (4.13)$$

$$G_R = \frac{5(C_{11} - C_{12} + C_{44})}{4C_{44} + 3(C_{11} - C_{12})} \quad (4.14)$$

Using Hill's average approximation the bulk and shear moduli are defined as;

$$B = \frac{B_v + B_R}{2} \quad (4.15)$$

## Results and Discussion

---

**Table 4.4:** The calculated the Bulk modulus  $B$  (GPa), the Shear modulus  $G$  (GPa), Young's modulus  $Y$  (GPa), the elastic anisotropy factor ( $A$ ),  $B/G$  ratio and Poisson's ratio ( $\nu$ ) of  $K_2AgSbI_6$  under hydrostatic pressure.

Pressures (GPa)	$B$	$G$	$Y$	$A$	$B/G$	$\nu$
0	19.80	8.69	22.71	0.374	2.27	0.308
5	38.63	13.14	35.14	0.193	2.94	0.347
10	55.86	20.09	53.82	0.121	2.78	0.339
15	67.14	26.13	69.38	0.118	2.57	0.327
20	77.02	28.55	76.24	0.106	2.69	0.335

$$G = \frac{G_v + G_R}{2} \quad (4.16)$$

Young's modulus, determines the strength of material is ratio of linear stress and strain can be evaluated via relation.

$$Y = \frac{9BG}{3B + G} \quad (4.17)$$

According to Pettifor [109], the Cauchy pressure ( $C_P = C_{12} - C_{44}$ ) might disclose the brittle or ductile nature of the atomic bond. For metallic bonding with ductile nature, the  $C_P$  is positive. Moreover, for brittle materials with directional and angular bonding character, it has negative value. Additionally, Pugh's ratio ( $B/G$ ) and Poisson's ratio ( $\nu$ ) [110] can be used to understand a compound's brittle and ductile nature. This is a crucial attribute for practical device fabrication. Properties such as brittleness, stiffness, and ductility are taken into account based on Poisson's and Pugh's ratios. The compound is thought to be ductile and suitable for device fabrication if its  $B/G$  and  $\nu$  higher than 1.75 and 0.26. However, a compound is considered to be plastic if its Poisson's ratio is smaller than 0.26 and indicates that the chemical is brittle [111]. Again equation 4.17 can be used to compute Zener's anisotropy ( $A$ ) [112, 113] factor, which indicates that the compounds are

## Results and Discussion

---

**Table 4.5:** Calculated the estimated elastic constant  $C_{11}$ ,  $C_{12}$ ,  $C_{44}$ , Cauchy's pressure of  $K_2AgBiI_6$  under hydrostatic pressure.

Pressures (GPa)	$C_{11}$	$C_{12}$	$C_{44}$	$C_{12} - C_{44}$
0	39.38	8.94	5.27	3.67
5	81.99	16.15	5.13	11.02
10	116.02	20.66	5.64	15.02
20	196.64	19.17	5.83	13.34
30	244.77	23.29	6.76	16.53
40	296.79	24.30	6.70	17.59
50	344.58	27.65	7.90	19.75

**Table 4.6:** The calculated the Bulk modulus  $B$  (GPa), the Shear modulus  $G$  (GPa), Young's modulus  $Y$  (GPa), the elastic anisotropy factor ( $A$ ),  $B/G$  ratio and Poisson's ratio ( $\nu$ ) of  $K_2AgBiI_6$  under hydrostatic pressure.

Pressures (GPa)	$B$	$G$	$Y$	$A$	$B/G$	$\nu$
0	19.09	8.19	21.51	0.346	2.33	0.312
5	38.10	12.00	32.58	0.155	3.17	0.357
10	52.45	15.58	42.53	0.118	3.36	0.364
20	78.33	24.15	65.71	0.065	3.24	0.360
30	97.12	29.59	80.58	0.061	3.28	0.361
40	115.13	34.67	94.53	0.049	3.32	0.363
50	133.29	40.43	110.16	0.049	3.29	0.362

anisotropic.

$$A = \frac{2C_{44}}{C_{11} - C_{12}} \quad (4.18)$$

From Table 4.4 for the system  $K_2AgSbI_6$ , we can see that at ambient pressure, the value of  $\nu$  is 0.308 and  $B/G$  is 2.27. Under induced pressure, the values of  $\nu$  and  $B/G$  gradually increase. At 20 GPa pressure, they are 0.335 and 2.69, respectively, indicating a more ductile nature compared to ambient conditions. Similarly, from Table 4.6 for the system  $K_2AgBiI_6$ , at ambient pressure, the value of  $\nu$  is 0.312 and  $B/G$  is 2.33. Under induced pressure, the values of  $\nu$  and  $B/G$  gradually increase.

## Results and Discussion

---

At 50 GPa pressure, they are 0.362 and 3.29, respectively, indicating a more ductile nature compared to ambient conditions.

When we compare the two systems,  $\text{K}_2\text{AgSbI}_6$  and  $\text{K}_2\text{AgBiI}_6$ , we can see that  $\text{K}_2\text{AgBiI}_6$  is more ductile than  $\text{K}_2\text{AgSbI}_6$ . Therefore, we can conclude that the system  $\text{K}_2\text{AgBiI}_6$  is more suitable for mechanical device applications between the two.

# Conclusions

---

The crystal structure of the material  $K_2AgXI_6$  ( $X= Sb, Bi$ ) double perovskite has been analyzed computationally using the Full Potential Linear Augmented Plane Wave (FP-LAPW) method based on Density Functional Theory (DFT) as implemented in WIEN2k, both at ambient conditions and under different hydrostatic pressures. The Perdew-Burke-Ernzerhof and Generalized Gradient Approximation (PBE-GGA), designed for materials, was utilized to compute the structural properties, revealing an increase in the lattice parameter when substituting the Bi element for the Sb element. The lattice parameter was determined to be 12.03 Å for the  $K_2AgSbI_6$  and 12.18 Å for the  $K_2AgBiI_6$ . In this thesis, we calculated the electronic, optical, thermoelectric, and mechanical properties using the modified Becke and Johnson (mBJ) approximation for the halide double perovskites  $K_2AgXI_6$  ( $X= Sb, Bi$ ) up to 20 GPa pressure for the  $K_2AgSbI_6$  compound and up to 50 GPa pressure for the  $K_2AgBiI_6$  compound, compared to ambient pressure. We chose the mBJ potential to compensate for PBE-GGA's underestimation of the band gap. Our results suggest that the bandgap increases from 0.97 eV to 1.599 eV after replacing Sb with Bi. The electronic band structure reveals a p-type semiconducting nature, indicating indirect band gaps that decrease from 0.97 eV to 0 eV for the system  $K_2AgSbI_6$  and from 1.599 eV to 0 eV for the system  $K_2AgBiI_6$  under induced pressures. The

## Conclusions

---

optical properties were studied as a function of photon energy (eV) within an energy range of 0-10 eV under different hydrostatic pressures for both compounds. From optical properties, including dielectric functions, optical reflectivity, refraction, absorption coefficients, and optical conductivity, show improved optical characteristics in the visible and ultraviolet regions under all induced pressures compared to ambient conditions for both systems. Therefore, the studied double perovskites could be contenders for solar cell and optoelectronic device applications. Thermoelectric efficiency was assessed using the figure of merit, power factor, Seebeck coefficient, electrical and thermal conductivity, and power factor. The Boltzmann transport equation was also used to compute these transport characteristics. At ambient conditions, the studied compounds exhibit a high Seebeck coefficient ( $\geq 200\mu V/K$ ) and a figure of merit of approximately 0.78, compared to the pressurized conditions. But with increasing pressure and temperature, the electrical conductivity, thermal conductivity, and power factor also increase for both systems. The ductility and stability of the compounds under ambient and pressurized conditions are assured by the mechanical properties of the compounds. From the mechanical properties, the Pugh's and Poisson's ratios ensure the ductility and mechanical stability of the compounds under induced pressure compared to ambient pressure. By virtue of their tolerance factors of 0.99 for  $K_2AgSbI_6$  and 0.94 for  $K_2AgBiI_6$ , as well as their elastic properties, these materials are structurally, thermodynamically, and mechanically stable.

In summary,  $K_2AgXI_6$  (X= Sb, Bi) double perovskite materials demonstrate favorable electronic, mechanical, thermoelectric, and optical properties under induced hydrostatic pressure compared to ambient conditions. Thus, both materials are suitable for solar cell applications, but between the two systems,  $K_2AgBiI_6$  is more suitable than  $K_2AgSbI_6$  based on negative formation energy, minimum energy states, octahedral factors, optical properties, thermal properties, and mechanical properties. We expect that our research will contribute new knowledge and value to the exploration of cost-effective optoelectronic materials.

---

# Bibliography

---

- [1] Wan-Jian Yin, Tingting Shi, and Yanfa Yan. Unique properties of halide perovskites as possible origins of the superior solar cell performance. *Advanced Materials*, 26(27):4653–4658, 2014.
- [2] Martin A Green, Anita Ho-Baillie, and Henry J Snaith. The emergence of perovskite solar cells. *Nature Photonics*, 8(7):506–514, 2014.
- [3] Dong Shi, Valerio Adinolfi, Riccardo Comin, Mingjian Yuan, Erkki Alarousu, Andrei Buin, Yin Chen, Sjoerd Hoogland, Alexander Rothenberger, Khabiboulakh Katsiev, et al. Low trap-state density and long carrier diffusion in organolead trihalide perovskite single crystals. *Science*, 347(6221):519–522, 2015.
- [4] Hong Wang, Muhammad Asif Amjad, Noman Arshed, Abdullah Mohamed, Shamsher Ali, Muhammad Afaq Haider Jafri, and Yousaf Ali Khan. Retracted: Fossil energy demand and economic development in brics countries. *Frontiers in Energy Research*, 10:842793, 2022.
- [5] Christian Bogmans, Lama Kiyasseh, Akito Matsumoto, and Andreas Pescatori. Energy, efficiency gains and economic development: when will global energy demand saturate? 2020.
- [6] Muhammad Kamran Khan, Muhammad Imran Khan, and Muhammad Rehan. The relationship between energy consumption, economic growth and carbon dioxide emissions in pakistan. *Financial Innovation*, 6(1):1, 2020.
- [7] Loiy Al-Ghussain. Global warming: review on driving forces and mitigation. *Environmental Progress & Sustainable Energy*, 38(1):13–21, 2019.

## Bibliography

---

- [8] Phebe Asantewaa Owusu and Samuel Asumadu-Sarkodie. A review of renewable energy sources, sustainability issues and climate change mitigation. *Cogent Engineering*, 3(1):1167990, 2016.
- [9] Ehsanur Rahman and Alireza Nojeh. Semiconductor thermionics for next generation solar cells: photon enhanced or pure thermionic? *Nature Communications*, 12(1):4622, 2021.
- [10] Ching Lin. Stabilizing organic–inorganic lead halide perovskite solar cells with efficiency beyond 20%. *Frontiers in Chemistry*, 8:592, 2020.
- [11] Gwisu Kim, Hanul Min, Kyoung Su Lee, Do Yoon Lee, So Me Yoon, and Sang Il Seok. Impact of strain relaxation on performance of  $\alpha$ -formamidinium lead iodide perovskite solar cells. *Science*, 370(6512):108–112, 2020.
- [12] Xin-Feng Diao, Yan-lin Tang, Tian-yu Tang, Quan Xie, Kun Xiang, and Gao-fu Liu. Study on the stability of organic–inorganic perovskite solar cell materials based on first principle. *Molecular Physics*, 118(8):e1665200, 2020.
- [13] Yuanyuan Zhou and Yixin Zhao. Chemical stability and instability of inorganic halide perovskites. *Energy and Environmental Science*, 12(5):1495–1511, 2019.
- [14] Sergio Aina, Belén Villacampa, and María Bernechea. Earth-abundant non-toxic perovskite nanocrystals for solution processed solar cells. *Materials Advances*, 2(13):4140–4151, 2021.
- [15] Wensi Cai, Haiyun Li, Mengchao Li, Meng Wang, Huaxin Wang, Jiangzhao Chen, and Zhigang Zang. Opportunities and challenges of inorganic perovskites in high-performance photodetectors. *Journal of Physics D: Applied Physics*, 54(29):293002, 2021.
- [16] Hanan Absike, Nora Baaalla, Rachida Lamouri, Hicham Labrim, and Hamid Ez-zahraouy. Optoelectronic and photovoltaic properties of  $\text{Cs}_2\text{AgBiX}_6$  (X= Br, Cl, or I) halide double perovskite for solar cells: Insight from density functional theory. *International Journal of Energy Research*, 46(8):11053–11064, 2022.
- [17] Md Safin Alam, Md Saiduzzaman, Arpon Biswas, Tanjun Ahmed, Aldina Sultana, and Khandaker Monower Hossain. Tuning band gap and enhancing optical functions of  $\text{AGeF}_3$  (A= K, Rb) under pressure for improved optoelectronic applications. *Scientific Reports*, 12(1):8663, 2022.

## Bibliography

---

- [18] H Absike, N Baaalla, L Attou, H Labrim, B Hartiti, and H Ez-zahraouy. Theoretical investigations of structural, electronic, optical and thermoelectric properties of oxide halide perovskite  $\text{ACoO}_3$  ( $A = \text{Nd, Pr or La}$ ). *Solid State Communications*, 345:114684, 2022.
- [19] I Hamideddine, N Tahiri, O El Bounagui, and H Ez-Zahraouy. Ab initio study of structural and optical properties of the halide perovskite  $\text{KBX}_3$  compound. *Journal of the Korean Ceramic Society*, 59(3):350–358, 2022.
- [20] Xin-Gang Zhao, Ji-Hui Yang, Yuhao Fu, Dongwen Yang, Qiaoling Xu, Liping Yu, Su-Huai Wei, and Lijun Zhang. Design of lead-free inorganic halide perovskites for solar cells via cation-transmutation. *Journal of the American Chemical Society*, 139(7):2630–2638, 2017.
- [21] Ying Liu, Angshuman Nag, Liberato Manna, and Zhiguo Xia. Lead-free double perovskite  $\text{Cs}_2\text{AgInCl}_6$ . *Angewandte Chemie*, 133(21):11696–11707, 2021.
- [22] Jakob C Dahl, Wojciech T Osowiecki, Yao Cai, Joseph K Swabeck, Yehonadav Bekenstein, Mark Asta, Emory M Chan, and A Paul Alivisatos. Probing the stability and band gaps of  $\text{Cs}_2\text{AgInCl}_6$  and  $\text{Cs}_2\text{AgSbCl}_6$  lead-free double perovskite nanocrystals. *Chemistry of Materials*, 31(9):3134–3143, 2019.
- [23] Tong Cai, Wenwu Shi, Sooyeon Hwang, Kanishka Kobbekaduwa, Yasutaka Nagaoka, Hanjun Yang, Katie Hills-Kimball, Hua Zhu, Junyu Wang, Zhiguo Wang, et al. Lead-free  $\text{Cs}_4\text{CuSb}_2\text{Cl}_{12}$  layered double perovskite nanocrystals. *Journal of the American Chemical Society*, 142(27):11927–11936, 2020.
- [24] I Hamideddine, H Zitouni, N Tahiri, O El Bounagui, and H Ez-Zahraouy. A dft study of the electronic structure, optical, and thermoelectric properties of halide perovskite  $\text{KGeI}_{3-x}\text{Br}_x$  materials: photovoltaic applications. *Applied Physics A*, 127:1–7, 2021.
- [25] Hang Yin, Yeming Xian, Yongli Zhang, Weijian Chen, Xiaoming Wen, Naveed Ur Rahman, Yi Long, Baohua Jia, Jiandong Fan, and Wenzhe Li. An emerging lead-free double-perovskite  $\text{Cs}_2\text{AgFeCl}_6$ : In single crystal. *Advanced Functional Materials*, 30(43):2002225, 2020.
- [26] Aron J Huckaba, Daniel T Sun, Albertus A Sutanto, Mounir Mensi, Yi Zhang, Wendy L Queen, and Mohammad Khaja Nazeeruddin. Lead sequestration

## Bibliography

---

- from perovskite solar cells using a metal–organic framework polymer composite. *Energy Technology*, 8(7):2000239, 2020.
- [27] David P McMeekin, Golnaz Sadoughi, Waqaas Rehman, Giles E Eperon, Michael Saliba, Maximilian T Hörantner, Amir Haghghirad, Nobuya Sakai, Lars Korte, Bernd Rech, et al. A mixed-cation lead mixed-halide perovskite absorber for tandem solar cells. *Science*, 351(6269):151–155, 2016.
- [28] Qianqian Fan, Gill V Biesold-McGee, Jianzhong Ma, Qunna Xu, Shuang Pan, Juan Peng, and Zhiqun Lin. Lead-free halide perovskite nanocrystals: crystal structures, synthesis, stabilities, and optical properties. *Angewandte Chemie International Edition*, 59(3):1030–1046, 2020.
- [29] De-Yuan Hu, Xian-Hao Zhao, Tian-Yu Tang, Li-Min Lu, Li Li, Li-Ke Gao, and Yan-Lin Tang. First-principles study on the structural, elastic, electronic and optical properties of lead-free double perovskites  $\text{Cs}_2\text{CuBiX}_6$  ( $X = \text{I, Br, Cl}$ ). *Materials Today Communications*, 29:102842, 2021.
- [30] De-Yuan Hu, Xian-Hao Zhao, Tian-Yu Tang, Li-Min Lu, Li Li, Li-Ke Gao, and Yan-Lin Tang. Exploring the structural, electronic and optical properties of vacancy-ordered double perovskites  $\text{Cs}_2\text{TlAsX}_6$  ( $X = \text{I, Br, Cl}$ ) based on first-principles. *Physics Letters A*, 427:127917, 2022.
- [31] De-Yuan Hu, Xian-Hao Zhao, Tian-Yu Tang, Li-Min Lu, Li Li, Li-Ke Gao, and Yan-Lin Tang. Revealing structural, elastic, electronic and optical properties of potential perovskites  $\text{K}_2\text{CuBiX}_6$  ( $X = \text{Br, Cl}$ ) based on first-principles. *Journal of Solid State Chemistry*, 310:123046, 2022.
- [32] Muhammad Waqas Iqbal, Mumtaz Manzoor, NA Noor, Ibadur Rehman, Nohseen Mushahid, Sikandar Aftab, Yousef Muhammad Alanazi, Hamid Ullah, and Amir Muhammad Afzal. Tuning of the electronic bandgap of lead-free double perovskites  $\text{K}_2\text{AgBiX}_6$  ( $X = \text{Cl, Br}$ ) for solar cells applications and their thermoelectric characteristics. *Solar Energy*, 239:234–241, 2022.
- [33] Fatima Aslam, B Sabir, and M Hassan. Structural, electronic, optical, thermoelectric, and transport properties of indium-based double perovskite halides  $\text{Cs}_2\text{InAgX}_6$  ( $X = \text{Cl, Br, I}$ ) for energy applications. *Applied Physics A*, 127:1–12, 2021.

## Bibliography

---

- [34] Fatima Aslam, Hamid Ullah, and M Hassan. Theoretical investigation of  $\text{Cs}_2\text{InBiX}_6$  ( $X = \text{Cl, Br, I}$ ) double perovskite halides using first-principle calculations. *Materials Science and Engineering: B*, 274:115456, 2021.
- [35] Fatima Aslam, Hamid Ullah, and M Hassan. First principle study of band gap tuning in  $\text{Cs}_2\text{InSbX}_6$  ( $X = \text{Cl, Br, I}$ ) for optoelectronic and thermoelectric applications. *Physica Scripta*, 97(4):045801, 2022.
- [36] Junaid Munir, Inamul Mursaleen, Hamid M Ghaithan, Qurat ul Ain, Abdullah Ahmed Ali Ahmed, and Saif MH Qaid. First-principles investigations of the mechanically and thermodynamically stable potassium-based double perovskites  $\text{K}_2\text{TlAsX}_6$  ( $X = \text{Cl, Br}$ ) for optoelectronic and renewable applications. *Materials Science and Engineering: B*, 298:116830, 2023.
- [37] Ghulam M Mustafa, Abdul Slam, Sadaf Saba, NA Noor, M Waqas Iqbal, and A Dahshan. Optoelectronic and thermoelectric characteristics of halide based double perovskites  $\text{K}_2\text{YAgX}_6$  ( $X = \text{Br, I}$ ) for energy storage applications. *Polyhedron*, 229:116184, 2023.
- [38] Fuxiang Ji, Johan Klarbring, Feng Wang, Weihua Ning, Linqin Wang, Chunyang Yin, José Silvestre Mendoza Figueroa, Christian Kolle Christensen, Martin Etter, Thomas Ederth, et al. Lead-free halide double perovskite  $\text{Cs}_2\text{AgBiBr}_6$  with decreased band gap. *Angewandte Chemie*, 132(35):15303–15306, 2020.
- [39] Md Roknuzzaman, Chunmei Zhang, Kostya Ostrikov, Aijun Du, Hongxia Wang, Lianzhou Wang, and Tuquabo Tesfamichael. Electronic and optical properties of lead-free hybrid double perovskites for photovoltaic and optoelectronic applications. *Scientific Reports*, 9(1):718, 2019.
- [40] N Rajeev Kumar and R Radhakrishnan. Electronic, optical and mechanical properties of lead-free halide double perovskites using first-principles density functional theory. *Materials Letters*, 227:289–291, 2018.
- [41] Xin-Gang Zhao, Dongwen Yang, Ji-Chang Ren, Yuanhui Sun, Zewen Xiao, and Lijun Zhang. Rational design of halide double perovskites for optoelectronic applications. *Joule*, 2(9):1662–1673, 2018.
- [42] H Rached, S Bendaoudia, and D Rached. Investigation of iron-based double perovskite oxides on the magnetic phase stability, mechanical, electronic and

## Bibliography

---

- optical properties via first-principles calculation. *Materials Chemistry and Physics*, 193:453–469, 2017.
- [43] Sanjeev Kumar, Gianluca Giovannetti, Jeroen van den Brink, and Silvia Picozzi. Theoretical prediction of multiferroicity in double perovskite  $\text{Y}_2\text{NiMnO}_6$ . *Physical Review B*, 82(13):134429, 2010.
- [44] Q Mahmood, Taher Ghrib, Amani Rached, A Laref, and MA Kamran. Probing of mechanical, optical and thermoelectric characteristics of double perovskites  $\text{Cs}_2\text{GeCl/Br}_6$  by dft method. *Materials Science in Semiconductor Processing*, 112:105009, 2020.
- [45] NA Noor, M Waqas Iqbal, Taharh Zelai, Asif Mahmood, HM Shaikh, Shahid M Ramay, and Waheed Al-Masry. Analysis of direct band gap  $\text{A}_2\text{ScInI}_6$  (A= Rb, Cs) double perovskite halides using dft approach for renewable energy devices. *Journal of Materials Research and Technology*, 13:2491–2500, 2021.
- [46] Muhammad Saeed, Izaz Ul Haq, Awais Siddique Saleemi, Shafiq Ur Rehman, Bakhtiar Ul Haq, Aijaz Rasool Chaudhry, and Imad Khan. First-principles prediction of the ground-state crystal structure of double-perovskite halides  $\text{Cs}_2\text{AgCrX}_6$  (X= Cl, Br, and I). *Journal of Physics and Chemistry of Solids*, 160:110302, 2022.
- [47] MA Ghebouli, T Chihi, B Ghebouli, and M Fatmi. Study of the structural, elastic, electronic and optical properties of lead free halide double perovskites  $\text{Cs}_2\text{AgBiX}_6$  (X= Br, Cl). *Chinese Journal of Physics*, 56(1):323–330, 2018.
- [48] Eric Yang and Xuan Luo. Theoretical pressure-tuning bandgaps of double perovskites  $\text{A}_2(\text{BB}')\text{X}_6$  for photo-voltaics. *Solar Energy*, 207:165–172, 2020.
- [49] Yongfu Liang, Xiaoli Huang, Yanping Huang, Xin Wang, Fangfei Li, Youchun Wang, Fubo Tian, Bingbing Liu, Ze Xiang Shen, and Tian Cui. New metallic ordered phase of perovskite  $\text{CsPbI}_3$  under pressure. *Advanced Science*, 6(14):1900399, 2019.
- [50] Tingting Yin, Bo Liu, Jiayu Yan, Yanan Fang, Minghua Chen, Wee Kiang Chong, Shaojie Jiang, Jer-Lai Kuo, Jiye Fang, Pei Liang, et al. Pressure-engineered structural and optical properties of two-dimensional

## Bibliography

---

- (C<sub>4</sub>H<sub>9</sub>NH<sub>3</sub>)<sub>2</sub>PbI<sub>4</sub> perovskite exfoliated nm-thin flakes. *Journal of the American Chemical Society*, 141(3):1235–1241, 2018.
- [51] Zhiwei Ma, Zhun Liu, Siyu Lu, Lingrui Wang, Xiaolei Feng, Dongwen Yang, Kai Wang, Guanjun Xiao, Lijun Zhang, Simon AT Redfern, et al. Pressure-induced emission of cesium lead halide perovskite nanocrystals. *Nature Communications*, 9(1):4506, 2018.
- [52] Francisco Javier Manjón and Daniel Errandonea. Pressure-induced structural phase transitions in materials and earth sciences. *Physica Status Solidi (b)*, 246(1):9–31, 2009.
- [53] John S Tse. A chemical perspective on high pressure crystal structures and properties. *National Science Review*, 7(1):149–169, 2020.
- [54] Mohammed Miri, Younes Ziat, Hamza Belkhanchi, Zakaryaa Zarhri, and Youssef Ait El Kadi. Structural and optoelectronic properties of LiYP (Y= Ca, Mg, and Zn) half-heusler alloy under pressure: A dft study. *Physica B: Condensed Matter*, 667:415216, 2023.
- [55] Enlai Dong, Bo Liu, Qing Dong, Xuhan Shi, Xin Ma, Ran Liu, Xuebin Zhu, Xuan Luo, Xiaodong Li, Yanchun Li, et al. Effects of pressure on the structure and properties of layered ferromagnetic Cr<sub>2</sub>Ge<sub>2</sub>Te<sub>6</sub>. *Physica B: Condensed Matter*, 595:412344, 2020.
- [56] Nazila Zarabinia and Reza Rasuli. Electronic and optical properties of halide double-perovskites under strain: A density functional study. *Energy Sources, Part A: Recovery, Utilization, and Environmental Effects*, 43(20):2443–2455, 2021.
- [57] Peter Blaha, Karlheinz Schwarz, Fabien Tran, Robert Laskowski, Georg KH Madsen, and Laurence D Marks. Wien2k: An apw+ lo program for calculating the properties of solids. *The Journal of Chemical Physics*, 152(7), 2020.
- [58] Erwin Schrödinger. An undulatory theory of the mechanics of atoms and molecules. *Physical Review*, 28(6):1049, 1926.
- [59] DJ Griffiths. Introduction to quantum mechanics 2nd ed.-solutions. 2005.
- [60] Max Born. Quantenmechanik der stoßvorgänge. *Zeitschrift Physik*, 38(11):803–827, 1926.

## Bibliography

---

- [61] David C Young. Density functional theory. *Computational Chemistry*, pages 42–48, 2001.
- [62] Wolfgang Pauli. The connection between spin and statistics. *Physical Review*, 58(8):716, 1940.
- [63] Arthur Jabs. Connecting spin and statistics in quantum mechanics. *Foundations of Physics*, 40(7):776–792, 2010.
- [64] Jean-Michel Combes, Pierre Duclos, and Ruedi Seiler. The born-oppenheimer approximation. In *Rigorous Atomic and Molecular Physics*, pages 185–213. Springer, 1981.
- [65] Michael P Marder. *Condensed matter physics*. John Wiley & Sons, 2010.
- [66] David J Griffiths and Darrell F Schroeter. *Introduction to quantum mechanics*. Cambridge university press, 2018.
- [67] Max Born. *Physik im Wandel meiner Zeit*. Springer-Verlag, 2013.
- [68] Hubert Klar. The born-oppenheimer approximation revisited. *Journal of Applied Mathematics and Physics*, 8(8):1507–1514, 2020.
- [69] Hanno Essén. The physics of the born–oppenheimer approximation. *International Journal of Quantum Chemistry*, 12(4):721–735, 1977.
- [70] F Schwabl. Quantum mechanics (QM I). ; Quantenmechanik (QM I). Eine Einfuehrung. 2007.
- [71] DJ Griffiths. Introduction to quantum mechanics 2nd ed.-solutions. 2005.
- [72] Paul Adrien Maurice Dirac. A new notation for quantum mechanics. In *Mathematical Proceedings of the Cambridge Philosophical Society*, volume 35, pages 416–418. Cambridge University Press, 1939.
- [73] Wolfgang Pauli. The connection between spin and statistics. *Physical Review*, 58(8):716, 1940.
- [74] Attila Szabo and Neil S Ostlund. *Modern quantum chemistry: introduction to advanced electronic structure theory*. Courier Corporation, 1996.
- [75] Walter Kohn. Nobel lecture: Electronic structure of matter—wave functions and density functionals. *Reviews of Modern Physics*, 71(5):1253, 1999.

## Bibliography

---

- [76] Wolfram Koch and Max C Holthausen. *A chemist's guide to density functional theory*. John Wiley & Sons, 2015.
- [77] Philippe C Hiberty, Stephane Humbel, David Danovich, and Sason Shaik. What is physically wrong with the description of odd-electron bonding by hartree-fock theory? a simple nonempirical remedy. *Journal of the American Chemical Society*, 117(35):9003–9011, 1995.
- [78] Ida Josefsson, Kristjan Kunnus, Simon Schreck, Alexander Fohllisch, Frank de Groot, Philippe Wernet, and Michael Odelius. Ab initio calculations of x-ray spectra: Atomic multiplet and molecular orbital effects in a multiconfigurational scf approach to the l-edge spectra of transition metal complexes. *The journal of Physical Chemistry Letters*, 3(23):3565–3570, 2012.
- [79] Pierre Hohenberg and Walter Kohn. Inhomogeneous electron gas. *Physical Review*, 136(3B):B864, 1964.
- [80] Robert G Parr. Weitao yang. density-functional theory of atoms and molecules, 1989.
- [81] JA Camargo-Martínez and R Baquero. Performance of the modified becke-johnson potential for semiconductors. *Physical Review B*, 86(19):195106, 2012.
- [82] Diola Bagayoko, Yacouba Issa Diakit , and Lashounda Franklin. Comments on all-electron self-consistent gw in the matsubara-time domain: Implementation and benchmarks of semiconductors and insulators. *Physical Review B*, 93:125210, 2016.
- [83] Walter Kohn and Lu Jeu Sham. Self-consistent equations including exchange and correlation effects. *Physical Review*, 140(4A):A1133, 1965.
- [84] Xiaofei Shao, Peitao Liu, Cesare Franchini, Yi Xia, and Jiangang He. Assessing the performance of exchange-correlation functionals on lattice constants of binary solids at room temperature within the quasiharmonic approximation. *Physical Review B*, 108(2):024306, 2023.
- [85] Axel D Becke. Density-functional exchange-energy approximation with correct asymptotic behavior. *Physical Review A*, 38(6):3098, 1988.
- [86] John P Perdew, John A Chevary, Sy H Vosko, Koblar A Jackson, Mark R Pederson, Dig J Singh, and Carlos Fiolhais. Atoms, molecules, solids, and

## Bibliography

---

- surfaces: Applications of the generalized gradient approximation for exchange and correlation. *Physical Review B*, 46(11):6671, 1992.
- [87] John P Perdew, Kieron Burke, and Matthias Ernzerhof. Generalized gradient approximation made simple. *Physical Review Letters*, 77(18):3865, 1996.
- [88] Vladimir I Anisimov, Ferdi Aryasetiawan, and AI Lichtenstein. First-principles calculations of the electronic structure and spectra of strongly correlated systems: the lda+ u method. *Journal of Physics: Condensed Matter*, 9(4):767, 1997.
- [89] MT Czyżyk and GA Sawatzky. Local-density functional and on-site correlations: The electronic structure of  $\text{La}_2\text{CuO}_4$  and  $\text{LaCuO}_3$ . *Physical Review B*, 49(20):14211, 1994.
- [90] Vlasdimir I Anisimov, IV Solovyev, MA Korotin, MT Czyżyk, and GA Sawatzky. Density-functional theory and nio photoemission spectra. *Physical Review B*, 48(23):16929, 1993.
- [91] Erik R Ylvisaker, Warren E Pickett, and Klaus Koepernik. Anisotropy and magnetism in the lsd+ u method. *Physical Review B*, 79(3):035103, 2009.
- [92] Peter Blaha, Karlheinz Schwarz, P Sorantin, and SB Trickey. Full-potential, linearized augmented plane wave programs for crystalline systems. *Computer Physics Communications*, 59(2):399–415, 1990.
- [93] David Koller, Fabien Tran, and Peter Blaha. Improving the modified becke-johnson exchange potential. *Physical Review B*, 85(15):155109, 2012.
- [94] David Koller, Fabien Tran, and Peter Blaha. Merits and limits of the modified becke-johnson exchange potential. *Physical Review B*, 83(19):195134, 2011.
- [95] Nirpendra Singh, Dalaver Anjum, Gobind Das, Issam Qattan, Shashikant Patole, and Muhammad Sajjad. Phonon dynamics and transport properties of copper thiocyanate and copper selenocyanate pseudohalides. *ACS Omega*, 5(44):28637–28642, 2020.
- [96] Victor Moritz Goldschmidt. Die gesetze der krystallochemie. *Naturwissenschaften*, 14(21):477–485, 1926.
- [97] Chonghe Li, Kitty Chi Kwan Soh, and Ping Wu. Formability of  $\text{ABO}_3$  perovskites. *Journal of Alloys and Compounds*, 372(1-2):40–48, 2004.

## Bibliography

---

- [98] Chonghea Li, Xionggang Lu, Weizhong Ding, Liming Feng, Yonghui Gao, and Ziming Guo. Formability of  $ABX_3$  ( $X = F, Cl, Br, I$ ) halide perovskites. *Acta Crystallographica Section B: Structural Science*, 64(6):702–707, 2008.
- [99] Mosayeb Naseri, Dennis R Salahub, Shirin Amirian, Hatf Shahmohamadi, Mohammad Abdur Rashid, Mehrdad Faraji, and Negin Fatahi. Multi-functional lead-free  $Ba_2XSbO_6$  ( $X = Al, Ga$ ) double perovskites with direct bandgaps for photocatalytic and thermoelectric applications: A first principles study. *Materials Today Communications*, 35:105617, 2023.
- [100] Lalhriatpuia Hnamte, Sandeep Sandeep, Himanshu Joshi, and RK Thapa. Electronic and optical properties of double perovskite  $Ba_2VMoO_6$ : Fp-lapw study. In *AIP Conference Proceedings*, volume 1953. AIP Publishing, 2018.
- [101] OA Lozhkina, AA Murashkina, MS Elizarov, VV Shilovskikh, AA Zolotarev, Yu V Kapitonov, R Kevorkyants, AV Emeline, and T Miyasaka. Microstructural analysis and optical properties of the halide double perovskite  $Cs_2BiAgBr_6$  single crystals. *Chemical Physics Letters*, 694:18–22, 2018.
- [102] B Amin, Iftikhar Ahmad, M Maqbool, Souraya Goumri-Said, and R Ahmad. Ab initio study of the bandgap engineering of  $Al_{1-x}Ga_xN$  for optoelectronic applications. *Journal of Applied Physics*, 109(2), 2011.
- [103] F Wooten. Optical properties of solids academic press: New york. *NY, USA, London, UK*, 1972.
- [104] Luyan Li, Weihua Wang, Hui Liu, Xindian Liu, Qinggong Song, and Shiwei Ren. First principles calculations of electronic band structure and optical properties of Cr-doped ZnO. *The Journal of Physical Chemistry C*, 113(19):8460–8464, 2009.
- [105] Diwen Liu, Wenying Zha, Rusheng Yuan, Benyong Lou, and Rongjian Sa. Indirect-to-direct band gap transition and optical properties of metal alloys of  $Cs_2Te_{1-x}Ti_xI_6$ : a theoretical study. *RSC Advances*, 10(60):36734–36740, 2020.
- [106] Thi Kim Phuong Luong, Vinh Le Thanh, Abdelhamid Ghrib, Moustafa El Kurdi, and Philippe Boucaud. Making germanium, an indirect band gap semiconductor, suitable for light-emitting devices. *Advances in Natural Sciences: Nanoscience and Nanotechnology*, 6(1):015013, 2015.

## Bibliography

---

- [107] Sukriti Ghosh and Dinesh C Gupta. Electronic, magnetic, elastic and thermodynamic properties of  $\text{Cu}_2\text{MnGa}$ . *Journal of Magnetism and Magnetic Materials*, 411:120–127, 2016.
- [108] Hillard Bell Huntington. The elastic constants of crystals. In *Solid State Physics*, volume 7, pages 213–351. Elsevier, 1958.
- [109] DG Pettifor. Theoretical predictions of structure and related properties of intermetallics. *Materials Science and Technology*, 8(4):345–349, 1992.
- [110] SF Pugh. Xcii. relations between the elastic moduli and the plastic properties of polycrystalline pure metals. *The London, Edinburgh, and Dublin Philosophical Magazine and Journal of Science*, 45(367):823–843, 1954.
- [111] K Haddadi, A Bouhemadou, L Louail, and Y Medkour. Structural, elastic and electronic properties of  $\text{XNCa}_3$  (X= Ge, Sn and Pb) compounds. *Solid State Communications*, 149(15-16):619–624, 2009.
- [112] Christopher M Kube. Elastic anisotropy of crystals. *AIP Advances*, 6(9), 2016.
- [113] Clarence M Zener and Sidney Siegel. Elasticity and anelasticity of metals. *The Journal of Physical Chemistry*, 53(9):1468–1468, 1949.